Fermilab

FERMILAB-THESIS-2003-13

Search for W Boson Pair Production in the Lepton + Jet Channel in 1.8-TeV Proton-Antiproton Collisions

Hideaki TAKANO

A dissertation submitted to the Doctoral Program
in Physics, the University of Tsukuba
in partial fulfillment of the requirements
for the degree of Doctor of Philosophy (Science)

April 2003

Abstract

CDF collaboration searched for W pair production in the dilepton channel, $W^+W^- \rightarrow \ell\nu\ell\nu$, and reported an evidence in 1996. CDF found five signal candidate events while the expected number of background events is 1.2 ± 0.3, and extracted the cross section $\sigma(p\bar{p} \rightarrow W^+W^-) = 10.2^{+6.3}_{-5.1}(\mathrm{stat}) \pm 1.6(\mathrm{syst})$ pb.

In the present study, we search for W^+W^- production in the lepton plus dijet channel, $W^+W^- \rightarrow \ell\nu jj$, using 106 pb^{-1} data sample. To separate signals from backgrounds we use conventional variables that discriminate between quark and gluon jets, such as jet charge, track multiplicity, and charm-jet tagging. In addition, we study variables taking advantage of event characteristics that are specific to the W^+W^- final state, such as pseudo-rapidity asymmetry, azimuthal correlations, and dijet mass. We set a 95% C.L. upper limit of 61 pb on the W^+W^- production cross-section.

Acknowledgments

I would like to thank my thesis adviser Professor Shinhong Kim for his guidance through my graduate years. I would like to thank Professor Luc DeMotier for his help through my research at Fermilab. Many crucial progresses on this study were obtained from their suggestions. I would like to thank members of the top/electroweak physics group at CDF.

My deep appreciation is due to Dr. Ashutosh Kotwal, Dr. Pasha Murat, Dr. Pierre Savard, Dr. Willis Sakumoto, Prof. Melissa Franklin and Ms. Robyn Madrak, who gave me many valuable advice and suggestions.

I would like to thank staff members of the CDF Japan group, Prof. Kunitaka Kondo, Prof. Koji Takikawa, Prof. Fumihiko Ukegawa, Prof. Kazuhiko Hara, Prof. Makoto Shimojima, Dr. Hiroyuki Matsunaga and Dr. Yuji Takeuchi. They provided me with advices and encouragement at the CDF experiments.

I would like to thank CDF students and staffs which include Dr. Masashi Tanaka, Mr. Takashi Suzuki, Mr. Yoshiyuki Miyazaki, and Mr. Koji Sato. My life in Chicago was supported by their friendship. I would like to thank Ms. Carol Picciolo, Ms. Kyoko Kunori, and Ms. Kazuko Kumashiro for their help through their secretary works.

Finally I would like to thank my family for their support.

This work was supported by the U.S. Department of Energy and National Science Foundation; the Italian Istituto Nazionale di Fisica Nucleare; the Ministry of Education, Culture, Sports, Science, and Technology of Japan; the Natural Sciences and Engineering Research Council of Canada; the National Science Council of the Republic of China; the Swiss National Science Foundation; the A.P. Sloan Foundation; the Bundesministerium fuer Bildung und Forschung, Germany; and the Korea Science and Engineering Foundation (KoSEF); the Korea Research Foundation; and the Comision Interministerial de Ciencia y Tecnologia, Spain.

Contents

List of Figures

List of Tables

Chapter 1

Introduction

The standard model has been successfully adopted to explain and predict the experimental results in high energy physics. In the framework of the standard model, there are two types of elementary particles, fermion and boson. The fermion constitutes a substance which consists of leptons and quarks of six types with three generations as shown in Table 1.1. The boson consists of gluon, photon, $W^{\pm}$ and Z^0 bosons and mediates three types of interaction between fermions: gluons for strong interaction, photons for electromagnetic interaction and $W^{\pm}$ and Z^0 bosons for weak interaction. The standard model also predicted the existence of Higgs particle which provides a mass to fermions and bosons. $W^{\pm}$ boson has an electric charge ± 1 and the mass is about 80 GeV/c^2.

Table 1.1: Three generation of quarks and leptons.

$$\begin{pmatrix} u \\ d \end{pmatrix} \begin{pmatrix} c \\ s \end{pmatrix} \begin{pmatrix} t \\ b \end{pmatrix}$$

$$\begin{pmatrix} \nu_e \\ e^- \end{pmatrix} \begin{pmatrix} \nu_\mu \\ \mu^- \end{pmatrix} \begin{pmatrix} \nu_\tau \\ \tau^- \end{pmatrix}$$

1.1 $W^{\pm}$ pair production search

In the standard model, the dominant contribution to diboson production in $p\bar{p}$ collisions at $\sqrt{s} = 1.8$ TeV comes from two types of Feynman diagrams as shown in Fig. 1.1. There are substantial cancellations between the $t-$ or $u-$channel diagrams, which involve only the couplings of the bosons to fermions, and the $s-$channel diagrams which contain the tri-gauge boson coupling [1]. These cancellations result in standard model cross-sections of 9.6 pb for W boson pair production.

CDF has searched for W pair production in the dilepton channel $W^+W^- \to \ell\nu\ell\nu$ and reported the evidence for it in 1996 [2]. CDF found five signal candidate events while the expected number of background events is 1.2± 0.3, and extracted the cross section $\sigma(p\bar{p} \to W^+W^-) = 10.2^{+6.3}_{-5.1}(stat) \pm 1.6(syst)$ pb.

We search for W pair production in the lepton plus dijet channel $W^+W^- \to \ell\nu jj$. Our purpose is to establish the method for detecting W pair production in the lepton plus dijet channel and to search for W pair production in this channel. Using Monte Carlo event samples we optimize the event selection criteria. We generated W^+W^- signal events and QCD W+jet background events with PYTHIA and VECBOS event generator, respectively, and then simulated through the CDF standard detector simulation program QFL. For W^+W^- signal events we forced one W ± boson to decay into a lepton pair and another to decay into a quark pair. For QCD W+jet background events we forced a $W^\pm$ boson to decay into a lepton pair.

All jets in the signal events originate from quarks while most jets in the background events originate from gluons. The charged track multiplicity in a gluon jet is higher than that in a quark jet.

The sum of two quark charges from $W^\pm$ decay is one or minus one while a gluon jet charge is zero. To utilize this for a signal-to-background ratio improvement, we use a total electric charge Q_{tot} defined as a sum of two jet charges times a lepton charge. Jet charge is introduced by R.D.Field and R.P.Feynman [3] and has been utilized by CDF [4] and LEP experiments.

We combined all kinematic cuts into one global likelihood and optimize this global likelihood cut.

1.2 Motivation of W pair production search

1.2.1 Theoretical motivation

Tri-gauge boson coupling is a good probe for new physics beyond the Standard Model at CDF. If we introduce nonstandard couplings which are invariant under the $SU(2)_L \times U(1)_Y$ gauge group into three-boson couplings, these nonstandard couplings can spoil the substantial cancellations and cause a dramatic increase of the cross section for W pair production, especially at large values of $\sqrt{s}$. ! ! First tri-gauge boson coupling studies were made by CDF and D0. D0 set the limit on WWZ and $WW\gamma$ tri-gauge boson couplings using $WW \to \ell\nu\ell\nu$ [5] and $WW \to \ell\nu jj$ [6, 7] modes. CDF set the limit using $WW \to \ell\nu\ell\nu$ mode [1]. LEP also set the limit using $WW \to \ell\nu\ell\nu$, $WW \to \ell\nu jj$ and $WW \to \ell\nu jj$ modes [8]. Figure 1.2 shows the tri-gauge boson coupling effects on W pair production for e^+e^- collisions. The

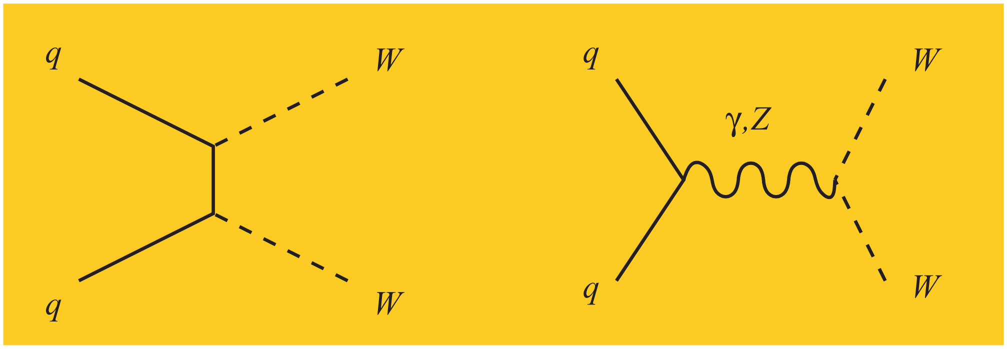

Figure 1.1: Feynman diagrams of W pair production.

$WW\gamma$ and WWZ couplings strongly suppress the W pair production. CDF can study the tri-gauge boson coupling effect at a higher energy region than they can reach in LEP experiment.

For Higgs particles with a mass above 150 GeV/c^2, the decay mode of $H \to W^+W^-$ is dominant(Fig. 1.3). LEP set an lower limit on the Higgs mass [9]. They lead to the conclusion that the Standard-Model Higgs boson must be heavier than 114.4 GeV (95 percent confidence level limit), as indicated by the excluded area drawn in yellow in the figure 1.4. The search capability for such Higgs particles at CDF has been studied [10], and CDF was found to be able to discover such Higgs with a mass below 180 GeV/c^2, where $H \to W^+W^- \to \ell\nu jj$ mode was not taken into account because the QCD W+jet background is too large. If we can reduce this QCD W+jet background in W pair search, we can make the Higgs decay mode of $H \to W^+W^- \to \ell\nu jj$ effective in the Higgs search.

1.2.2 Experimental motivation

We search for W boson pair production in the $WW \to l\nu qq$ decay mode. This decay mode has a six times larger branching ratio than $WW \to l\nu l\nu$ decay mode and we can expect about 1000 events of W pair production at first stage of our analysis.

We apply new analysis techniques to identify jets from $W \to qq$ against gluon jets at CDF. They are charged track multiplicity, jet charge and heavy flavor tag. We explain the detail of these techniques in the following sections.

The primary goal is to develop a technique to identify W pair final states where one W decays hadronically using above new analysis techniques and WW kinematical cuts. Then we test this technique on a measurement of the W^+W^- cross section using full Run I data.

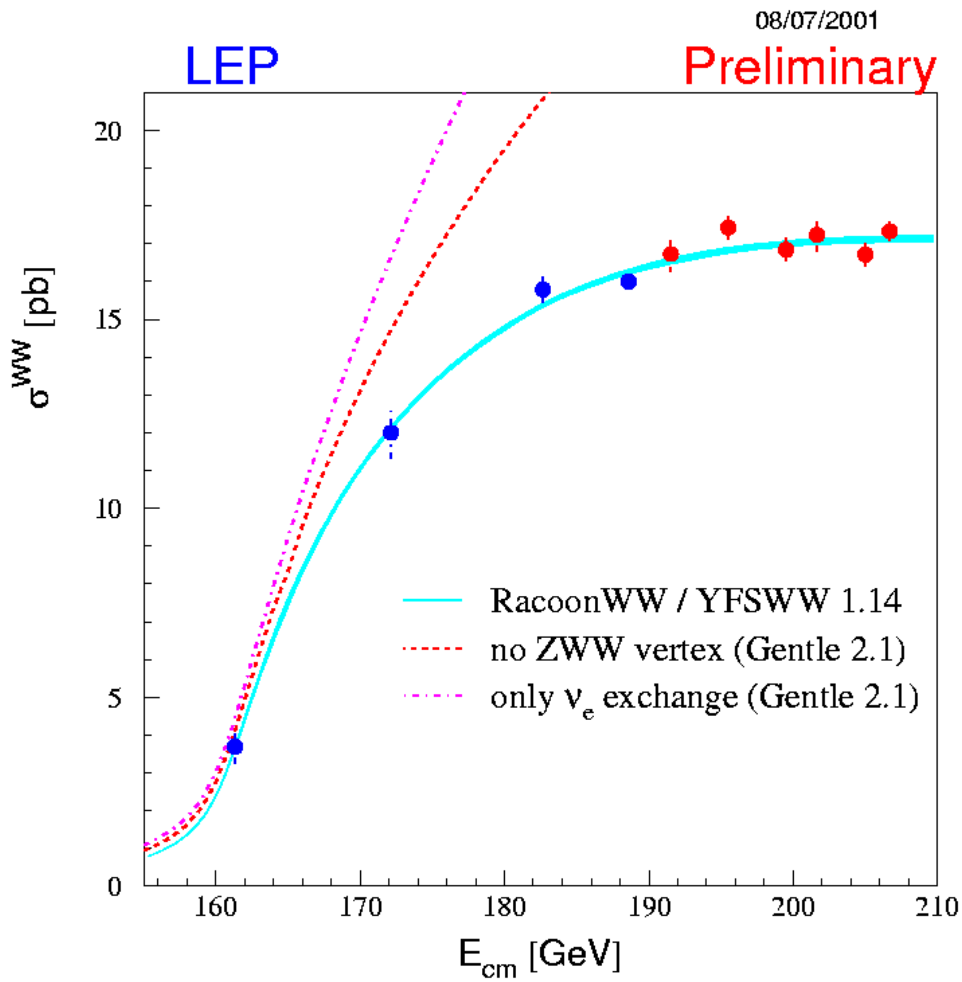

Figure 1.2: W pair production cross-section for e^+e^- collisions.

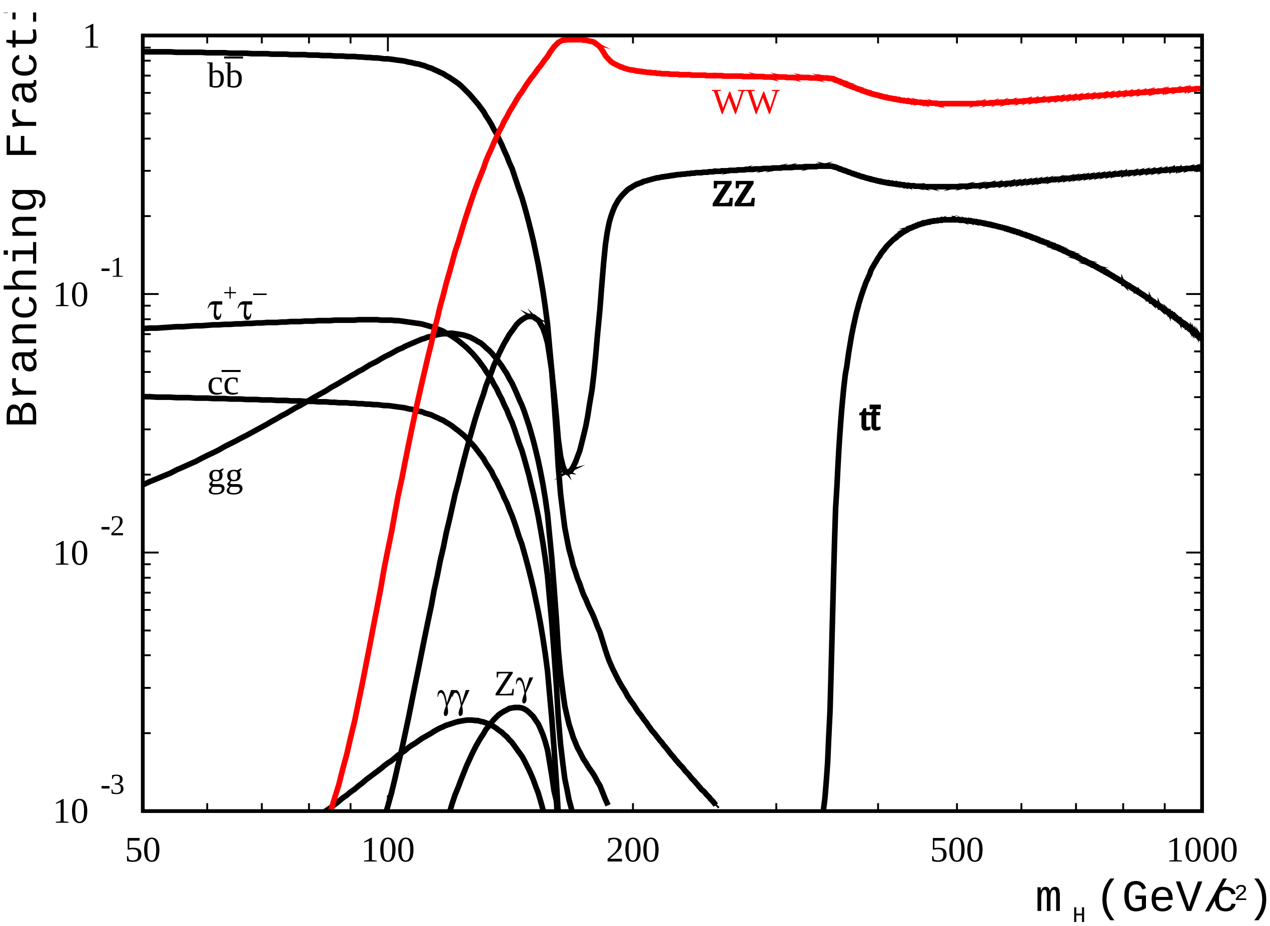

Figure 1.3: Branching fraction of Standard Model Higgs.

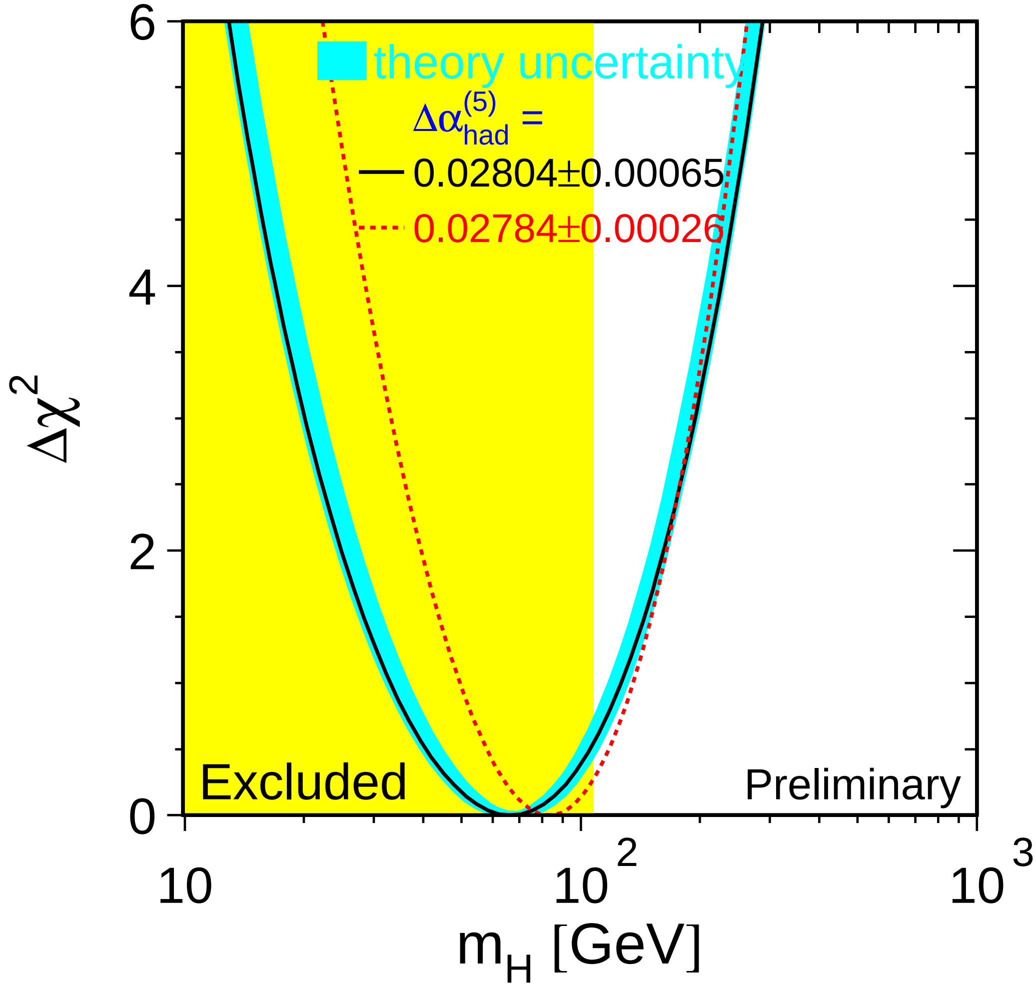

Figure 1.4: The direct searches for the Higgs boson at LEP.

Chapter 2

Experimental apparatus

2.1 The Accelerator

The Fermilab accelerator complex is shown schematically in Figure 2.1.

The Pre-accelerator, or 'Preacc' is the first of the accelerators. It is the source of the negatively-charged hydrogen ions accelerated by the linear accelerator. The Preacc consists of the source housed in an electrically-charged dome. The source converts hydrogen gas to ionized hydrogen gas (H^-). The dome is charged to a potential of -750 kV. The ionized gas is allowed to accelerate through a column from the charged dome to the grounded wall, and the H^- is accelerated to an energy of 750 keV.

The Linear Accelerator or 'Linac' is the next level of acceleration for the negatively-charged hydrogen ions. It takes the ions with an energy of 750 keV and accelerates them to an energy of 400 MeV. The linac consists of 14 cylindrical accelerating cavities arranged colinearly. The first five tanks are fed by amplifying systems using large power amplifiers (PAs). These amplify an RF frequency of 201 MHz which is then fed into each of the tanks. The last 9 RF cavities are fed by amplifying systems using klystrons. These amplify an RF frequency of 805 MHz which is then fed into each of the tanks.

The Booster is the next level of acceleration, taking the 400 MeV negative hydrogen ions, stripping the electrons off leaving only the proton core, and accelerating the protons to 8 GeV. The Booster is the first synchrotron in the acceleration chain. It consists of a series of magnets arranged around a 75 meter radius circle, with 17 RF cavities interspersed.

The Main Ring is a circular synchrotron of radius 1 km. The ring is divided up into 6 sections, labeled A through F. Main ring has 18 accelerating cavities located at the beginning of the sixth sector (F sector). It can accelerate protons from the Booster from 8 GeV to either 120 GeV or 150 GeV, depending on their destination.

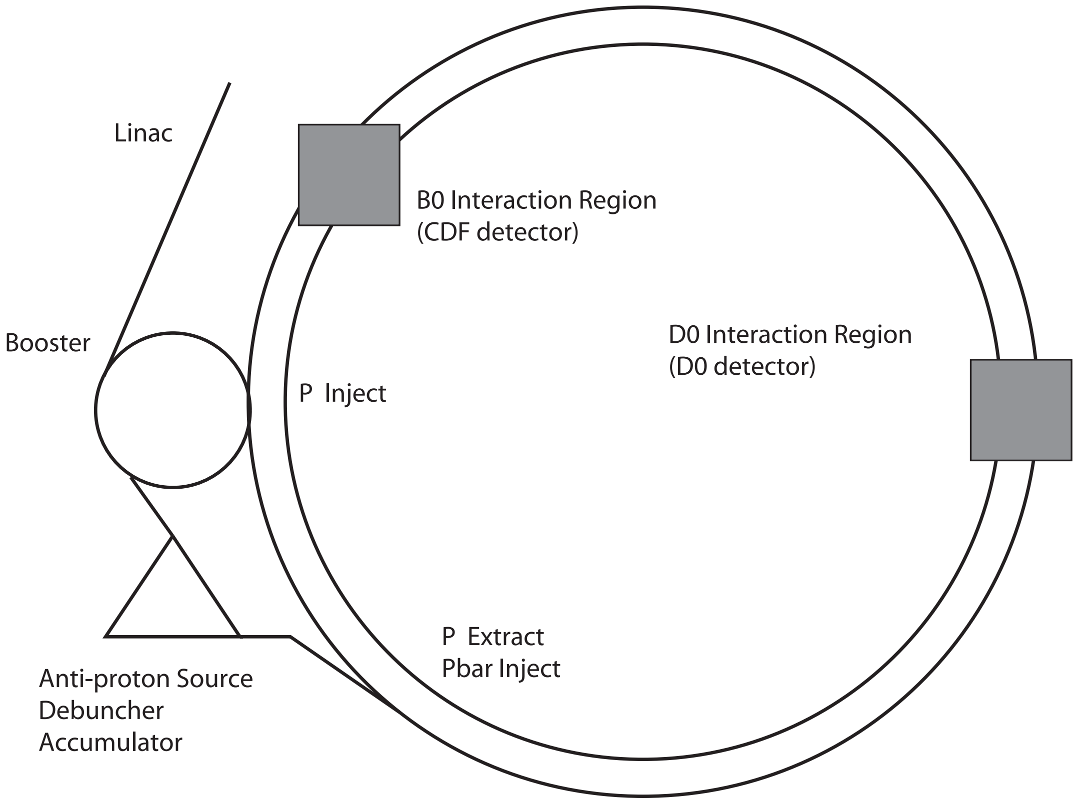

Figure 2.1: A schematic view of Fermilab accelerator complex.

As well as accepting protons from Booster, the Main Ring can accept antiprotons from the antiproton source at 8 GeV and accelerate them to 150 GeV. Once the proton or pbar beam in Main Ring is accelerated to 150 GeV, it can be sent to the Tevatron. The proton beam that is accelerated to 120 GeV can be sent to the Antiproton source.

120 GeV protons coming from Main Ring hit a tungsten target and produce antiprotons. These antiprotons are directed to the Debuncher.

The Debuncher is one of the two synchrotrons that makes up the antiproton source. The Debuncher is a rounded triangular-shaped synchrotron with a mean radius of 90 meters. Its primary purpose is to reduce the momentum spread of the antiprotons by rotating the bunches. There are also beam cooling systems that act to reduce the oscillations in the plane perpendicular to the orbit (transverse plane) as well as reducing the momentum spread of the antiprotons. The Debuncher does not 'accelerate' beam in the same sense as the other accelerators, but maintains the beam at a constant energy of 8 GeV. There are three RF systems used in the Debuncher. The antiproton beam can be transferred to the Accumulator.

The Accumulator is the second synchrotron of the antiproton source. It too is a triangular-shaped synchrotron of radius 75 meters, and is housed in the same radiation enclosure as the Debuncher. It is the storage ring for the antiprotons: all of the antiprotons made are stored here at 8 GeV and cooled until needed. Under typical condition the stack of antiprotons can be built at a rate of $\sim 4 \times 10^{10}$ antiprotons per hour.

The Tevatron is the only cryogenically cooled accelerator at Fermilab. It is a circular synchrotron of radius 1 km that has the same basic layout and shares the same radiation enclosure as Main ring. The RF section of the accelerator consists of 8 accelerating cavities. The Tevatron can accept both protons and antiprotons from Main Ring and accelerate them from 150 GeV to 900 GeV.

Six bunches of the protons and antiprotons are transferred into the Tevatron ring and the collisions occur every 3.5 μs. There are two instrumented collision points along the ring. These are labeled B0 and D0, respectively. The CDF detector is located at B0. Typical numbers of the protons and antiprotons are 2.0×10^{11} and 5.5×10^{10} per bunch, respectively. Low-β quadrupole magnets which are located immediately upstream of the CDF detector reduce the beam size the, and the dimensions of each bunch are, 30 cm along the beamline and, 30 μm in the transverse directions at the nominal interaction point. Typical instantaneous luminosity is 1.6×10^{31} cm^{-2} s^{-1}, and its lifetime is, $\sim$ 10 hours.

Figure 2.2 shows the integrated luminosity delivered to and accumulated by the CDF detector during the years 1992 - 1996 (Run I). The data taking efficiency of the CDF detector is, 75%. We collected data within three sub-periods; Oct. 1992 - Jun. 1993 (Run IA), Feb. 1994 - Jul. 1995 (Run IB), Nov. 1995 - Feb. 1996 (Run Ic). These three data used in this analysis.

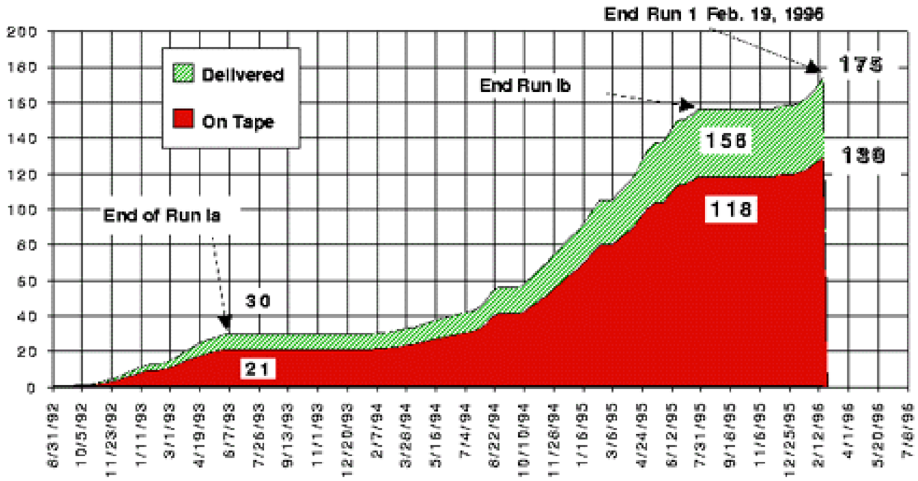

Figure 2.2: The integrate luminosity delivered to the B0 collision point and the corresponding luminosity collected by CDF.

2.2 The CDF detector

The CDF Detector is a multi-purpose detector designed to detect the particles produced in $p\bar{p}$ collisions. Figure 2.3 shows an isometric view of the CDF detector. The detector consists of a 5000 t central detector which made up of the solenoidal magnet, steel yoke, tracking detectors, electromagnetic and hadron calorimeters, and muon chambers, and two identical forward/backward detectors consisting of segmented time-of-flight counters, electromagnetic and hadron calorimeters, and muon toroidal spectrometers [11].

2.2.1 Coordinate system

Figure 2.4 shows a schematic of the rz-view of the detector. In CDF, the positive z is defined along the proton beam direction, the r is transverse to the z direction, θ is the polar angle, and ϕ is the azimuthal angle with respect to the Tevatron plane. The radial distance from the z axis is denoted by r. The pseudo-rapidity η is defined as $\eta = -\ln(\tan\frac{\theta}{2})$, which is an approximation of Lorentz invariant variable, rapidity $\frac{1}{2}\ln(\frac{E+p_z}{E-p_z})$ at high energy $E \approx p$. Transverse energy and momentum are defined by $E_T = E\sin\theta$ and $p_T = p\sin\theta$, respectively. The origin of coordinates is the physical center of the detector, which is the nominal interaction point.

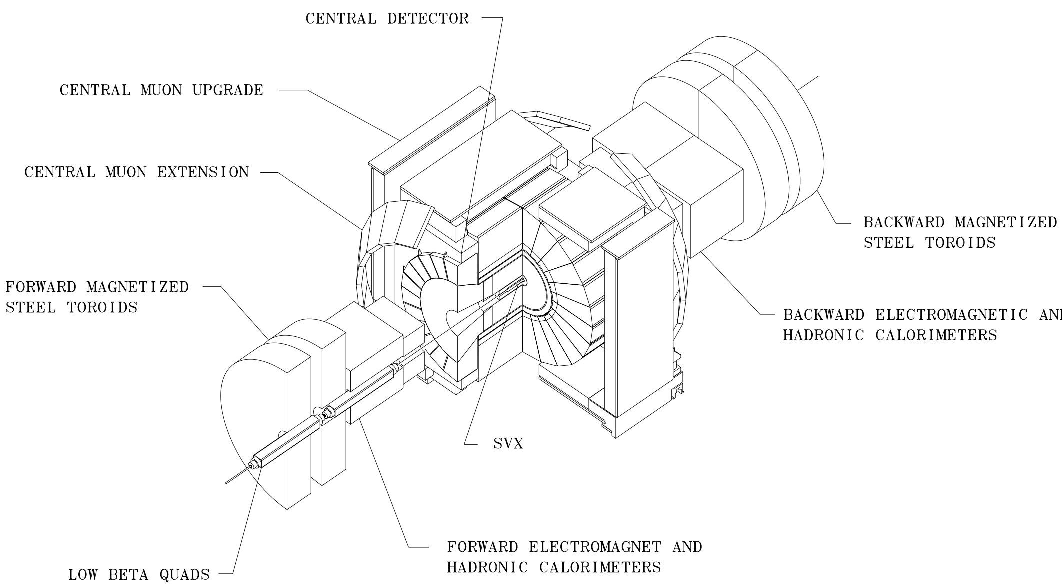

Figure 2.3: An isometric view of the CDF detector.

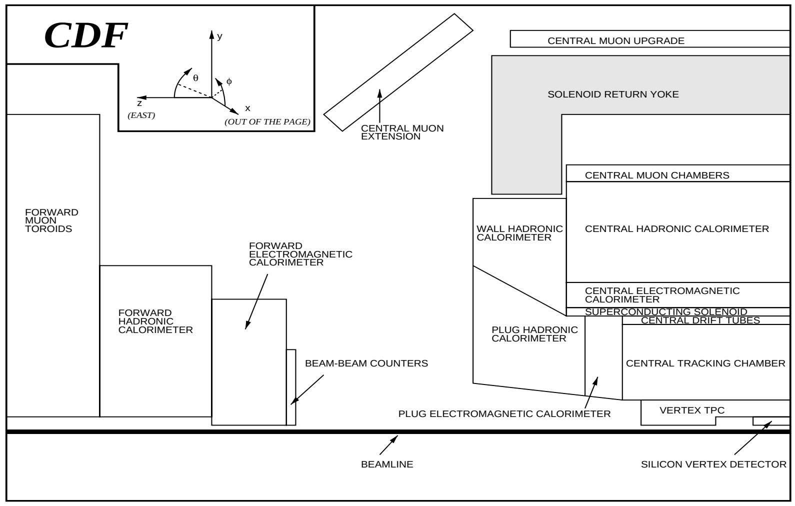

Figure 2.4: A side view cross section of the CDF detector.

2.2.2 Tracking detector

The tracking system in the central region consists of three subsystems, a silicon vertex detector(SVX) [12], a vertex drift chamber(VTX) [13] and a central tracking drift chamber(CTC) [14].

A superconducting solenoid covers the tracking system and generates a 1.4 T magnetic field along the incident beam direction. It allows precise momentum determination of charged particles in the central region.

Superconducting solenoid

The superconducting solenoid magnet coil is 4.8 m long and 1.5 m in radius. The coil is made of 1164 turns of an aluminum-stabilized NbTi/Cu superconductor. The steel magnet yoke is placed outside the central calorimeter to return the magnetic field flux.

Silicon vertex detector (SVX)

The silicon vertex detector(SVX) is a tracking detector closest to an interaction point with surrounding the 1.9 cm radius beam pipe. The SVX is designed to detect the secondary vertices from heavy flavor decay especially b hadrons of which the mean decay length is about 400 μm. The SVX consists of two barrels aligned end-to-end along the z axis. The schematic view of one barrel is shown in Figure 2.5. Each barrel is divided azimuthally into 12 wedges and radially into 4 concentric layers. Each layer contains 3 rectangular strip detectors with a size of 3 cm $\times$ 8.5

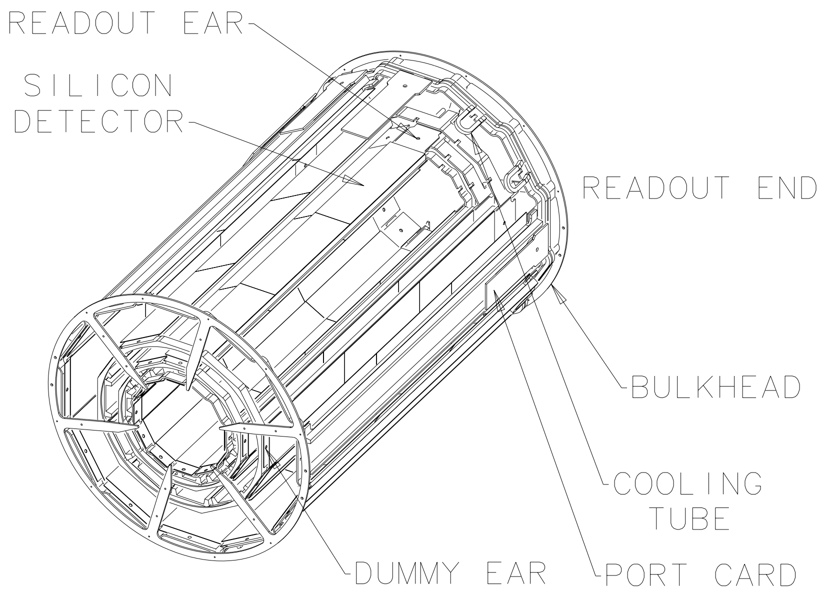

Figure 2.5: An isometric view of the SVX.

cm. The SVX has 46,080 channels which is about one third of all the channels for the whole CDF detector. The strip lines are running parallel to the beam line and provide the hit information in $r-\phi$ plane. The strip pitch is 60 μm for the inner three layers and 55 μm for the fourth layer. The SVX single hit resolution is measured to be 13 μm in $r-\phi$ plane. And the resolution of the impact parameter relative to the primary vertex is 17 μm.

The total coverage of SVX is 51 cm in z direction. The spread of the $p\bar{p}$ collisions is 30 cm in a standard deviation. The SVX detector was used in RUN1A and replaced by the SVX' detector in RUN1B. The SVX' is very similar to the SVX. The SVX' is an AC-coupled device for reducing noise though the SVX is a DC-coupled device. The SVX' is also improved to be more radiation-hard for the higher luminosity.

Vertex drift chamber (VTX)

The vertex drift chamber lies outside the SVX. The VTX consists of 28 modules of octagonal time projection chamber along the z axis. The inner 18 modules contain 16 sense wires perpendicular to the radial direction. The outer 10 modules contain

24 sense wires. It provides tracking information in $r - z$ plane for each of the eight azimuthal sections within $r < 220\ mm$ and $|\eta| < 3.3$. The VTX is primarily used to identify the z position of the primary vertex, that is, event vertex. The event vertex in z direction is determined with a resolution of about 1 mm.

Central tracking chamber (CTC)

The central tracking chamber(CTC) is a 1.3 m in a diameter and 3.2 m long cylindrical drift chamber with 84 layers of sense wires arranged into 9 superlayers. Five of the superlayers, in which the wires are parallel to the beam line, each is composed of the cells of 12 sense wire layers. Four of the superlayers, in which the wires are tilted by $\pm\ 3^\circ$ to the beam line to provide tracking information in z axis, each is composed of the cells of 6 sense wire layers. Each cell is tilted by 45° with respect to the radial direction. Figure 2.6 shows the transverse view at the endplate of the CTC.

The momentum resolution with the combination of SVX and CTC tracking information is given by

$$\delta p_T/p_T = \sqrt{(0.0009p_T)^2 + (0.0066)^2}$$

where p_T is the transverse momentum in GeV/c.

2.2.3 Calorimetry

Particles with p_T greater than 350 MeV/c are able to go out of the solenoid magnet and be detected by the calorimeters. The calorimeters are segmented in azimuth and pseudo-rapidity to form a projective tower geometry which points back to the nominal interaction point. They are separated into three regions in η, the central, plug, and forward. The calorimeters consist of the electromagnetic and hadronic one. The hadron calorimeter is placed outside the electromagnetic one in each region.

Central calorimeter

The central electromagnetic calorimeter (CEM) covers the region of $|\eta| < 1.1$. The central hadron calorimeter (CHA) and the endwall hadron calorimeter (WHA) cover $|\eta| < 0.9$ and $0.7 < |\eta| < 1.3$ respectively. The CEM, CHA and WHA are segmented into 15° in azimuth and 0.1 in η. The CEM consists of alternative layers of a 5 mm thick plastic scintillator as a sampling medium and 3 mm thick lead absorber. The CEM has 31 layers of scintillator and 30 layers of lead. The CEM has the wedges segmented into 15° in azimuth. Each wedge is divided into 10 towers along the z axis. One wedge is notched to allow the access to the coil

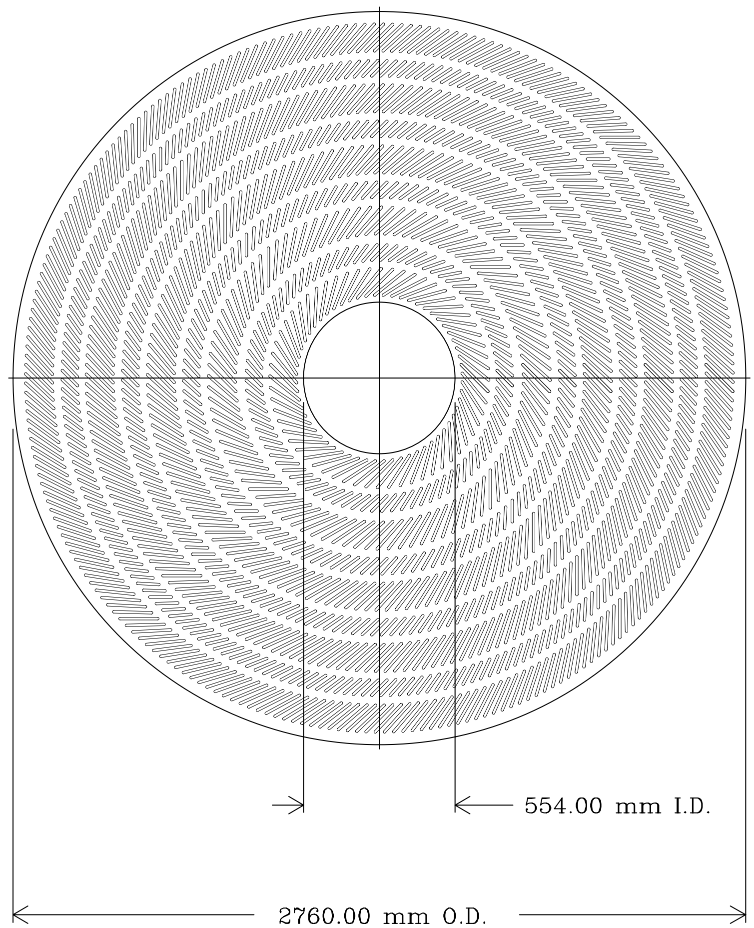

Figure 2.6: An $x-y$ view of the CTC end plate.

and consequently has only 8 towers. Figure 2.7 shows the perspective view of a central calorimeter wedge. The central electromagnetic shower counter (CES) is located at the CEM shower maximum to provide the shower position information in $z - \phi$ view. The CES is a proportional strip and wire chamber. Cathode strips running in azimuthal direction provide the z information and anode wires running in z direction provide the ϕ information. The central preradiator detector (CPR) composed of the proportional chambers is placed between the solenoid and the CEM. The CPR samples the early development of electromagnetic showers and is used to distinguish between electrons and hadrons. The CHA consists of 32 layers of a 1 cm thick plastic scintillator interleaved with 2.5 cm thick steel. The WHA consists of 15 layers of a 1 cm thick plastic scintillator interleaved with 5 cm thick steel. The CHA and WHA have 9 and 6 towers along the z axis segmented into wedge covering 15° in azimuth respectively.

The energy resolution of the CEM is $13.7\%/\sqrt{E_T} \oplus 2\%$ where $\oplus$ means adding in quadrature. The energy resolutions of the CHA and WHA are $50\%/\sqrt{E_T} \oplus 3\%$ and $75\%/\sqrt{E_T} \oplus 4\%$.

2.2.4 Muon system

Muon system consists of three muon chambers, the central muon chamber (CMU), the central muon upgrade (CMP) and the central muon extension (CMX). All of the detectors consist of four layers of rectangular drift tubes with single wire.

Figure 2.8 shows the coverage of muon chambers. The CMU and the CMP cover 84% and 63% of solid angle for $|\eta| < 0.6$, respectively. And 53% of solid angle is covered by both detectors. The CMX covers 71% of solid angle for $0.6 < |\eta| < 1.0$.

Central muon chamber (CMU)

The central muon chamber (CMU) is located directly behind the CHA and covers $|\eta| < 0.6$. Muons with p_T above 1.4 GeV/c can reach the CMU. The CMU is divided into wedges covering 12.6° in azimuth. Each wedge has three towers and each tower contains four layers of four drift tubes. The outer two layers have an offset by 2 mm to resolve the left-right ambiguity of track measurement in azimuth with respect to the two inner layers.

Central muon upgrade (CMP)

The central muon upgrade (CMP) reduces the background of the hadrons which "punched-through" the CMU. Muons with p_T above 2.5 GeV/c can reach the CMP. The CMP is located behind an additional steel of 0.6 m. The CMP consists of a four sided box around the CDF detector.

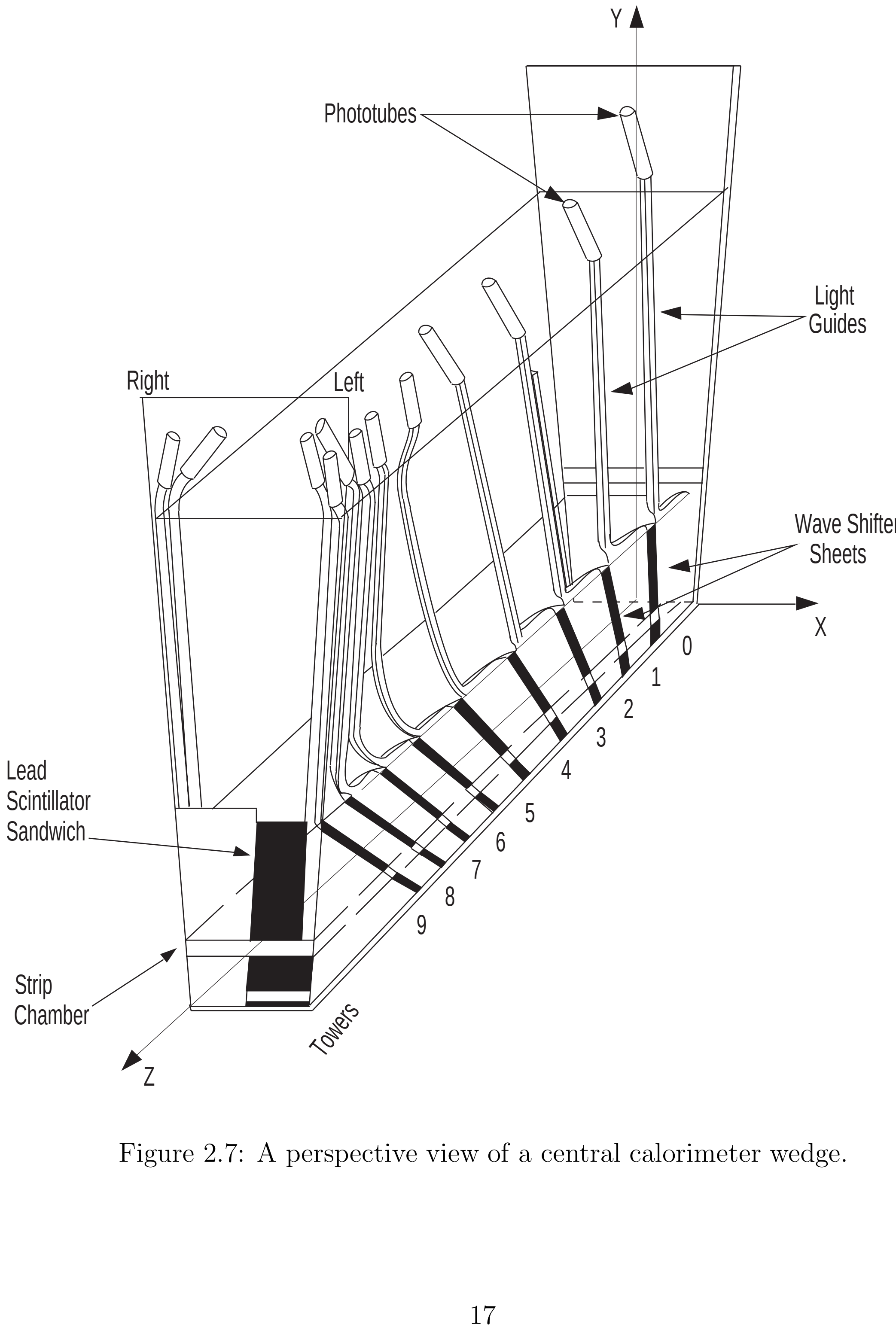

Figure 2.7: A perspective view of a central calorimeter wedge.

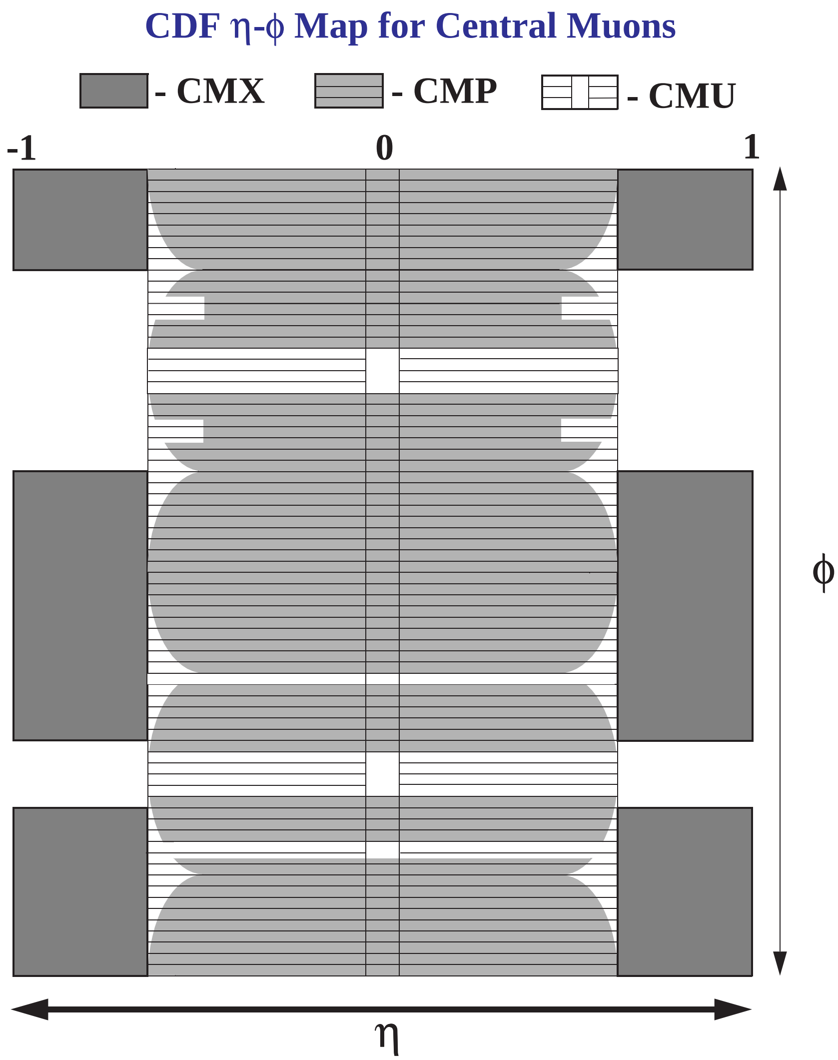

Figure 2.8: A coverage of muon chambers.

Central muon extension (CMX)

The central muon extension (CMX) extends the η coverage of muon chamber up to 1.0. The CMX consists of four conical arches as shown in Figure 2.3.

2.2.5 Trigger

The CDF trigger is formed by a multi-level trigger system to maximize the efficiency of the data taking of interesting events.

The CDF level 1 trigger selects events using the information of calorimeter energies and muon chamber hits. The event rate is reduced down to 1 kHz from 280 kHz by the level 1 trigger requirement.

The level 2 trigger uses the information of tracks and clustered energies. High momentum tracks using CTC hits are reconstructed using the central fast tracker(CFT) of a hardware processor. The calorimeter clusters are formed by searching for a seed tower above a certain threshold and adding neighboring towers. The level 2 output rate is 20-35 Hz. The level 2 decision takes about 20 μs and incurs a dead time of a few percent.

The level 3 trigger is a software reconstruction trigger on a farm of Silicon Graphics processors. All events which pass the level 3 trigger are written to 8 mm tape. The level 3 output rate is 5-10 Hz. In this thesis we use the same triggers of a high p_T electron or muon and $\not{E}_T$ as in the $t\bar{t}$ events analysis [15, 16].

Chapter 3

Event selection

We collected the data corresponding to an integrated luminosity of 106.0 ± 4.1 pb^{-1} with the CDF detector in 1992-1996 which we call Run1 data. In this analysis, we used this full data to select candidates of W boson pair production. The signal has one high p_T lepton, large missing transverse energy $\not\!\!E_T$ and two high E_T jets. In Section 3.1, we describe the kinematic variables that are used in the event selection and data analysis.

Starting with the events which pass the level 3 trigger for high E_T electron or high p_T muon and $\not\!\!E_T$, we apply additional selection criteria for high E_T electron or high p_T muon described in Section 3.2 and 3.3 and large $\not\!\!E_T$. We remove the dilepton events to reject the backgrounds from Z boson and $t\bar{t}$ production as described in Section 3.5. To suppress W + QCD jets background, we also require that the events have just two high E_T jets.

3.1 Event variables

In this section, we describe the kinematic variables used in this analysis.

3.1.1 E_T : Electron transverse energy

The electron E_T is defined as $E \times \sin\theta$ where E is the energy of the electromagnetic cluster, and $\sin\theta = 1/\sqrt{1 + \cot\theta^2}$. The $\cot\theta$ is calculated for the beam constrained track, which is discussed immediately below. The cluster energy is the sum of the electromagnetic energies of a CEM seed tower, which is any tower with energy above 5 GeV, and its two neighboring towers in the z direction. If the seed tower borders the 90° crack, then only one neighboring tower is used, so that the cluster is not allowed to cross the 90° crack. The cluster is always 1 tower wide in azimuth.

3.1.2 p_T : Muon track momentum and beam constraint

We identify muons in the pseudorapidity region $|\eta| < 1.0$ by requiring a match between a CTC track and a track segment in the muon chambers of CMU, CMP or CMX and the track momentum is estimated from the curvature of this CTC track. The muon p_T is defined as $p \times \sin\theta$ where p is a momentum for the beam constrained track and $\sin\theta = 1/\sqrt{1+\cot\theta^2}$. The $\cot\theta$ is calculated for the beam constrained track.

The beam constraint would be to re-fit the track with the beam spot added as an additional point, which improves the track resolution.

3.1.3 $\not\!\!E_T$: Missing transverse energy

The missing transverse energy ($\not\!\!E_T$) is defined to be the negative of the vector sum of transverse energy in all calorimeter towers with $|\eta| < 3.6$. The η range is restricted because the final focusing magnets of the Tevatron obscure parts of the forward hadron calorimeter. To be included in the sum, individual tower energies (E, not E_T) must exceed detector-dependent energy thresholds. These thresholds are 100 MeV in the CEM, CHA and WHA, 300 MeV in the PEM, 500 MeV in the PHA and FEM, and 800 MeV in the FHA. For events with muon candidates, the vector sum of the calorimeter transverse energy is corrected by vectorially subtracting the energy deposited by the muon and then adding the p_T of the muon candidate as measured in the CTC. This is done for muons passing the high p_T threshold. The $\not\!\!E_T$ resolution is given approximately by $0.7\sqrt{\sum E_T}$, where $\sum E_T$ is the scalar sum of the transverse energy measured in units of GeV.

3.2 High p_T electron selection

High p_T electron must be in the central region($|\eta| < 1.0$) and have a CTC track pointing to an electromagnetic cluster in CEM. We apply the following cuts to the electron candidates:

- The transverse energy: $E_T > 20$ GeV
- The ratio of the cluster energy to the track momentum: $E/p < 1.8$
- The ratio of the hadronic energy to the electromagnetic energy of the cluster: $\frac{HAD}{EM} < 0.05$
- A comparison of lateral shower profile in the calorimeter with that measured at the test beam: $Lshr < 0.2$

- A χ^2 comparison of the CES shower profile with that measured at test beam: $\chi^2_{strip} < 10$

- The distance between the interaction vertex and the reconstructed track in the z direction: $|Z_v - Z_0^e| < 5$ cm

- The z position of the interaction vertex: $|Z_v| < 60$ cm

- Fiducial cuts on the electron: Fiducial volume for the electron covers 84% of the solid angle in the region $|\eta| < 1.0$

- Photon conversion Removal: If the candidate electron and the partner electron pass the following requirements, the candidate is removed.

  - The difference in the cotangent of the polar angle: $|\Delta \cot \theta| < 0.06$
  - The separation of the two tracks at the point of tangency in $r - \phi$ plane: $|\Delta(r - \phi)| < 0.3$ cm
  - The radial distance between the conversion point and the origin: $-20 < R_c < 50$ cm or
  - VTX occupancy < 0.2 for the primary electron: The VTX occupancy is defined as the ratio of the number of VTX hits found to that expected. If fewer than three hits are expected, the VTX occupancy is defined to be one.

- The distance between the position of the extrapolated track and the CES shower position measured in the $r - \phi$ views: $|\Delta x| < 1.5$ cm, $|\Delta z| < 3.0$ cm

- Electron isolation: The ratio of $E'_{0.4}$ to E_T of the electron cluster, where $E'_{0.4}$ is defined as a sum of E_T's in towers within a cone of radius $R \equiv \sqrt{(\Delta\phi)^2 + (\Delta\eta)^2}$ of 0.4 centered on the electron but excluding the electron cluster E_T. $I_{0.4} < 0.1$ where $I_{0.4} \equiv \frac{E_T(0.4) - E_T(EM)}{E_T(EM)}$

3.3 High p_T muon selection

High p_T muon must have a CTC track matched to a track segment in the muon chambers and have as much energy deposition in the calorimeters as a minimum ionizing particle. We apply the following cuts to the muon candidates:

- The transverse momentum: $p_T > 20$ GeV/c

- The electromagnetic energy: $EM < 2.0$ GeV

- The hadronic energy: $HAD < 6.0$ GeV
- EM + HAD energy: EM + HAD > 0.1 GeV
- The distance between the interaction vertex and the reconstructed track in the z direction: $|Z_v - Z_0^\mu| < 5$ cm
- The z position of the interaction vertex: $|Z_v| < 60$ cm
- The impact parameter of the reconstructed track to the beam line: $|d_0| < 0.3$ cm
- The distance between the position of the extrapolated track and the track segment in the muon chamber: $|\Delta x| < 2.0$ cm for CMU or $|\Delta x| < 5.0$ cm for CMP and CMX.
- Muon isolation: $I_{0.4} < 0.1$ where $I_{0.4} \equiv \frac{E_T(0.4) - E_T(\mu\ tower)}{p_T(track)}$

3.4 Missing transverse energy

- $\not{E}_T > 20$ GeV

3.5 Z boson production and dilepton events removal

The second electron in high p_T electron sample($Z \to ee$)

- The transverse energy: $E_T > 10$ GeV
- The ratio of the cluster energy to the track momentum: $E/p < 2.0$
- The ratio of the hadronic energy to the electromagnetic energy of the cluster: $\frac{HAD}{EM} < 0.12$
- Electron isolation: $Calorimeter\ I_{0.4} < 0.2$

The second muon in high p_T muon sample($Z \to \mu\mu$)

- The transverse momentum: $p_T > 10$ GeV/c
- The electromagnetic energy: $EM < 5.0$ GeV$(CMU/CMP/CMX); EM < 2.0$ GeV $(CMIO)$

- The hadronic energy: $HAD\ <\ 10.0$ GeV $(CMU/CMP/CMX); HAD\ <$ 6.0 GeV $(CMIO)$

- The distance between the position of the extrapolated track and the track segment in the muon chamber: $CMU : |\Delta x|\ <\ 5.0$ cm or $CMP : |\Delta x|\ <\ 5.0$ cm or $CMX : |\Delta x|\ <\ 5.0$ cm

- Muon isolation: $Calorimeter\ I_{0.4}\ <\ 0.2$

- The detector η cut: $|\eta|\ <\ 1.2(CMIO)$

Finally, if the invariant mass of the lepton pair is between 75 and 105 GeV/c^2, then the event is flagged as a Z.

For $t\bar{t}$ background reduction, we remove dilepton events, which have two leptons(e or μ) with $p_T\ >\ 20$ GeV/c, high $\not{E}_T >\ 25$ GeV, and two jets with $E_T\ >\ 10$ GeV. Dilepton events which contain an isolated track with $p_T\ >\ 15$ GeV/c and an opposite sign of the electric charge to the primary lepton. The track isolation requirement is $\Sigma p_T\ <\ 2.0$ GeV/c in an cone radius of 0.4 around the lepton candidate track.

3.6 Jet identification

Jets are reconstructed as an energy cluster with a cone radius of 0.7 in $\eta - \phi$ space. First we find seed towers with $E_T\ >\ 1$ GeV. Preclusters are formed from seed towers which is adjacent each other and the E_T weighted center of the preclusters is calculated. Then we combine towers with $E_T\ >\ 0.1$ GeV which are in a cone radius of 0.7. The center of the cluster is recalculated until the set of the towers in a cluster does not change.

The jet energy may be mismeasured due to the effects, calorimeter no-linearity, out of cone losses, contributions from the underlying event, undetected energy carried by muons or neutrinos, curvature of low momentum charged particles by the CDF magnetic field, reduced calorimeter subsystems. We correct the jet energy by applying the correction factors which depend on the jet E_T and η to reproduce the average jet E_T correctly, not to reduce the jet fluctuations around this mean E_T. Estimates of the uncertainty in our knowledge of the reconstructed jet E_T due to detector effects range from 5% for 20 GeV corrected jets to 3% at 300 GeV.

It is possible to check the energy scale set by the jet energy corrections using the direct photon data sample. This contains a subset of two-jet events for which most of the energy of one jet is carried by a single γ, π^0 or η, and is fully contained in the CEM calorimeter where the energy scale is well understood.

We define two subsamples of the W sample. The first subsample passes tight jet cuts and is our *WW search sample*, whereas the second one passes looser jet cuts and is our *control sample*. The tight and loose jet cuts are listed in the table below:

Selection variable	WW search sample	Control sample
$\|\eta_{detector}\|$ range used for counting jets	≤ 1.1	≤ 2.0
# of jets required in above range	exactly 2	exactly 2
Uncorrected E_T of jet 1	≥ 20 GeV	≥ 15 GeV
Uncorrected E_T of jet 2	≥ 15 GeV	≥ 15 GeV
Electron proximity	$\Delta R(e, \text{jet}) \geq 0.5$	$\Delta R(e, \text{jet}) \geq 0.5$
Missing-E_T proximity	$\Delta\phi(\not{E}_T, \text{jet}) \geq 0.2$	$\Delta\phi(\not{E}_T, \text{jet}) \geq 0.2$
Dijet opening angle	$\Delta R(\text{jet}, \text{jet}) \geq 1.4$	no cut

Distributions of uncorrected jet E_T, jet $\eta_{detector}$, and dijet opening angle for both WW search and control samples are shown in Figures 3.1 to 3.5.

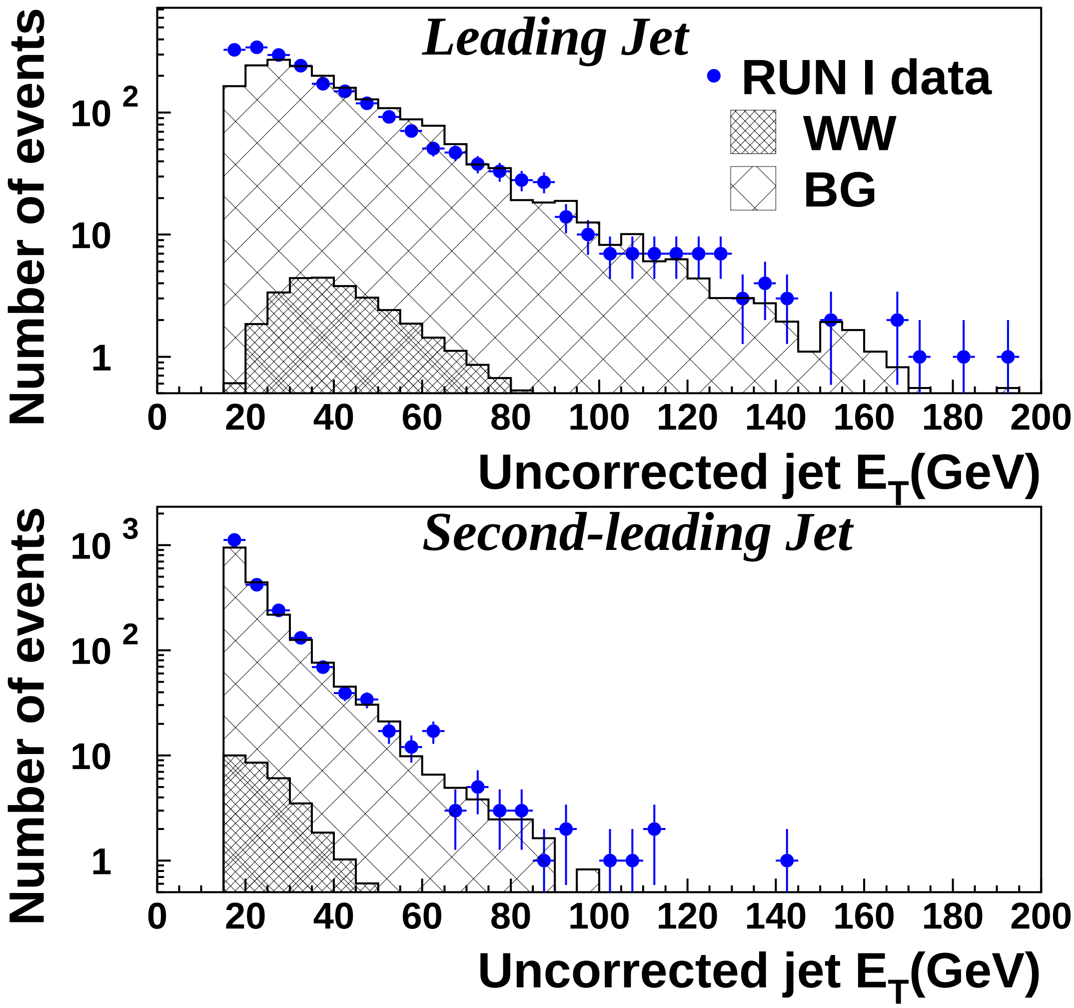

Figure 3.1: Uncorrected transverse jet energy distributions for CDF data and Monte Carlo simulations after loose jet selection. Top: leading jet E_T; bottom: second-leading jet E_T. Signal and background events were generated with PYTHIA and VECBOS respectively.

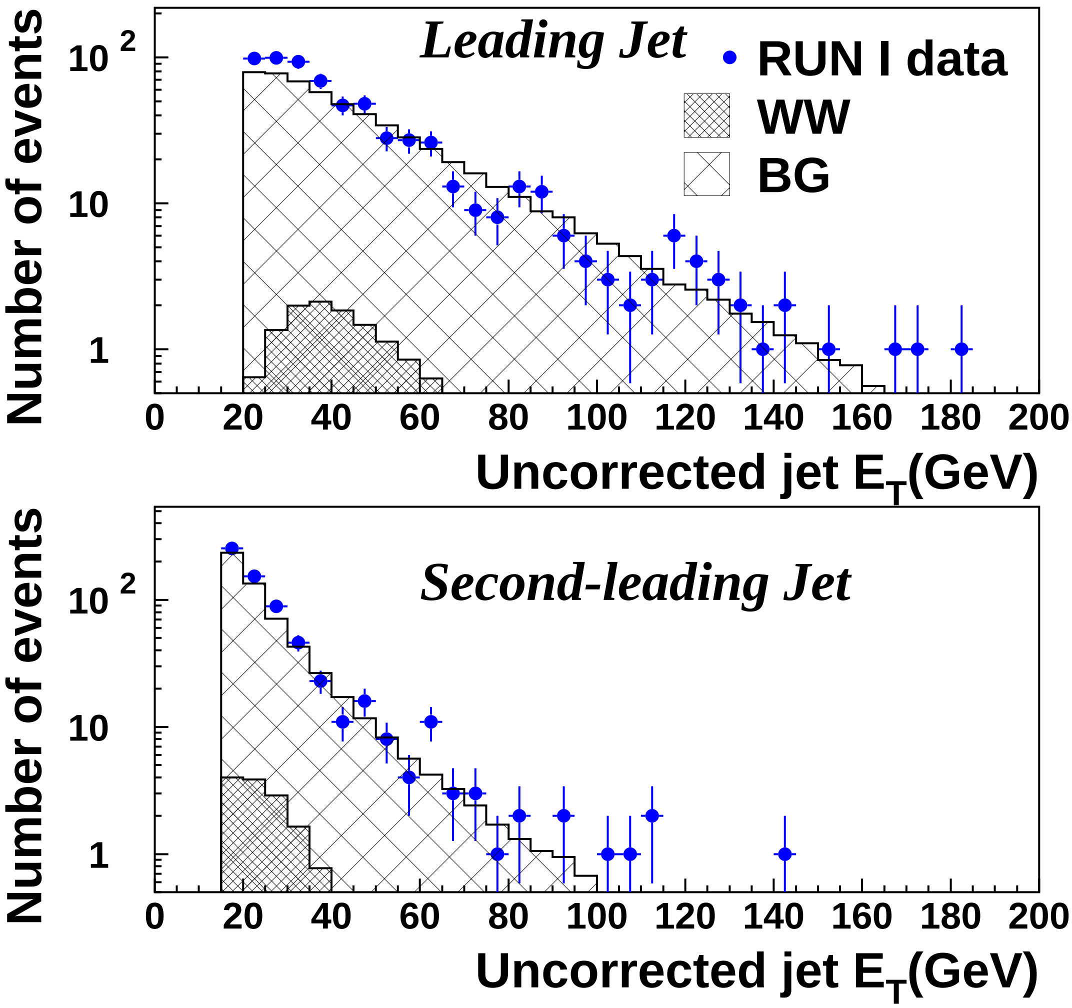

Figure 3.2: Uncorrected transverse jet energy distributions for CDF data and Monte Carlo simulations after tight jet selection. Top: leading jet E_T; bottom: second-leading jet E_T. Signal and background events were generated with PYTHIA and VECBOS respectively.

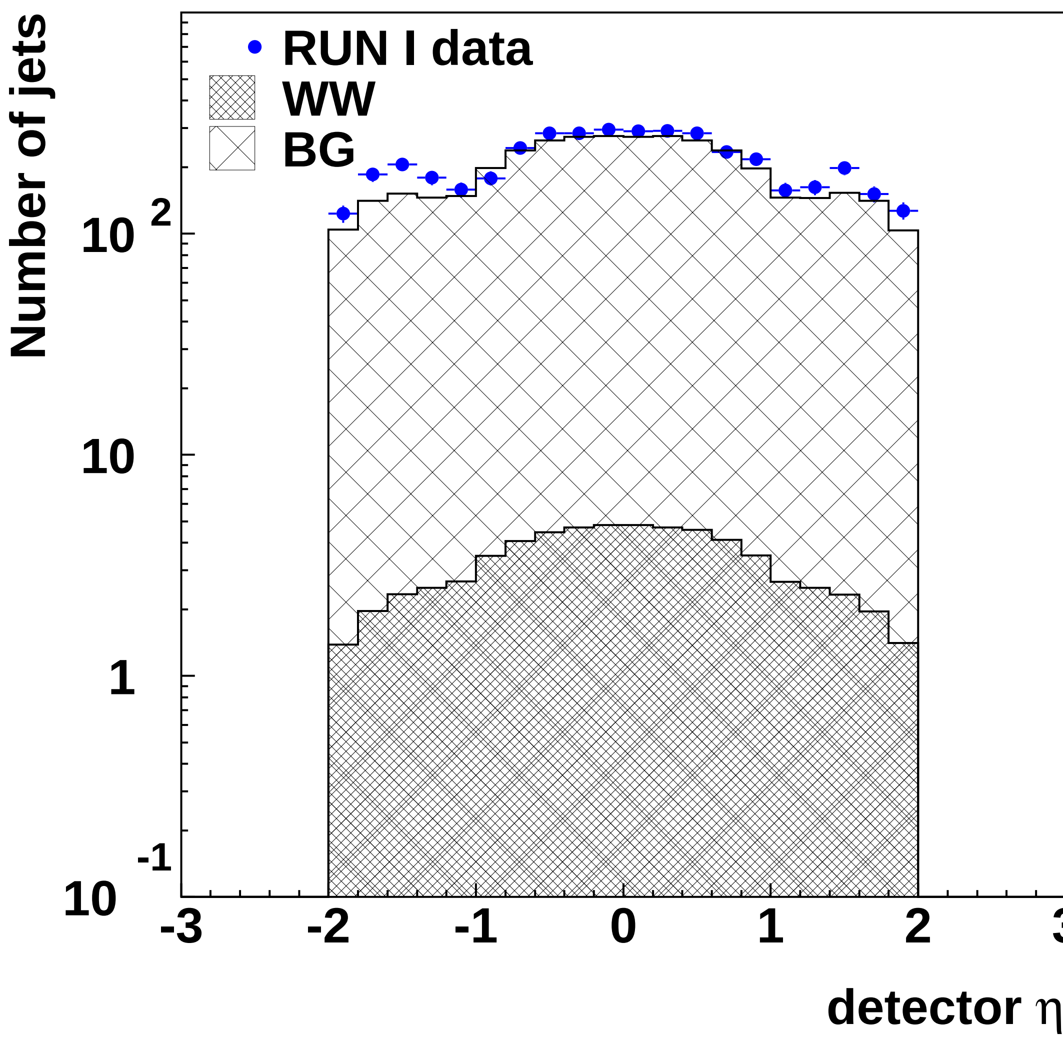

Figure 3.3: Detector η of jets for CDF data and Monte Carlo simulations after loose jet selection. Signal and background events were generated with PYTHIA and VECBOS respectively.

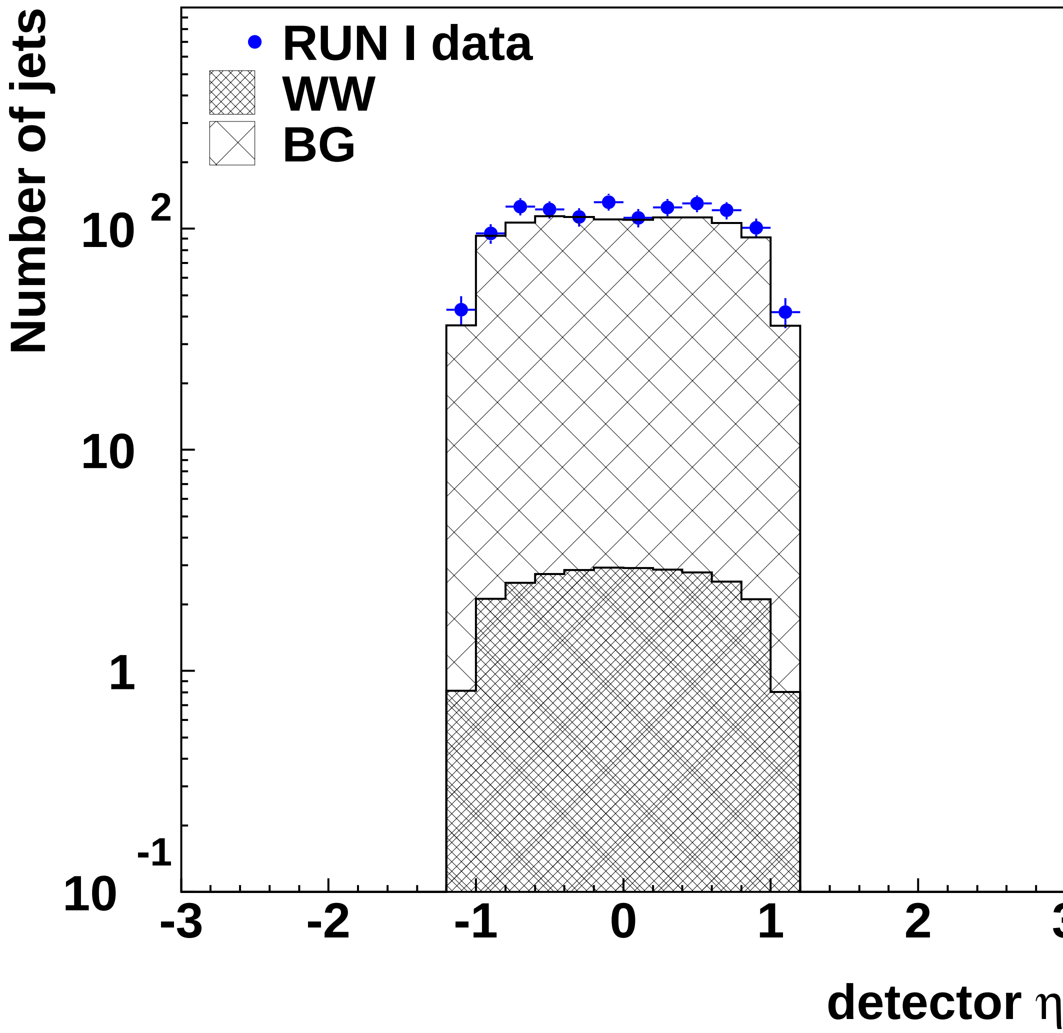

Figure 3.4: Detector η of jets for CDF data and Monte Carlo simulations after tight jet selection. Signal and background events were generated with PYTHIA and VECBOS respectively.

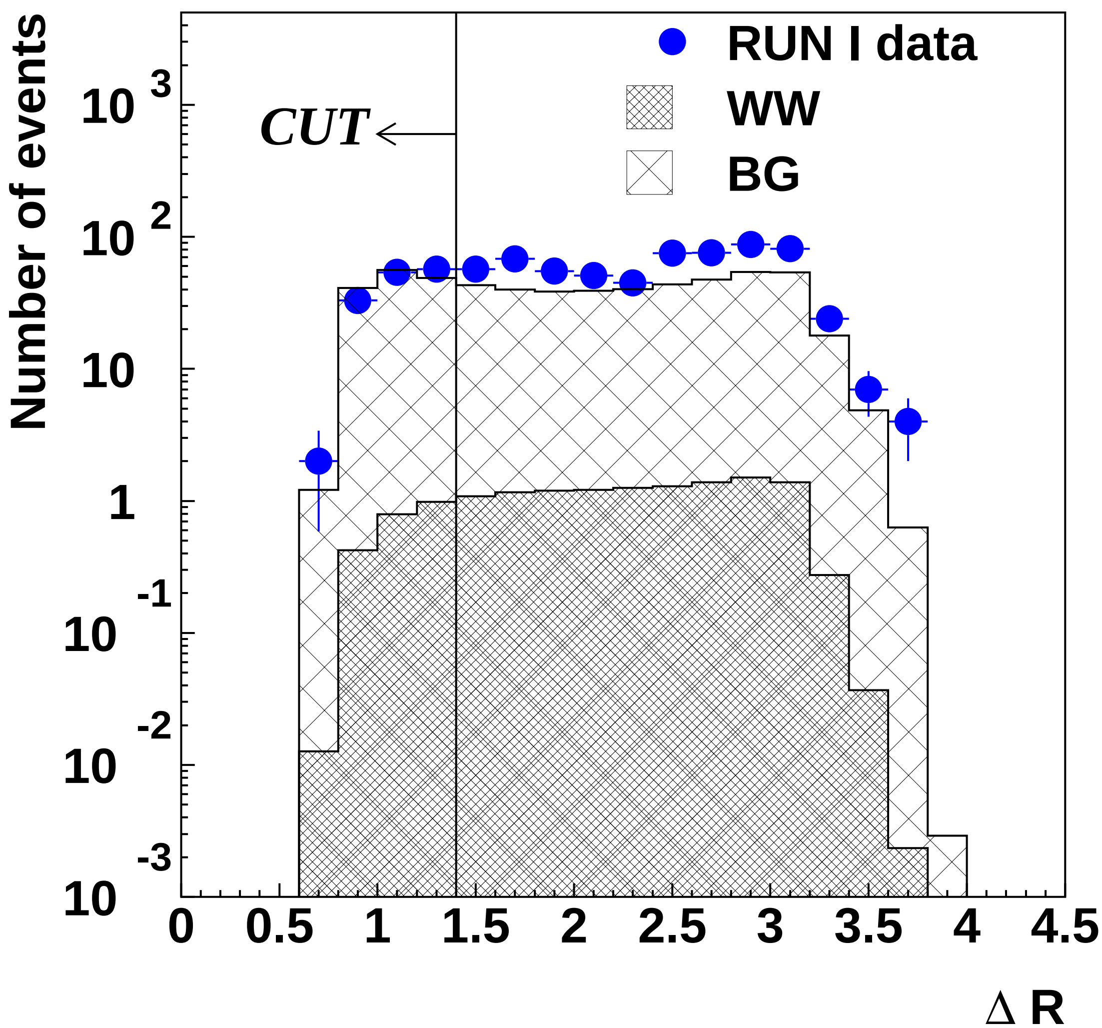

Figure 3.5: Dijet opening angle for CDF data and Monte Carlo simulations after tight jet selection. Signal and background events were generated with PYTHIA and VECBOS respectively.

Chapter 4

Backgrounds and signal estimation

To model the signal and background events we use Monte Carlo(MC) simulations. PYTHIA Monte Carlo simulation package [17, 18] is our modeling of the W^+W^- signal events. PYTHIA is based on the leading order QCD matrix elements, and partons are fragmented using Lund string model without parton shower evolution. We use VECBOS [19] for a modeling of the $W + QCD\ jets$ background events. VECBOS is a parton-level Monte Carlo simulation based on a tree-level matrix element calculation. HERWIG Monte Carlo simulation [20, 21] is used for a modeling of the top background events. HERWIG is based on the leading order QCD matrix elements followed by parton shower evolution and parton fragmentation according to a cluster model. CLEOMC [22] is used in all Monte Carlo generator for the b-hadron decays. The CDF detector simulation called QFL' is performed after the event generation. We apply the same selection criteria as applied to RUNI data samples as described in chapter 3.

The lepton identification efficiency in the Monte Carlo samples has been checked by a Run I data. Table 4.1 compares lepton identification efficiencies extracted from the PYTHIA sample with those obtained from Z data by the top dilepton group [23]. Similar results were obtained for VECBOS and HERWIG.

Table 4.1: Lepton identification efficiencies, in percentages, from the W^+W^- PYTHIA sample and CDF Run 1 Z data. All uncertainties are statistical only.

Category	PYTHIA W^+W^-	Run 1 Z data
CE	82.0 ± 0.6	81.3 ± 0.9
CMU/CMP	92.7 ± 0.5	92.3 ± 1.4
CMX	94.1 ± 0.7	95.2 ± 1.1

In the following subsections we provide more details on the simulation and normalization of each process that is relevant to our analysis.

4.1 W + QCD jets

W + 2jets and Wc background events were generated with VECBOS(v3_00) and then we used HERWIG for a fragmentation of partons. In VECBOS, we applied the following cuts:

$$\begin{array}{rcl} p_T \text{ (jets)} & > & 5 \text{ GeV}/c \\ |\eta_{detector}| \text{ (jets)} & < & 3.5 \\ |\Delta\eta| \text{ (jets)} & > & 0.4 \\ p_T \text{ (lepton)} & > & 10 \text{ GeV}/c \\ |\eta| \text{ (lepton)} & < & 1.5 \\ p_T \text{ (neutrino)} & > & 5 \text{ GeV}/c \end{array}$$

The Q^2 scale was set to the square of the average parton p_T and the CTEQ-4M parton distributions were used. The generated events were unweighted by routine UNWT, bottom and charm particles were decayed with the CLEO Monte Carlo QQ v9.1, and partons were fragmented with HERPRT. The W + 2jets cross section calculated by VECBOS with the above settings is 610 ± 6 pb. Based on reference [24], we multiply this cross section by a Q^2-scale dependent correction factor $R = 1.25 \pm 0.10$.

The fraction of W + 2jets events that contain a charm-jet is $(6.4 \pm 0.1)\%$, in agreement with the $t\bar{t}$ production cross section analysis, which found $(7.2 \pm 2.2)\%$ (Table XXVIII in [25]).

4.2 $Wb\bar{b}$

The $Wb\bar{b}$ background was generated by VECBOS with the "force $b\bar{b}$" option. We normalized this sample relatively to the W + 2jets sample, in two steps. First we note that the jet selection for the control sample is identical to that in reference [26]. Therefore, the expected number $N^{\text{loose}}_{Wb\bar{b}}$ of $Wb\bar{b}$ events in the control sample can be set equal to $f_{b\bar{b}}$ times the expected number of W+2jets events in that sample, where $f_{b\bar{b}} = (0.85 \pm 0.25)\%$ [26]. In the second step we multiply $N^{\text{loose}}_{Wb\bar{b}}$ by the efficiency of the tight jet selection relative to the loose jet selection in the $Wb\bar{b}$ sample.

4.3 $Wc\bar{c}$

The $Wc\bar{c}$ background is generated by VECBOS with the "force $b\bar{b}$" option and subsequent replacement of $b\bar{b}$ and $c\bar{c}$. We normalized this sample in the same way as the $Wb\bar{b}$ sample, using a fraction $f_{c\bar{c}} = (1.04 \pm 0.27)\%$ ([26]).

4.4 $t\bar{t}$

The $t\bar{t}$ background is generated with HERWIG(v5_6). We made $t\bar{t} \to W^+W^-b\bar{b}$ events with a top mass $M_{top} = 175$ GeV/c^2. This sample was normalized to a cross section of $\sigma(p\bar{p} \to t\bar{t}) = 5.1 \pm 0.4$ pb [27].

4.5 Single top

At the Tevatron, single top production is dominated by two processes: s-channel W^* exchange, and t-channel W-gluon fusion. We generated both processes with HERWIG and forced the top quark to decay in the $t \to b\ell\nu$ channel. The s- and t-channel samples were normalized to cross sections of 0.73±0.10 pb [28] and 1.70±0.29 pb [29], respectively.

4.6 Non-W

The non-W background has been studied in many previous analyses. For example, a 1993 study finds the non-W contamination in $W(\to \ell\nu)+ \geq 2$jets events with $\not{E}_T \geq 25$ GeV to be $3.6 \pm 1.2\%$ in the electron channel and $4.0 \pm 1.0\%$ in the muon channel. In our analysis the missing E_T threshold is somewhat lower, so that we expect the non-W fractions to be a little larger. We use the same method as this previous study, namely the "Isolation versus $\not{E}_T$ Method". At first, we make two samples enriched in QCD multijets by removing the lepton isolation and $\not{E}_T$ cuts from the control and search samples respectively. In order to estimate the amount of non-W background in the latter samples, we make "Isolation vs $\not{E}_T$" plots and divide them into four regions (see diagram below):

Region A: $Iso < 0.1$ and $\not{E}_T < 10$ GeV

Region B: $Iso > 0.3$ and $\not{E}_T < 10$ GeV

Region C: $Iso > 0.3$ and $\not{E}_T > 20$ GeV

Region D: $Iso < 0.1$ and $\not{E}_T > 20$ GeV (W sample)

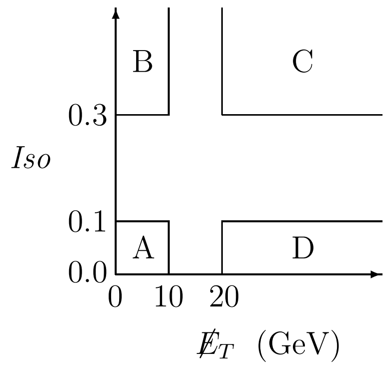

Assuming that the distribution of the isolation variable for fake electrons (misidentified QCD jets) is independent of $\not\!\!E_T$ (as suggested by Figures 4.1 and 4.2), the ratio N_A/N_B of the numbers of isolated to non-isolated events in the low $\not\!\!E_T$ region can be extrapolated into the high $\not\!\!E_T$ region. The number of non-W events in region D (N_{non-W}) is therefore given by:

$$N_{non-W} = R \times N_C, \quad (4.1)$$

$$\text{where}: \quad R = \frac{N_A}{N_B} \quad (4.2)$$

The results of this calculation are summarized in Table 4.2.

Table 4.2: Calculation of the non-W background contamination in the control and search samples.

	Control sample		Search sample	
	$e + 2$jets	$\mu + 2$jets	$e + 2$jets	$\mu + 2$jets
N_A	575	395	171	117
N_B	828	3685	202	2223
N_C	101	345	22	185
N_D	1135	990	323	308
R	0.69	0.11	0.85	0.05
N_{non-W}	70	37	18.6	9.7
Non-W fraction (%)	6.2	3.7	5.8	3.2

4.7 W pair signal

W^+W^- signal events are generated by PYTHIA v5.7, and forced into the decay mode $WW \rightarrow \ell\nu q\bar{q}'$. The W^+W^- sample is normalized to a cross section of $9.6^{+0.3}_{-0.9}$

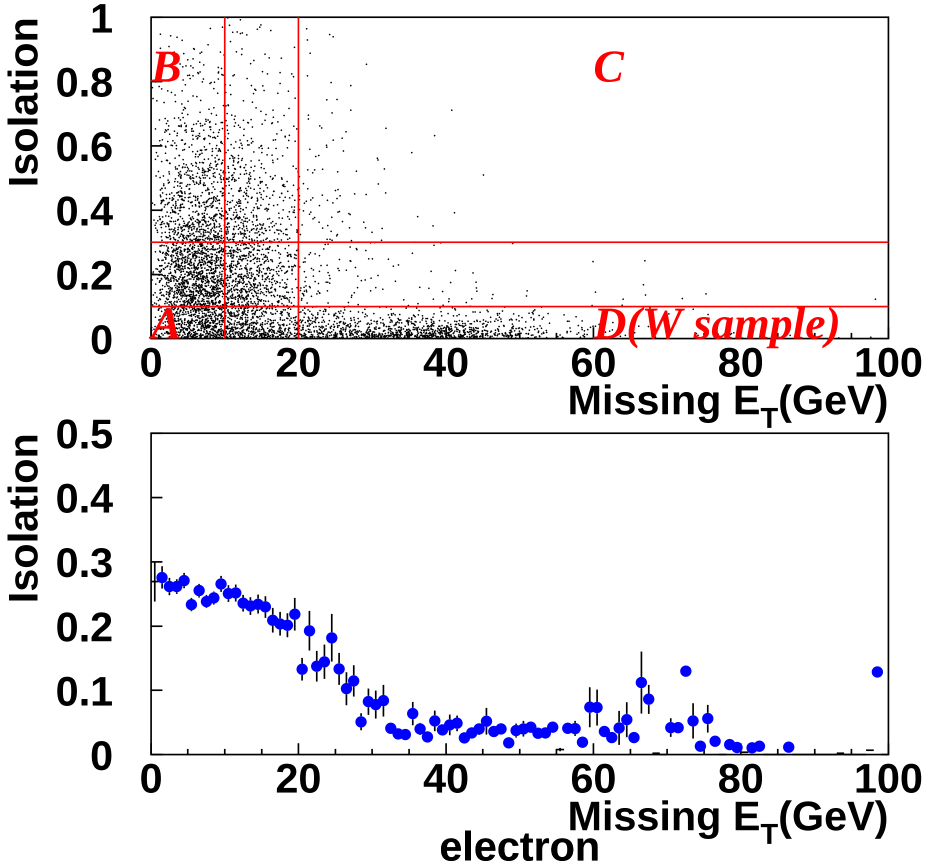

Figure 4.1: Upper plot shows the Isolation vs $\not\!\!E_T$ for enriched Non-W sample(electron channel) after loose jet ID. Lower plot shows the profile of upper plot. The high missing energy events show the low isolation of W electrons and our W sample include QCD jets contamination.

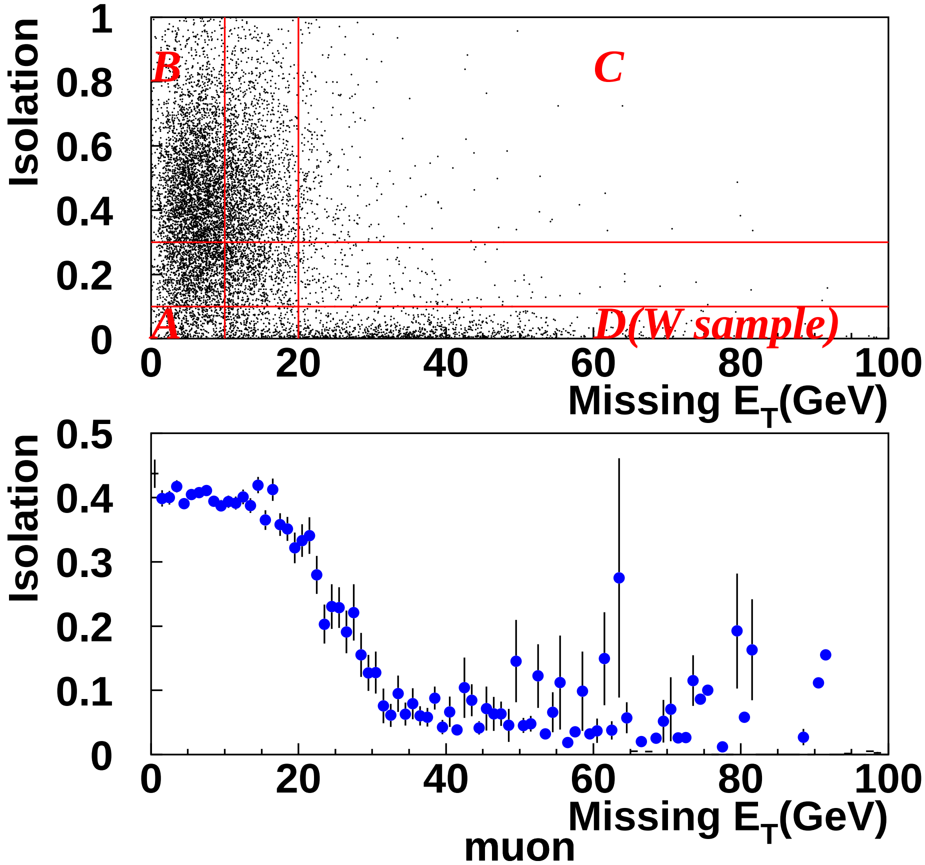

Figure 4.2: Upper plot shows the Isolation vs $\not{E}_T$ for enriched Non-W sample(muon channel) after loose jet ID. Lower plot shows the profile of upper plot.The high missing energy events show the low isolation of W muons and our W sample include QCD jets contamination.

pb [30].

Some W^+W^- events include QCD jets from initial or final state gluon radiation. When these QCD jets pass the jet selection cuts and become one of the two leading jets, the corresponding events broaden the dijet mass distribution in the W^+W^- final state, thereby reducing the sensitivity of the analysis. According to the Monte Carlo simulation, the fraction of events with such mislabeled leading jets is 21% in the control sample.

4.8 Event yields for W + 2jets events

We estimate the number of expected signal and background events using the CDF data and simulation. We use a VECBOS cross section correction factor R(=1.25) for the QCD W + n jets background as described in the previous analysis [24].

The number of signal events N_{signal} is obtained as

$$N_{signal} = \sum_{ch=e,\mu} \mathcal{L} \cdot \sigma(WW) \cdot BR(WW \to l\nu qq) \cdot \varepsilon^{ch}(WW)$$

where $\mathcal{L}$ is an integrated luminosity, $\sigma(WW)$ is the WW production cross section, $BR(WW \to l\nu qq)$ is the branching ratio of $WW \to l\nu qq$ decay, and $\varepsilon^{ch}(WW)$ is the number of events passing the selection criteria over the number of generated events.

The dominant background process is the QCD W+n jets. We also consider the other backgrounds of Non-W, $t\bar{t}$, single top productions, $Wb\bar{b}$ and $Wc\bar{c}$. Each number of background events is given by

$$\begin{aligned}
N_{WW} &= \sum_{ch=e,\mu} \mathcal{L} \cdot \sigma_{WW} \cdot BR(WW \to l\nu qq) \cdot \varepsilon^{ch}_{WW} \\
N_{W+2jets} &= \sum_{ch=e,\mu} \mathcal{L} \cdot R \cdot \sigma_{W+\geq 2jets} \cdot BR(W \to l\nu) \cdot \varepsilon^{ch}_{W+2jets} \\
N_{t\bar{t}} &= \sum_{ch=e,\mu} \mathcal{L} \cdot \sigma_{t\bar{t}} \cdot \varepsilon^{ch}_{t\bar{t}} \\
N_{single\ top} &= \sum_{ch=e,\mu} \mathcal{L} \cdot \sigma_{single\ top} \cdot BR(t \to bl\nu) \cdot \varepsilon^{ch}_{single\ top} \\
N_{Wb\bar{b}} &= \sum_{ch=e,\mu} \mathcal{L} \cdot \sigma_{Wb\bar{b}} \cdot BR(W \to l\nu) \cdot \varepsilon^{ch}_{Wb\bar{b}} \\
N_{Wc\bar{c}} &= \sum_{ch=e,\mu} \mathcal{L} \cdot \sigma_{Wc\bar{c}} \cdot BR(W \to l\nu) \cdot \varepsilon^{ch}_{Wc\bar{c}} \\
N_{Wc} &= \sum_{ch=e,\mu} \mathcal{L} \cdot R \cdot \sigma_{Wc} \cdot BR(W \to l\nu) \cdot \varepsilon^{ch}_{Wc}
\end{aligned}$$

where the following production cross sections are used: $\sigma(WW)$=9.6 pb [30] and $\sigma(t\bar{t})$ = 5.1 pb [27] are theoretically predicted for W pair production and top pair production, respectively. In $t\bar{t}$ production, W bosons decay to all possible modes. $\sigma(W+\geq 2jets)$ = 0.61 nb is the result of VECBOS output as listed in Table 4.3. Single top production have 2 processes. One is the s-channel W^* exchange process and another is the boson-gluon fusion(BGF). $\sigma(t;W^*) = 0.7\ pb$ [28] , $\sigma(t;BGF) = 1.7\ pb$ [29]. $\sigma(W(\rightarrow e\nu) + b\bar{b}) = 3.2\ pb$ and $\sigma(W(\rightarrow e\nu) + c\bar{c}) = 3.3\ pb$ [26] are expected from VECBOS. The number of Non-W background events is obtained from RUN I data sample. The total number of background events N_{BG} is given by $N_{BG} = N_{BG}(W + 2jets) + N_{BG}(Non - W) + N_{BG}(t\bar{t}) + N_{BG}(single\ top) + N_{BG}(Wb\bar{b}) + N_{BG}(Wc\bar{c})$.

The signal fraction S/BG and the signal significance $S/\sqrt{BG}$ are given by

$$S/BG = \frac{N_{signal}}{N_{BG}}$$

and

$$S/\sqrt{BG} = \frac{N_{signal}}{\sqrt{N_{BG}}}$$

Tables 4.4 summarize the number of expected signal and each background events for electron and muon channel separetely.

Table 4.3: Cross section of W + QCD jets event from VECBOS output.

# of jets	$\sigma(Q^2 =< p_t >^2)$ (nb)
≥ 2	0.61

Table 4.4: Expected numbers of signal and background events in the control (loose jet cuts) and search (tight jet cuts) samples; ε_1 = (Number of events in control sample)/(Number of generated events); ε_2 = (Number of events in search sample)/(Number of events in control sample).

	Control sample				Search sample			
	e	μ	Total	ε_1(%)	e	μ	Total	ε_2(%)
$W+2jets$	875.55	784.14	1659.69	1.02	248.30	235.32	483.61	29
$Non-W$	70.14	36.98	107.12	N/A	18.62	9.74	28.36	26
$t\bar{t}$	9.51	7.91	17.42	1.61	5.01	4.41	9.42	54
single top	7.33	6.94	14.27	6.01	2.66	2.62	5.28	45
$Wb\bar{b}$	7.95	7.32	15.27	2.25	2.93	2.84	5.76	37
$Wc\bar{c}$	9.78	8.99	18.77	2.68	3.50	3.39	6.88	37
Wc	53.45	45.07	98.53	0.95	15.76	14.89	30.65	31
WW	17.07	15.40	32.47	10.6	7.31	6.69	14.00	43
MC total	1051	913	1964	N/A	304	280	584	30
Run I	1135	990	2125	N/A	323	308	631	30

Chapter 5

Search for W boson pair production

5.1 Heavy flavor tagging

The average p_T for c hadrons from W boson decay is large compared with the scale set by the c-quark mass. This, combined with the long c-quark lifetime, results in a long average decay length for c hadrons in W pair production.

The decay distance in the plane transverse to the beam direction is defined to be Lxy. A simplified illustration of an event containing a c hadron with large p_T is shown in Fig. 5.1. Tracks from the c-hadron decay are measurably displaced from the $p\bar{p}$ interaction point, called the primary vertex. The ability to identify such displaced tracks depends on the resolution for determining both the trajectory of each track and the position of the primary vertex from which most tracks emanate. At the CDF interaction region, primary vertices have a Gaussian distribution along the beam direction with $\sigma \sim 30$ cm and transverse to the beam axis with a $\sigma \ \sim 36$ μm.

The detector axis and beam axis are not exactly parallel and coaxial. The detector axis and the beam axis have a relative slope of ~ 4.5 μm/cm in the horizontal plane and ~ -3 μm/cm in the vertical plane. Through the course of the 9 months of data taking, these slopes were stable at the level of 1 μm/cm. The displacement of the detector axis and the beam axis (at the nominal interaction position $z = 0$) varied between 200 and 1200 μm in the horizontal plane and 400 and -1000 μm in the vertical plane. The slope and displacement drifted due to changing Tevatron conditions, but were measured on a run-by-run basis to accuracies of ~ 0.4 μm/cm for the slope and ~ 10 μm for the displacement.

The primary vertex is found for each event by a weighted fit of the SVX tracks and the VTX z event vertex position, with appropriate corrections for detector offset and slope. An iterative search removes tracks from the fit which have large impact

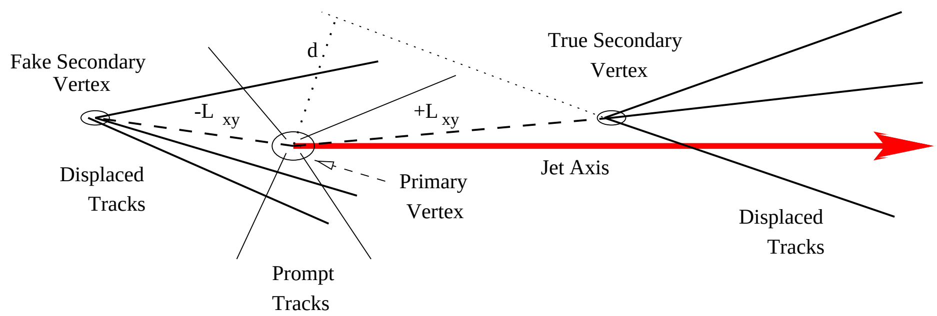

Figure 5.1: Simplified view of an event containing a secondary vertex shown in the transverse ($r-\phi$) plane. The solid lines represent charged-particle tracks reconstructed in the SVX. The primary vertex is the point in the $r-\phi$ plane where the $p\bar{p}$ interaction occurs. The secondary vertex is the point of decay for a long-lived particle originating at the primary vertex. The impact parameter, d, is shown for representative tracks. Also shown is L_{xy}, the two-dimensional decay distance to the secondary vertex, measured in the $r-\phi$ plane.

parameters. The impact parameter, d, is the distance of closest approach of a track to the primary vertex in the $r-\phi$ plane (Fig 5.1). The uncertainty in the fitted primary-vertex coordinates transverse to the beam direction ranges from 6 to 36 μm depending on the number of tracks and the event topology.

Because of the high-luminosity conditions of the 1992-93 run, approximately 40% of events in the W sample contain multiple primary interactions separated along the beam axis. In these events, the event vertex is chosen to be the one with the greatest total transverse momentum of associated tracks. All tracks used in the vertex fit and subsequent analysis are required to extrapolate to within 5 cm of this vertex along the beam direction. The resolution on the extrapolation to the z position for CTC tracks above 2 GeV/c is approximately 6 mm. The primary high-p_T electron or muon is associated with the chosen vertex in 99.9% of the events.

Displaced tracks identified with the SVX are used as input to two c-tagging algorithms. All two algorithms require the size of the impact parameter, d, to be large compared to its estimated uncertainty. The sign of the impact parameter is given by the angle between the jet axis and the track's point of closest approach to the primary vertex. The sign of impact parameter is positive(negative) when the angle is acute(obtuse). Tracks from heavy-flavor decay will populate both the positive and negative tails of the impact parameter distribution. The uncertainty on d, σ_d, is computed for each track with the measured momentum and multiple scattering based on the traversed material. It ranges from 50 μm for 1 GeV/c charged tracks to 15 μm for 10 GeV/c tracks.

The c tagging algorithms are applied to sets of SVX tracks associated with jets that have calorimeter $E_T \geq 10$ GeV and $|\eta| < 2.0$. An SVX track is associated with a jet if the opening angle(ΔR) between the track direction and the jet direction (given by the calorimeter) is less than 0.7. In order to remove tracks consistent with photon conversions and K_s or Λ decays originating from the primary vertex, we impose an impact parameter requirement ($|d| < 0.15$ cm). In addition, track pairs consistent with the K_s or Λ mass are removed.

CDF has the two c tagging algorithms referred as the "SECVTX" algorithm [32] and the "jet probability" algorithm(JPBTAG) [31]. We separate the W + 2jets sample into two samples applying SECVTX for this heavy flavor separation. One is $W \rightarrow u\bar{d}$ and the other is $W \rightarrow c\bar{s}$ sample.

In appendix B, we consider a JPBTAG-based analysis to do a similar analysis. We found however, that the SECVTX-based analysis provides better *expected* upper limits.

5.1.1 Identification of $W \rightarrow u\bar{d}$ and $W \rightarrow c\bar{s}$ using charm-tagging with SECVTX

The SECVTX algorithm requires a jet to contain at least two good SVX tracks. A good SVX track satisfies one of the following definitions:

- Loose definition of a good SVX track
  - $p_T > 0.5$ GeV/c in jet cone 0.7
  - Impact parameter significance $d_0/\sigma_{d0} > 2.5$
  - ≥ 1 good cluster for 3 and 4 hit tracks.
  - 2 hit tracks accepted if no bad clusters and $p_T > 1.5$ GeV/c
- Tight definition of a good SVX track
  - $p_T > 2.0$ GeV/c in jet cone 0.7
  - $d_0/\sigma_{d0} > 3.0$
  - ≥ 1 good cluster for 4 hit tracks.
  - ≥ 2 good cluster for 3 hit tracks.

The SECVTX-tagged jet must satisfy one of the following conditions:

- Three or more tracks in the jet satisfy the loose definition and at least one track has p_T above 2 GeV/c.
- Two or more tracks in the jet satisfy the tight definition, at least one track has p_T above 2 GeV/c and the secondary vertex made from these tracks have $\chi^2 \leq 50$.

Using these tracks, L_{xy} and its error $\sigma_{L_{xy}}$ (typically, 130 μm) are calculated using a 3-dimensional common vertex constrained fit. The sign of L_{xy} is given by the sign of the inner product of the vector from the primary vertex to the secondary vertex and the vector sum of the tagged-track momenta. Jets containing many mismeasured tracks, and no true secondary vertices, have vertices which are equally likely to have L_{xy} either positive or negative. This has been checked by combining tracks from different jets to form a vertex. This avoids contamination from real long lived objects found within a single jet. In order to mimic the small opening angle of tracks in the same jet, events with jets nearly back-to-back were selected. Track pairs with an opening angle near 180^o will form vertices with similar properties to those formed by tracks with opening angles near 0^o. The larger of the two jets is taken as defining the positive L_{xy} direction. The resultant L_{xy} distribution is observed to be symmetric about $L_{xy} = 0$. In contrast, jets containing long lived particles have vertices with L_{xy} predominantly positive. For the purposes of identifying c jets, only jets with $\frac{L_{xy}}{\sigma_{L_{xy}}} \geq 3.0$ are considered 'tags'. As explained below, the bulk of the SVX c tagging results reported use this algorithm.

We define the following additional cut to remove K_s and Λ candidates, b jet and primary jet(P jet).

- Remove displaced K_s and Λ candidates using track mass which is reconstructed with a good SVX track's four momentum.
- $JP^+ > 0.001$, where JP^+ is the jet-probability using tracks with positive impact parameter. This cut helps remove b jets.
- $c\tau > 60$ μm. This cut helps remove "primary" jets, i.e. jets originating at the primary event vertex.

Figure 5.2 shows the SECVTX tagging efficiency for each b, c and primary jet. The charm jet tagging efficiency is about 8–10%. The primary jet tagging efficiency is about 0.1–0.2%, therefore the signal significance should be improved by this cut.

We now introduce two non-overlapping subsamples of the search sample: the $W+cs$ subsample, which contains all events with one charm tag and one null tag; and the $W+ud$ subsample, which contains all events with two null tags. Table 5.1 shows the expected numbers of signal and background events in these two subsamples.

5.2 Charged track multiplicity

The mean value of the charged multiplicity in gluon jets is expected to be higher than that of quark jets [33], because a gluon decay into quark pair at the first stage of fragmentation.

Table 5.1: Expected numbers of signal and background events in the $W + cs$ and $W + ud$ subsamples; ε = (Number of events in subsample)/(Number of events in search sample).

	$W + cs$ sample				$W + ud$ sample			
	e	μ	Total	$\varepsilon(\%)$	e	μ	Total	$\varepsilon(\%)$
$W + 2jets$	0.76	0.79	1.54	0.32	245.32	232.46	477.78	98.8
$Non - W$	0.00	0.27	0.27	0.95	13.34	7.97	21.30	75.1
$t\bar{t}$	1.03	0.91	1.94	20.6	2.67	2.33	5.00	53.1
$single\ top$	0.51	0.54	1.04	19.7	1.84	1.79	3.63	68.8
$Wb\bar{b}$	0.52	0.50	1.02	17.7	1.48	1.44	2.92	50.7
$Wc\bar{c}$	0.36	0.37	0.74	10.8	2.97	2.86	5.83	84.7
Wc	1.32	1.26	2.58	8.42	14.00	13.19	27.19	88.7
WW	0.21	0.20	0.41	2.93	6.99	6.40	13.39	95.6
MC total	4.71	4.84	9.55	1.64	288.62	268.42	557.04	95.4
Run I	4	6	10	1.58	300	287	587	93.0

For measuring the charged track multiplicity and the jet charge, we first define a jet's "track axis" by summing up all the momentum vectors of tracks that are within a cone of radius $\Delta R = 0.4$ around the original jet axis and that have a total momentum of at least 0.4 GeV/c (Figure 5.3).

We then calculate the charged track multiplicity of a jet ($\mathcal{CM}_j$) by counting all charged tracks which have momentum along the jet track axis greater than 0.5 GeV/c and that are within a given distance ΔR from that axis, where ΔR can be 0.4, 0.7 and 1.0(see Fig. 5.4). The larger ΔR is, the better the separation between a gluon jet and a quark jet is. Therefore we chose $\Delta R = 0.7$ in this analysis.

As shown in Figure 5.5, the charged track multiplicity strongly depends on jet E_T. Therefore, our definition of the global likelihood variable in section 5.7 will have to take into account the correlations between $\mathcal{CM}_j$ and E_{Tj}. Figure 5.5 also shows that different hadronization algorithms such as HERPRT and JETSET are in reasonable agreement with each other and indicate a clear separation between the mean charged track multiplicities in gluon and quark jets.

Figure 5.6 shows some 1-dimensional charged track multiplicity distributions for Run 1 data and simulations. The likelihood analysis of section 5.7 requires 2-dimensional distributions of charged track multiplicity versus jet E_T, which are shown in Figures 5.7 to 5.10.

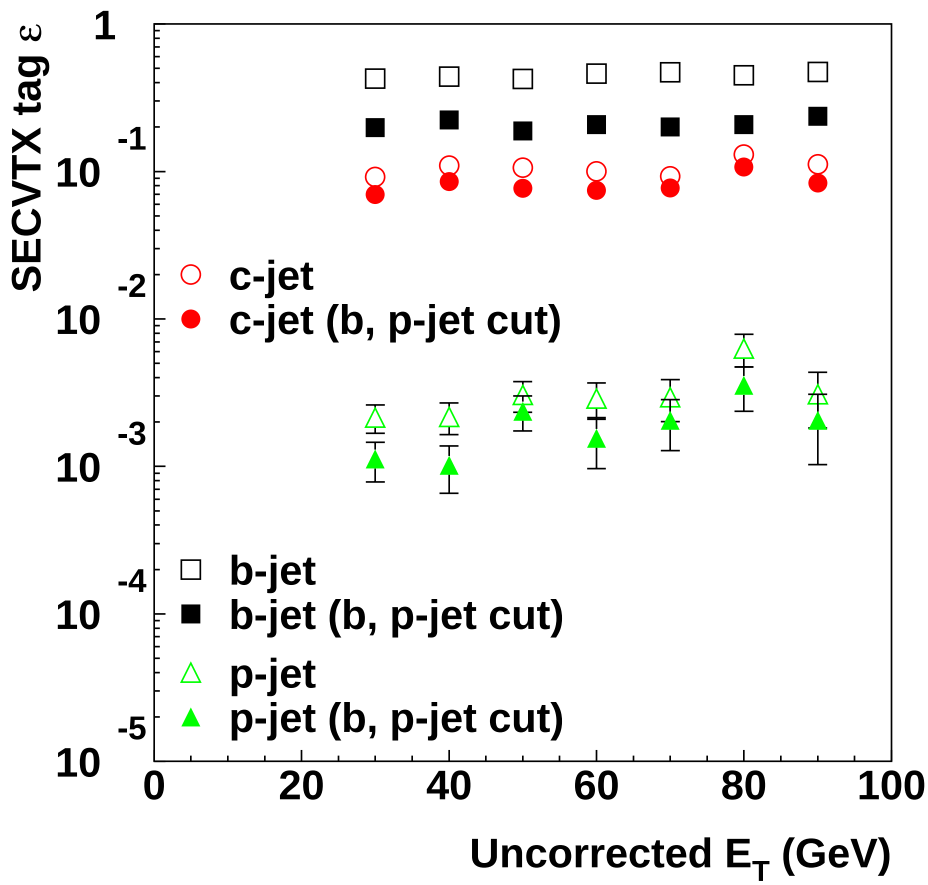

Figure 5.2: SECVTX tagging efficiency for primary, charm and bottom jets in PYTHIA. Hollow symbols show the tagging efficiency for the default SECVTX algorithm used by the top group [25], whereas filled-in symbols include the additional cuts $JP+ > 0.001$ and $c\tau > 60\mu$m used to reject b-jets and primary jets, respectively.

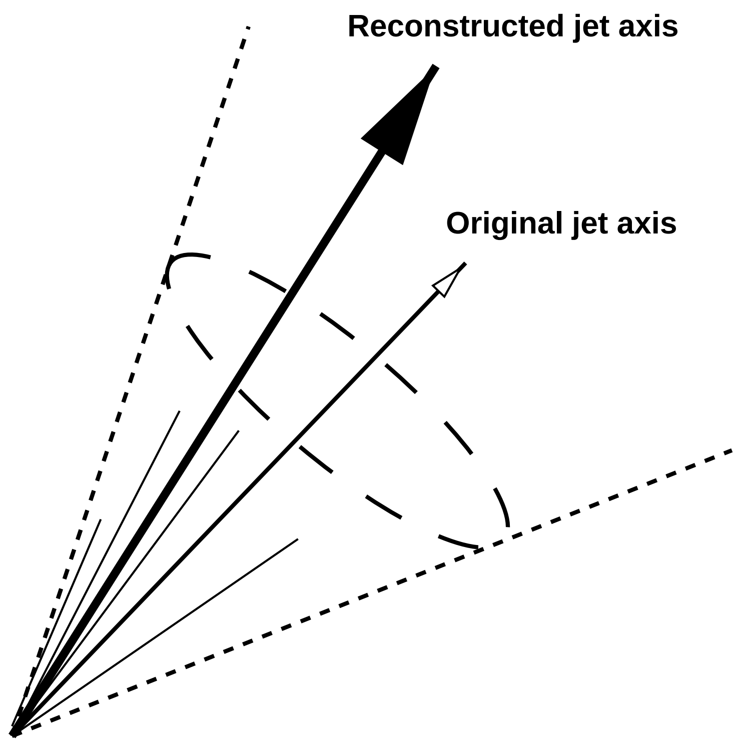

Figure 5.3: New jet axis reconstructed from the momentum of tracks which are in $\Delta R = 0.4$ around original jet axis, and the momentum is over 0.4 GeV/c.

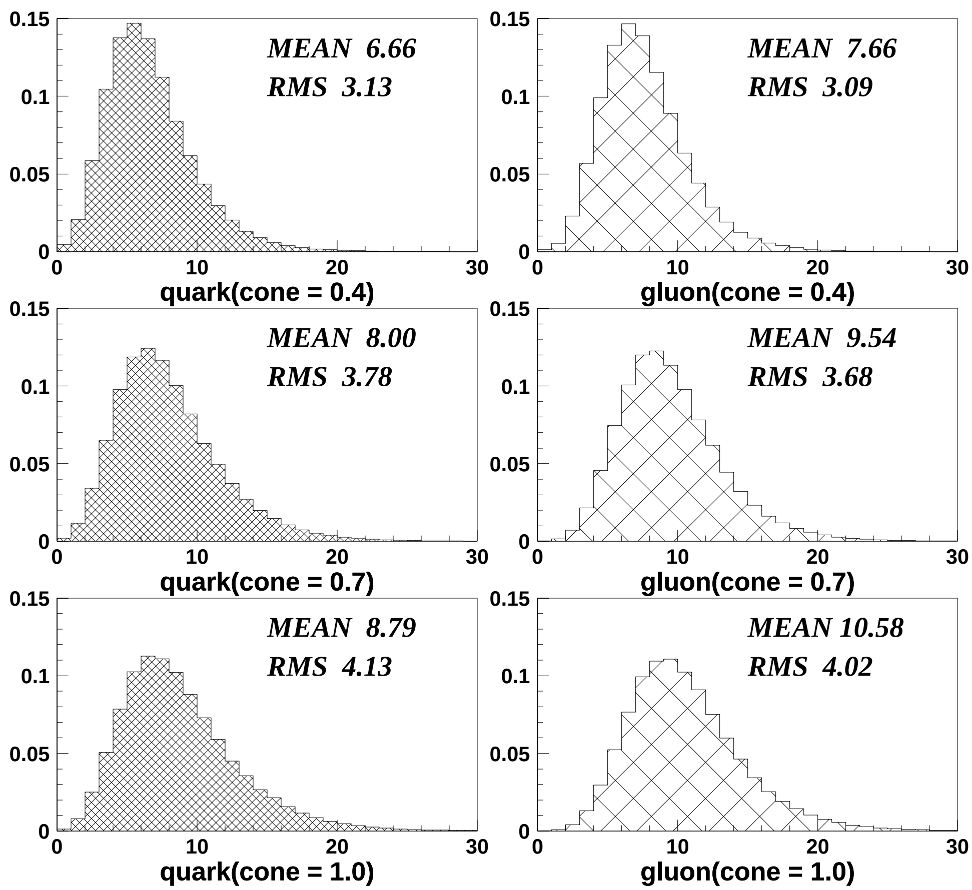

Figure 5.4: Quark and gluon jet charged track multiplicity for jet cone sizes of 0.4, 0.7 and 1.0. Upper section is $\Delta R = 0.4$, middle section is $\Delta R = 0.7$ and lower section is $\Delta R = 1.0$ for the W + 2jets sample.(VECBOS)

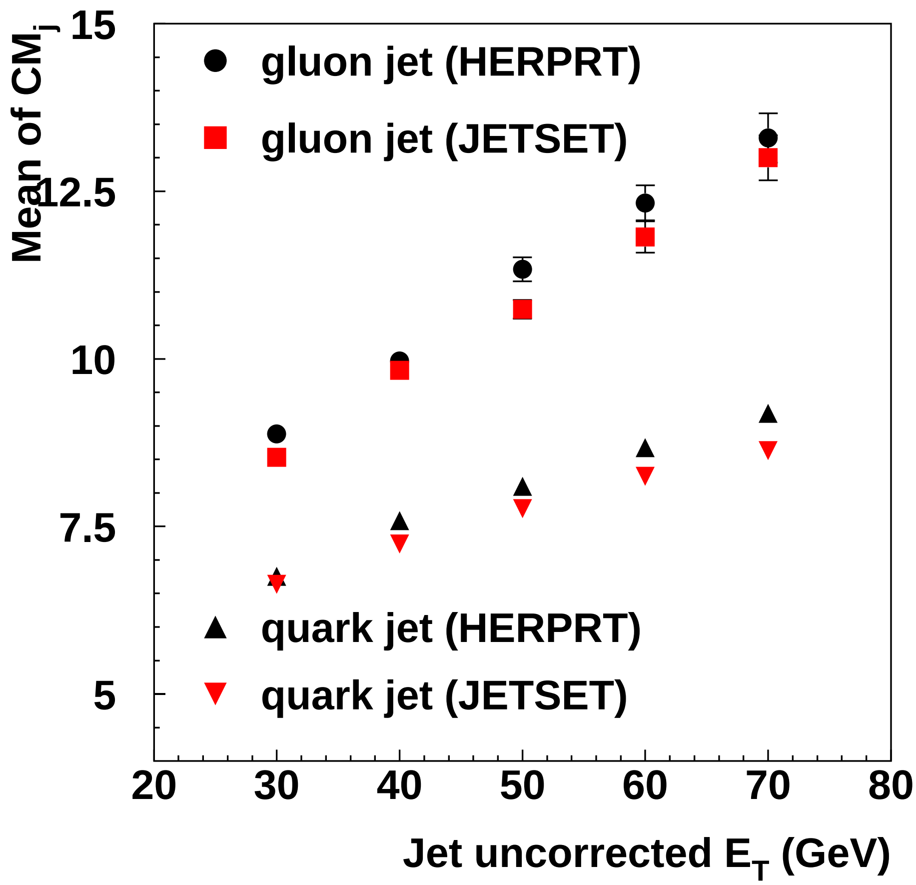

Figure 5.5: Mean charged track multiplicity vs. uncorrected E_T for quark and gluon jets with $\Delta R = 0.7$. The HERPRT and JETSET hadronization algorithms appear to give consistent results.

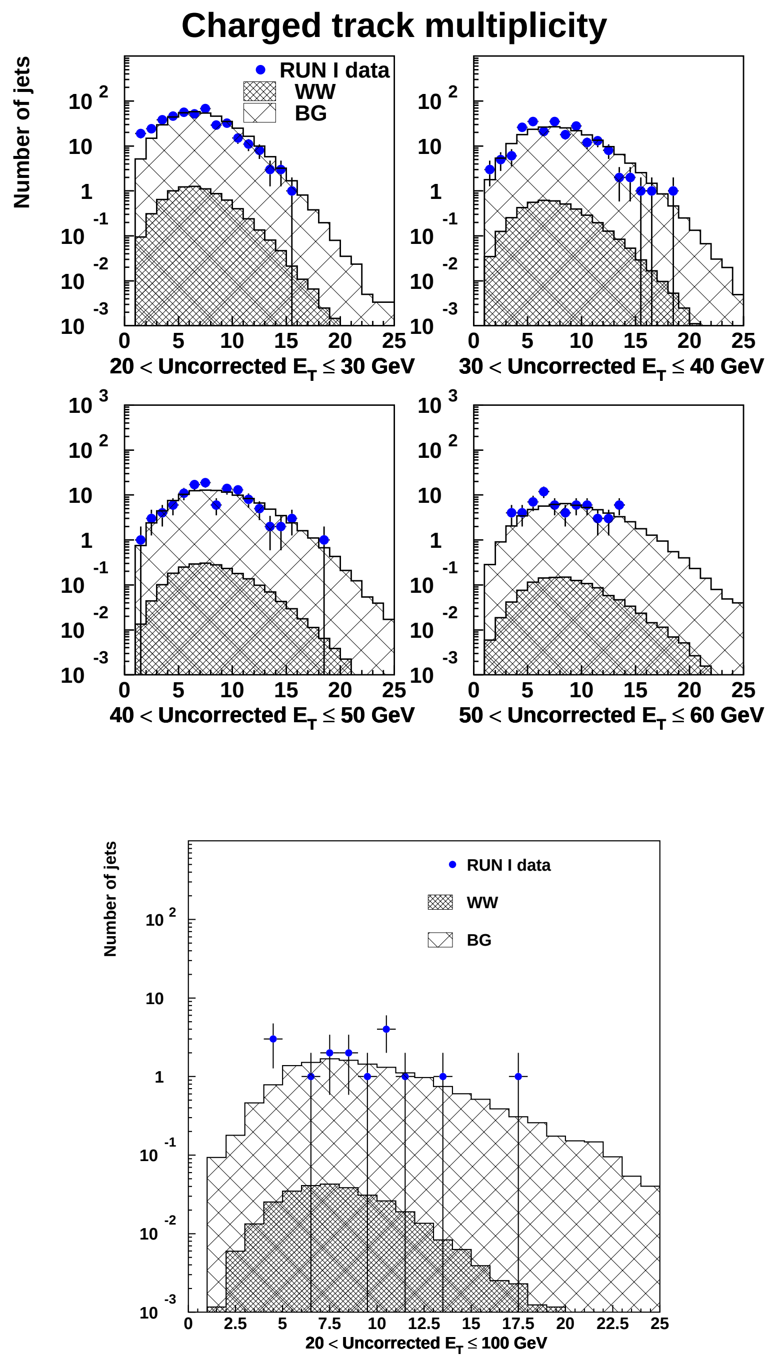

Figure 5.6: Charged track multiplicity in jets with $\Delta R = 0.7$, for various uncorrected E_T ranges. Top: $W + ud$ sample (note how the slope of the right-hand tails of the distributions changes with increasing jet E_T, leading to the increase in mean charged track multiplicity observed in Figure 5.5); bottom: $W + cs$ sample.

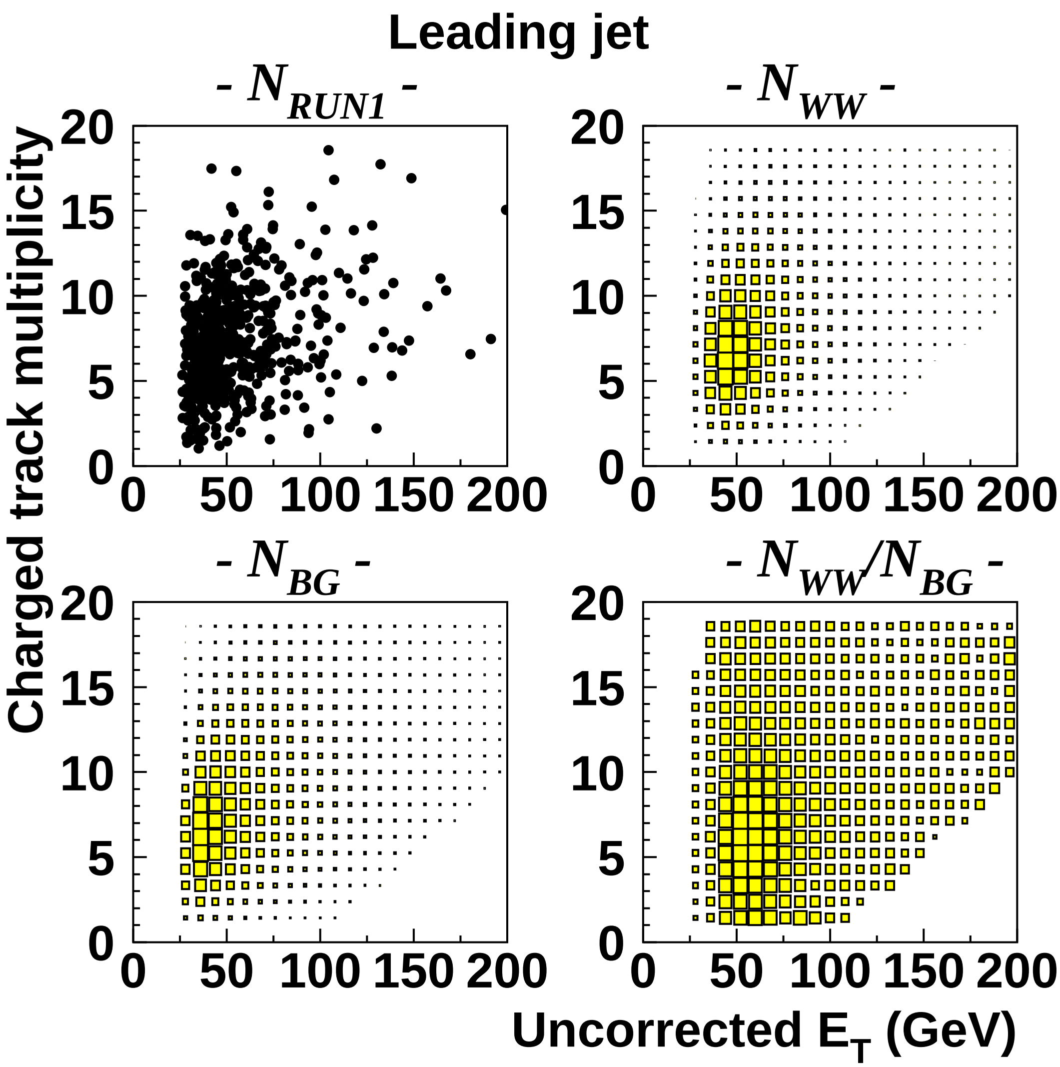

Figure 5.7: Charged track multiplicity versus uncorrected E_T of leading jet in $W+ud$ sample. Top left: Run 1 data; top right: W^+W^- signal; bottom left: background; bottom right: ratio between W^+W^- and background distributions after separately normalizing them to 1.

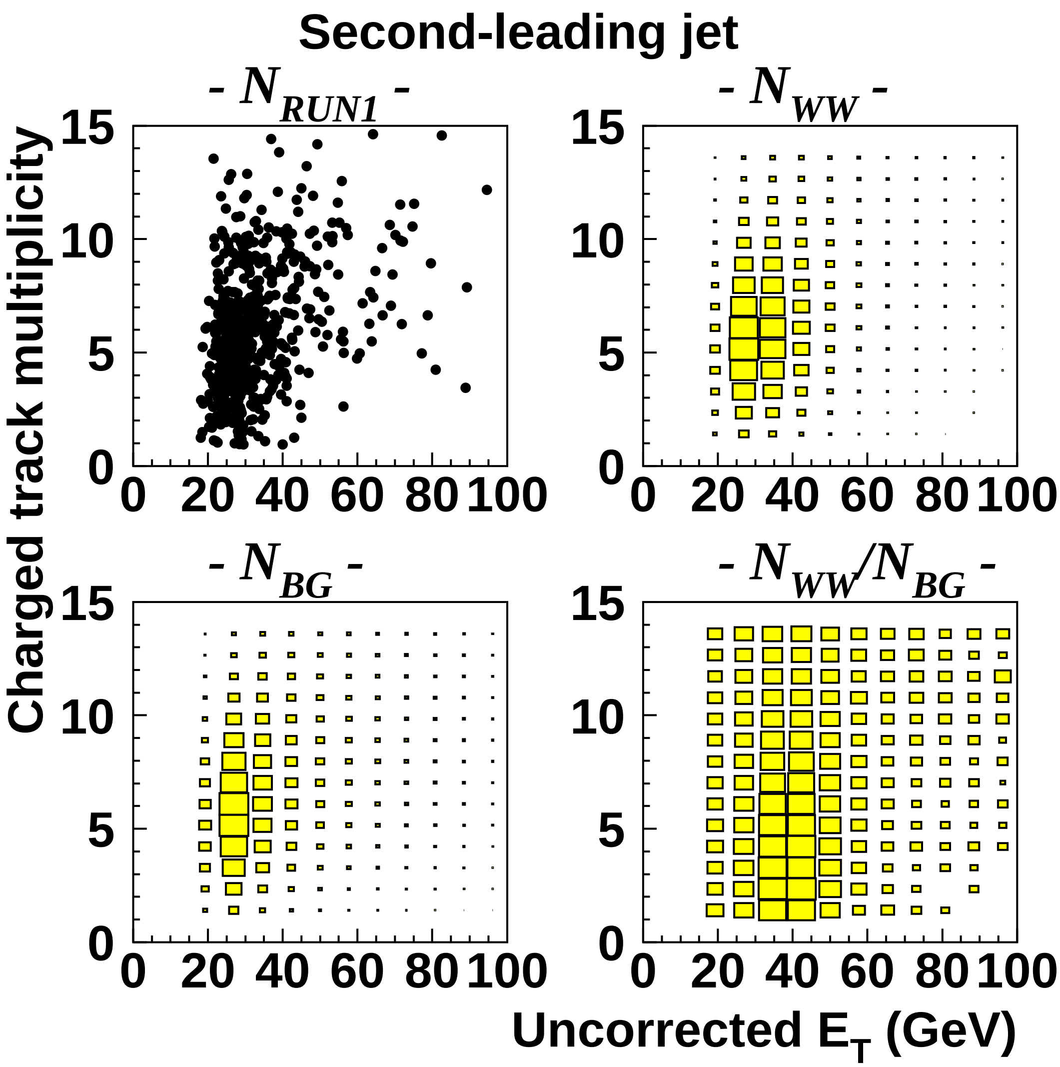

Figure 5.8: Charged track multiplicity versus uncorrected E_T of next-to-leading jet in $W + ud$ sample. Top left: Run 1 data; top right: W^+W^- signal; bottom left: background; bottom right: ratio between W^+W^- and background distributions after separately normalizing them to 1.

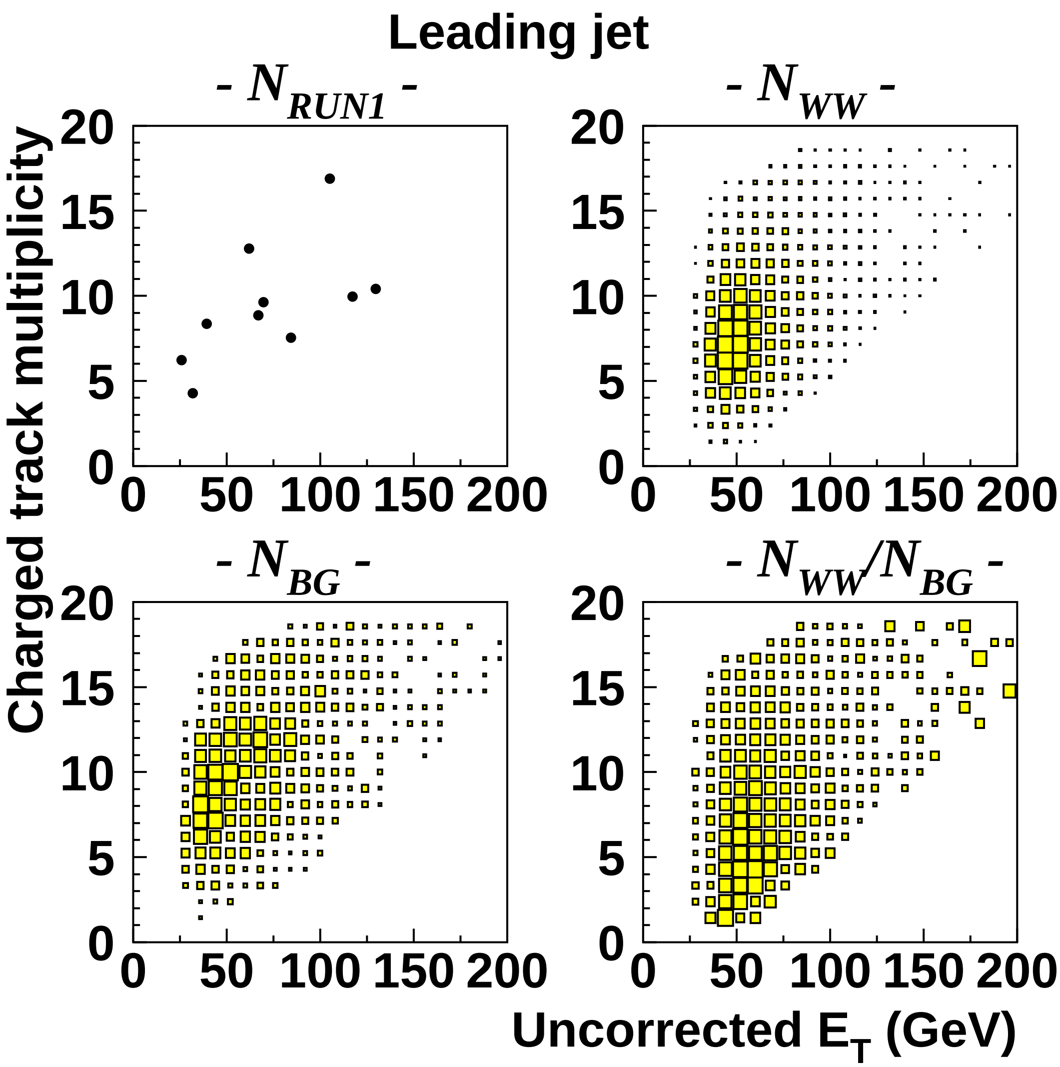

Figure 5.9: Charged track multiplicity versus uncorrected E_T of leading jet in $W+cs$ sample. Top left: Run 1 data; top right: W^+W^- signal; bottom left: background; bottom right: ratio between W^+W^- and background distributions after separately normalizing them to 1.

5.3 Jet charge

As quarks and gluons cannot be observed directly, their charges have to be inferred from the corresponding hadoronic final states. Previous CDF analyses have estimated parton charge by measuring so-called jet charges [4]. The jet charge is a momentum-weighted sum of track charges, defined as follows:

$$Q_{jet} \equiv \frac{\Sigma_i \, q_i \cdot (\vec{p}_i \cdot \hat{a})}{\Sigma_i \, \vec{p}_i \cdot \hat{a}} \tag{5.1}$$

where q_i and $\vec{p}_i$ are the charge and momentum of the i-th track in the jet and $\hat{a}$ is a unit-vector along the jet's track axis. We demand a jet should have at least two charged tracks. The jet charge(Q_{jet}) depends on $\vec{p}_i$ and a jet cone size(ΔR). We optimized the Q_{jet} cut threshold for fixed $\vec{p}_i$ and ΔR. The Q_{jet} distributions for various flavors are obtained from VECBOS W + 2jets sample and PYTHIA W^+W^- sample as shown in Figs. 5.11- 5.14 and listed in Table 5.2. These Q_{jet} distributions depend on their original parton charge, except the Q_{jet} coming from a charm-quark. It is quite smaller than that from an up-quark because the $D^{*\pm}$ mesons decay to $D^0(energetic) + \pi^{\pm}$. We use this Q_{jet} variable to reduce the background of gluon jets such as QCD W + jet background.

Table 5.2: Average jet charge $\langle Q_{jet} \rangle$ in PYTHIA and VECBOS, as a function of parton flavor. The jet charge is calculated according to equation (5.1) using all tracks within a radius ΔR of the jet's track axis and with at least 0.5 GeV/c of momentum along this axis.

Flavor	Parton-level charge	Jet-level charge $\langle Q_{jet} \rangle$		
		PYTHIA		VECBOS
		$\Delta R = 0.4$	$\Delta R = 0.7$	
u	2/3	0.23	0.22	0.16
d	−1/3	−0.14	−0.13	−0.12
s	−1/3	−0.17	−0.16	−0.10
c	2/3	0.07	0.07	0.03
gluon	0	0.00	0.00	0.01

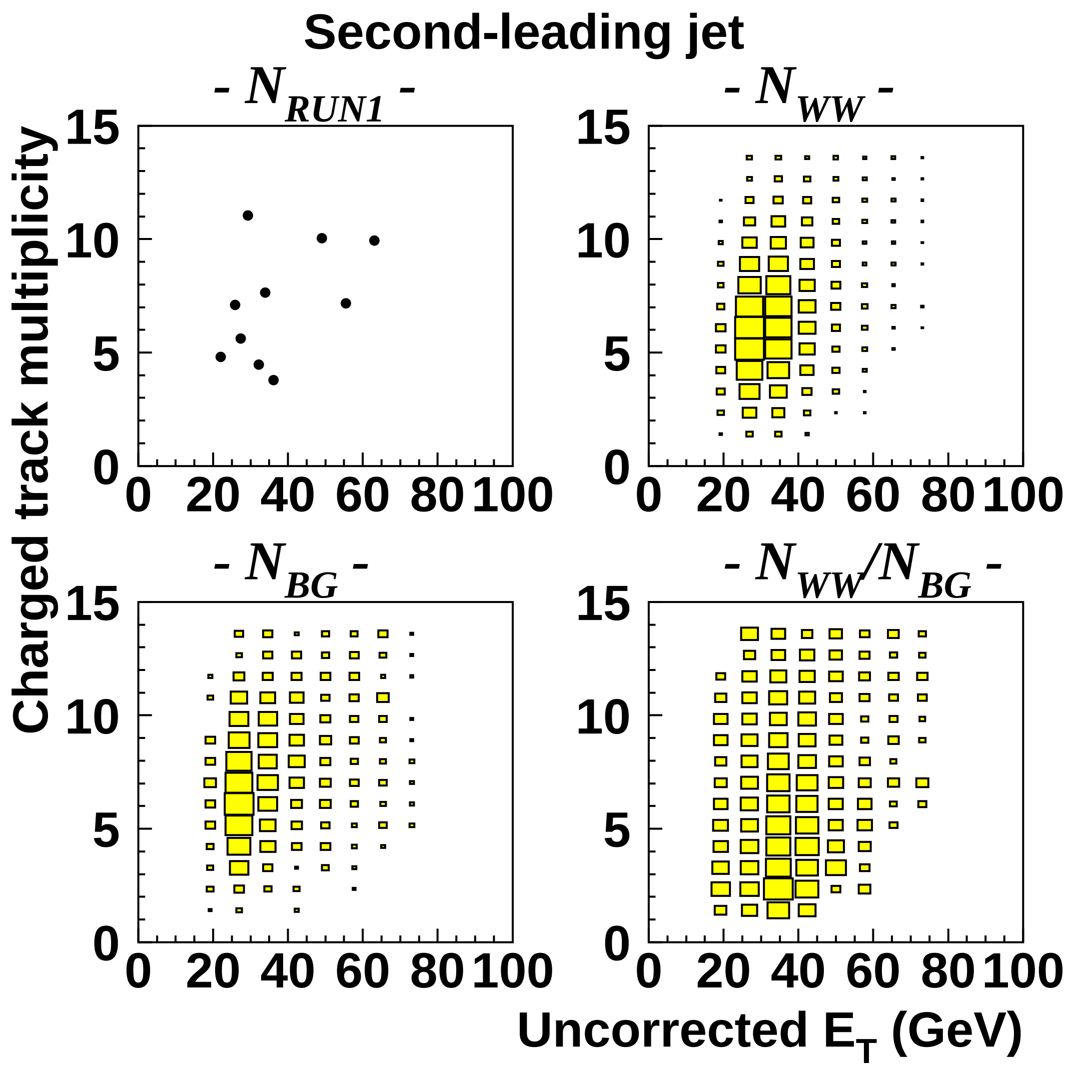

Figure 5.10: Charged track multiplicity versus uncorrected E_T of next-to-leading jet in $W + cs$ sample. Top left: Run 1 data; top right: W^+W^- signal; bottom left: background; bottom right: ratio between W^+W^- and background distributions after separately normalizing them to 1.

We define the total electric charge Q_{tot} by

$$Q_{tot} \equiv -Q_{lepton} \cdot (Q_{jet1} + Q_{jet2}) \tag{5.2}$$

where Q_{jet1} is the leading jet charge and Q_{jet2} is the second-leading jet charge. For signal events, Q_{lepton} and $(Q_{jet1}+Q_{jet2})$ equal the electric charge of the corresponding parent W boson at parton level, so that $\langle Q_{tot} \rangle = 1$ at parton level. However, as the absolute value of $\langle Q_{jet} \rangle$ is less than that of the corresponding quark charge q^f, the measured $\langle Q_{tot} \rangle$ is less than one. For background events, $\langle Q_{tot} \rangle$ is expected to be close to zero.

Figures 5.15 and 5.16 show the Q_{tot} distribution for signal and background.

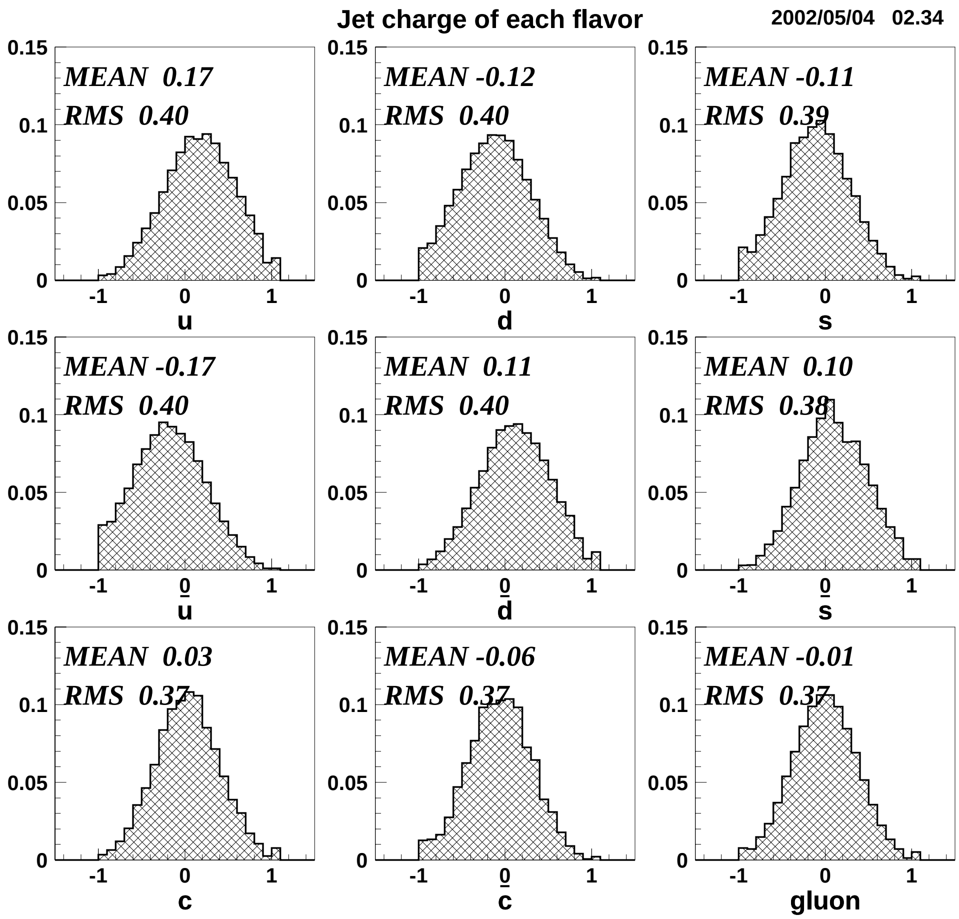

Figure 5.11: The jet charge Q_{jet} for different quark flavors as expected at the hadronic final state for VECBOS W + 2jets sample. $\Delta R = 0.4$ and $P_{axis,i} > 0.5$ (GeV/c).

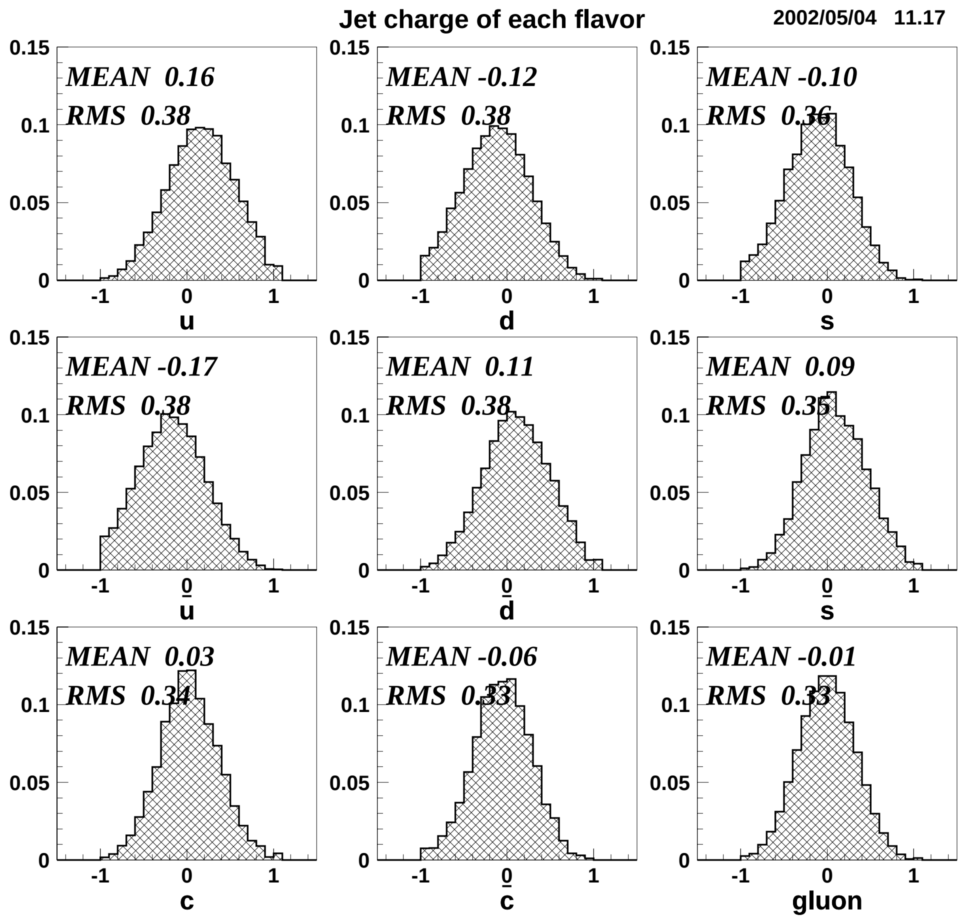

Figure 5.12: The jet charge Q_{jet} for different quark flavors as expected at the hadronic final state for VECBOS W + 2jets sample. $\Delta R = 0.7$ and $P_{axis,i} > 0.5$ (GeV/c)

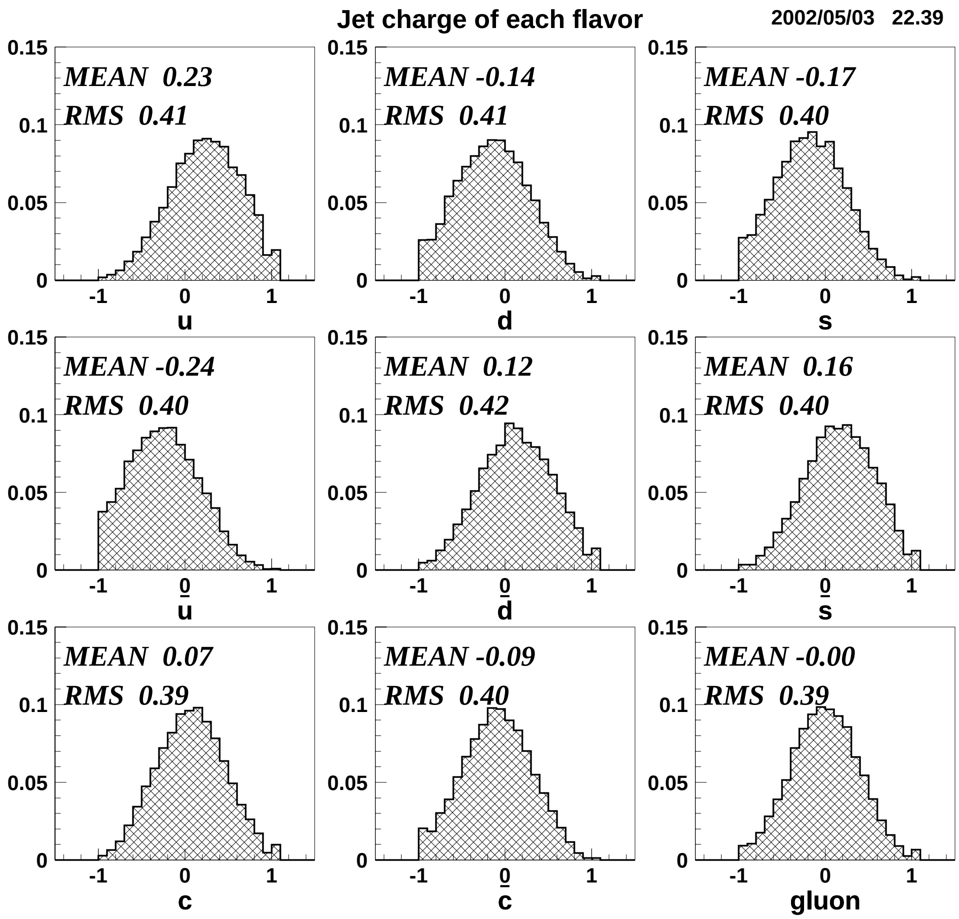

Figure 5.13: The jet charge Q_{jet} for different quark flavors as expected in the hadronic final state for PYTHIA W^+W^- sample. $\Delta R = 0.4$ and $P_{axis,i} > 0.5$ (GeV/c).

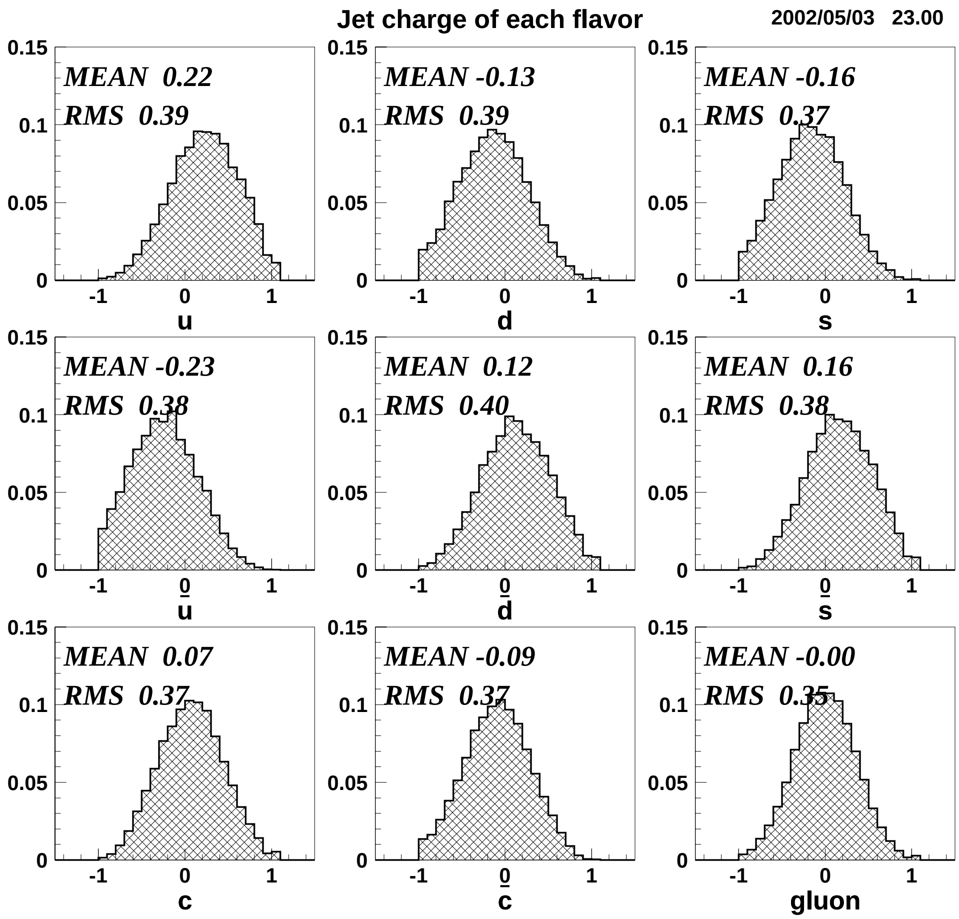

Figure 5.14: The jet charge Q_{jet} for different quark flavors as expected in the hadronic final state for PYTHIA W^+W^- sample. $\Delta R = 0.7$ and $P_{axis,i} > 0.5$ (GeV/c)

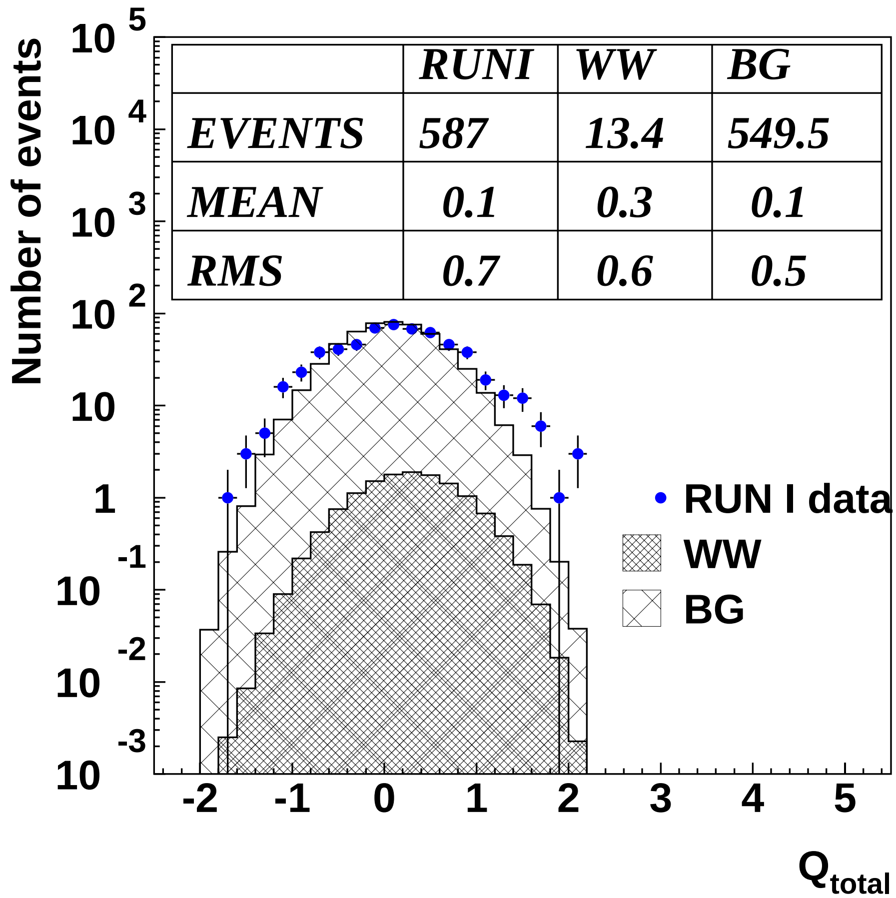

Figure 5.15: Distribution of the total charge Q_{tot} in the $W + ud$ sample. $\Delta R = 0.7, P_{axis,i} > 0.5$ (GeV/c)

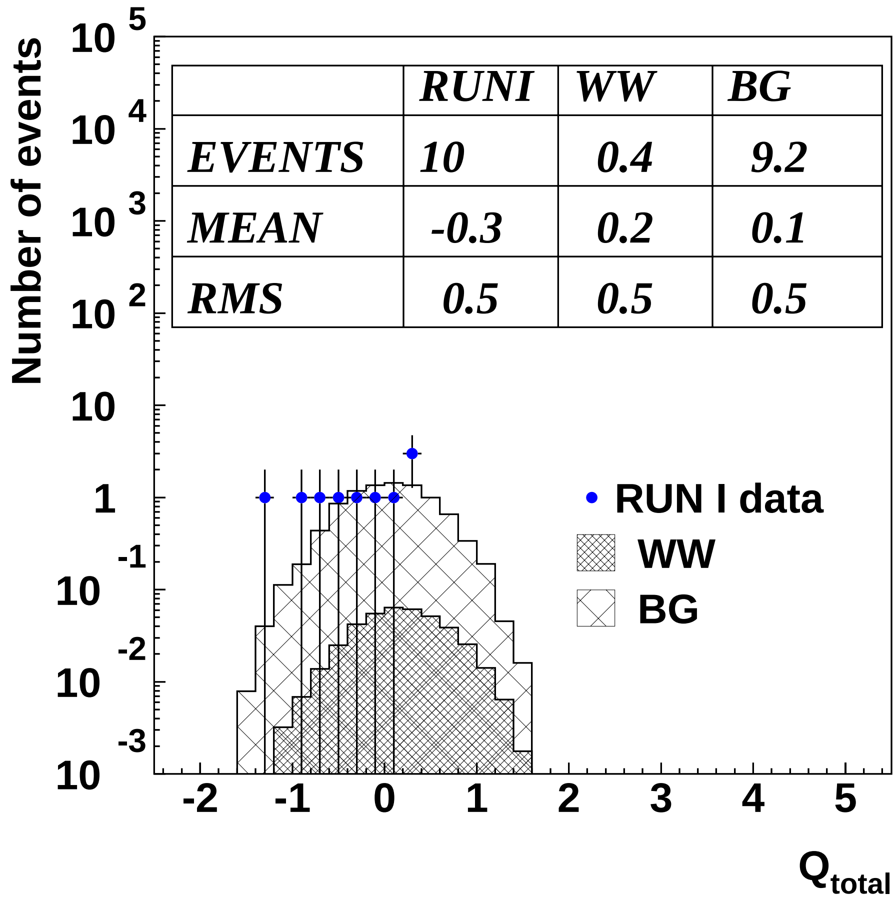

Figure 5.16: Distribution of the total charge Q_{tot} in the $W + cs$ sample. $\Delta R = 0.7$,$P_{axis,i} > 0.5$ (GeV/c)

5.4 Pseudo-rapidity asymmetry in W pair production

$W^{\pm}$ bosons are produced in the annihilation of $u(d)$ quark in proton and $\bar{u}(\bar{d})$ quark in antiproton(Fig. 1.1). The $W^{+}(W^{-})$ boson is coming from $u(\bar{u})$ quark and follow the direction of incoming proton(antiproton) because $W^{+}W^{-}$ production is dominated by a t-channel quark exchange process [34]. So the pseudo-rapidity η of $W^{+}W^{-}$ boson have asymmetry.

Figure 5.17 shows the η distributions of the $W^{\pm}$ bosons in PYTHIA $W^{+}W^{-}$ events. Figures 5.18 and 5.19 show asymmetry distributions for data and simulations in the

$W + ud$ and $W + cs$ samples respectively, where the asymmetry is represented by the parameter A_1:

$$A_1 \equiv -Q_{lepton} \times \eta_W, \tag{5.3}$$

Q_{lepton} being the lepton charge and η_W the pseudo-rapidity of the W boson on the dijet side.

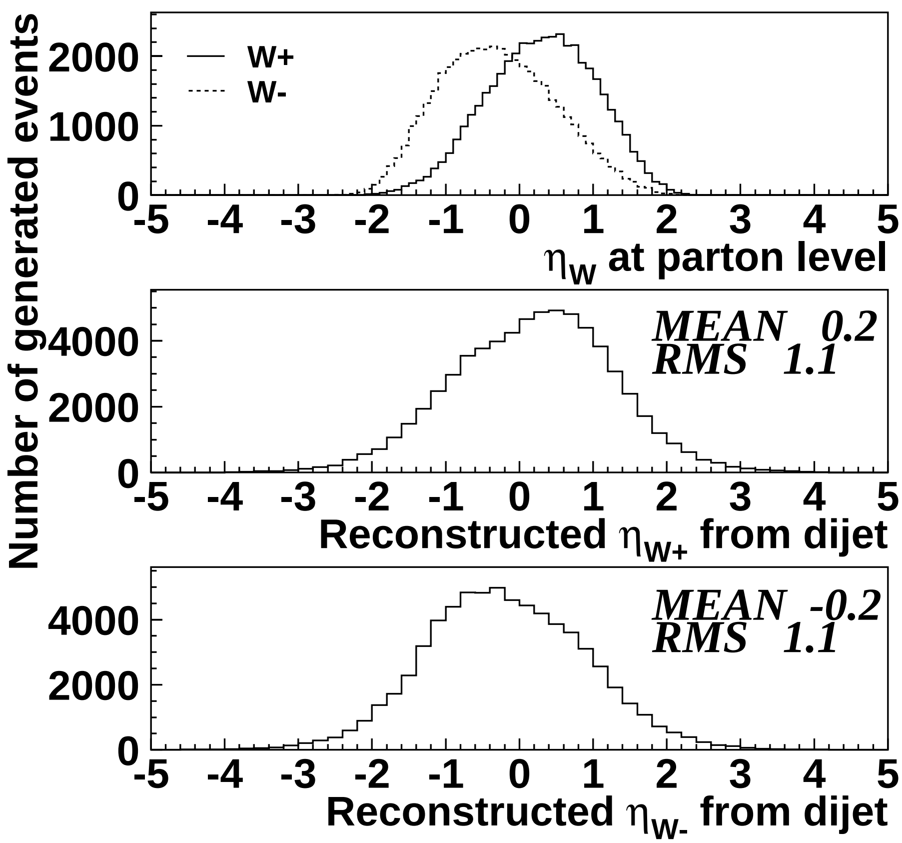

Figure 5.17: Distributions of W-boson η in PYTHIA W^+W^- sample. Top: generator-level distributions. Middle and bottom: reconstruction-level distributions, with η_W calculated from dijet system.

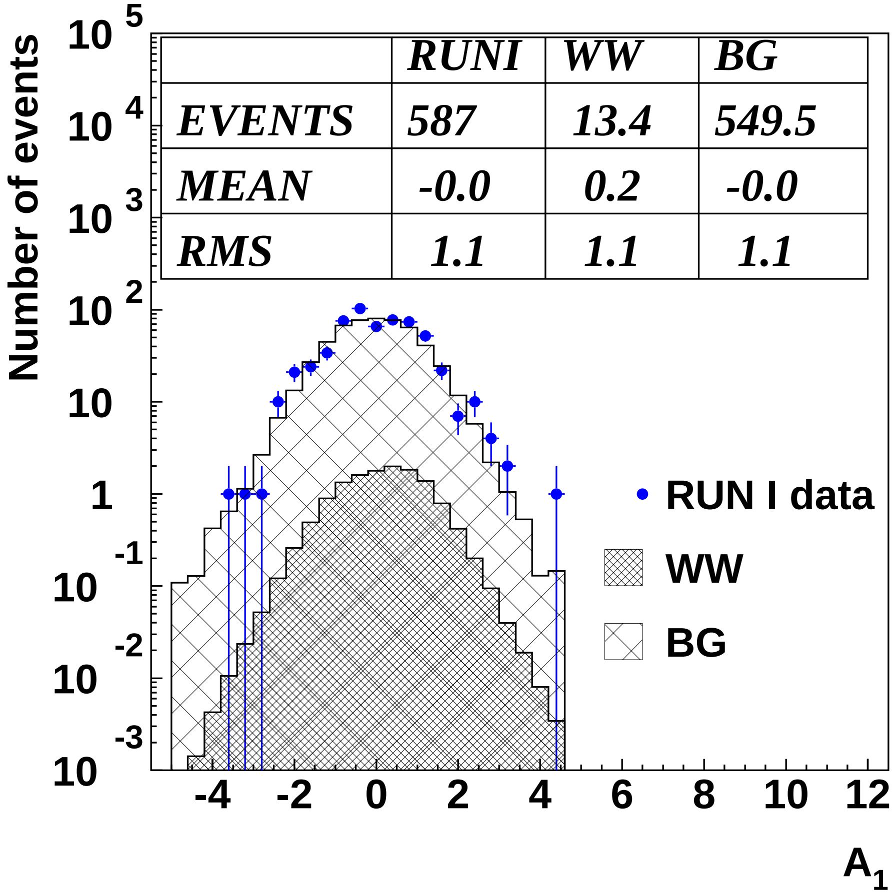

Figure 5.18: Pseudo-rapidity asymmetry of W^+ and W^- bosons in the $W + ud$ sample. The W-boson η is reconstructed from the dijet system ($A_1 \equiv -Q_{lepton} \cdot \eta_W$).

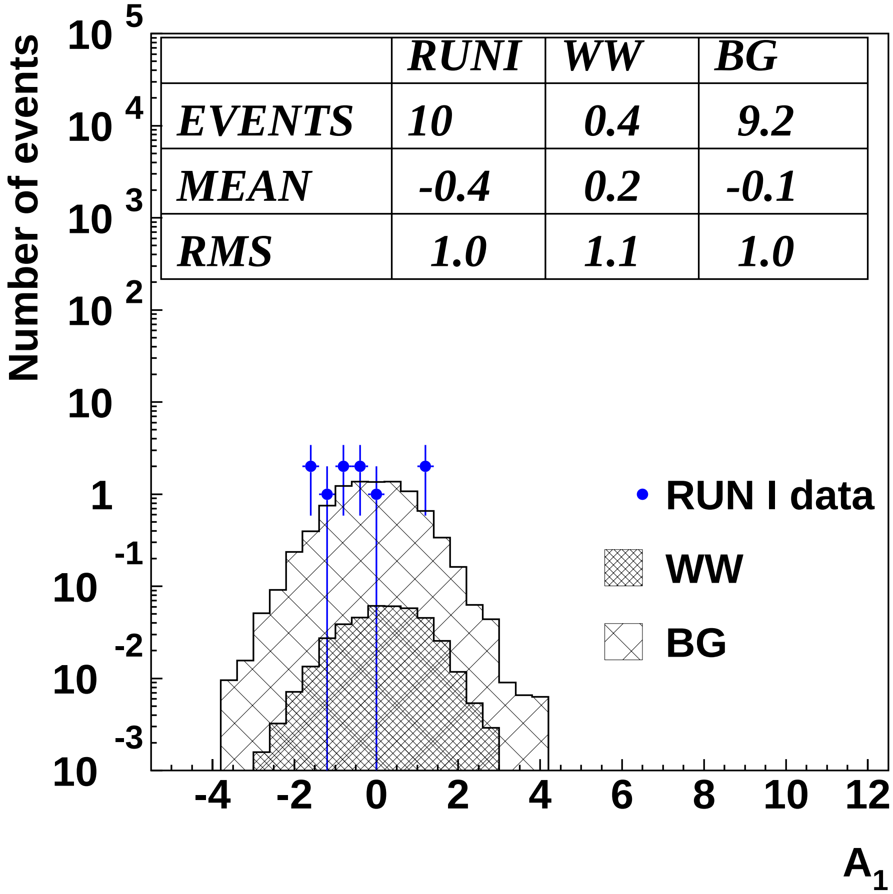

Figure 5.19: Pseudo-rapidity asymmetry of W^+ and W^- bosons in the $W + cs$ sample. The W-boson η is reconstructed from the dijet system ($A_1 \equiv -Q_{lepton} \cdot \eta_W$).

5.5 Azimuthal correlation between the $\ell\nu$ and dijet systems

The W-pair signal enjoys spin correlations that originate from initial-state parton spins. Furthermore, the charged lepton and neutrino decay products on one side, and the up- and down-type quark decay products on the other side, have directivities that depend on the parent W boson spin. As a result, in W-pair production the up(down)-type quark tends to escape in the direction opposite that of the $\nu(\ell)$ in the $r - \phi$ plane.

We can investigate these correlations in the $W + cs$ sample by plotting the azimuthal opening angle between lepton and null tag versus the azimuthal openingangle between lepton and charm tag (Figure 5.20). The same plot can be made with the missing E_T replacing the lepton (Figure 5.21). For obvious reasons, azimuthal correlations cannot be studied in the $W + ud$ sample.

5.6 Dijet mass

For signal events the dijet mass distribution is expected to cluster around the W boson mass ($\sim$ 80 GeV/c^2). We reconstruct the dijet mass from the jet four-momenta after correcting them with JTC96S and AAJSCO. Figure 5.22 shows the dijet mass distributions in the $W + ud$ and $W + cs$ samples.

5.7 Global likelihood

One way to assess the effectiveness of a generic parameter Z in separating signal from background is to measure its separation power $SP(Z)$:

$$SP(Z) \equiv \frac{\langle Z\rangle_S - \langle Z\rangle_B}{\sqrt{\mathrm{Var}_S(Z) + \mathrm{Var}_B(Z)}}, \tag{5.4}$$

where $\langle Z\rangle_S$, $\langle Z\rangle_B$ are mean values of Z over the signal and background samples respectively, and $\mathrm{Var}_S(Z)$, $\mathrm{Var}_B(Z)$ are the corresponding variances. Table 5.3 shows the separation powers of the three 1-dimensional parameters in our analysis.

Table 5.3: Separation powers of the combined W charge, the dijet invariant mass,and the pseudo-rapidity asymmetry in the $W + ud$ and $W + cs$ samples.

Sample	Q_{tot}	M_{jj}	A_1
$W + ud$	0.26	0.11	0.14
$W + cs$	0.18	0.18	0.18

These values justify inclusion of the corresponding parameters in a global likelihood variable to be defined below. It should be noted however, that separation power is not the only measure of discrimination between signal and background, and that likelihood variables are generally sensitive to differences in higher order moments than just the mean.

The parameters defined in the five previous sections (charged track multiplicity $\mathcal{CM}$ versus jet E_T, combined W charge Q_{total}, W boson pseudo-rapidity asymmetry

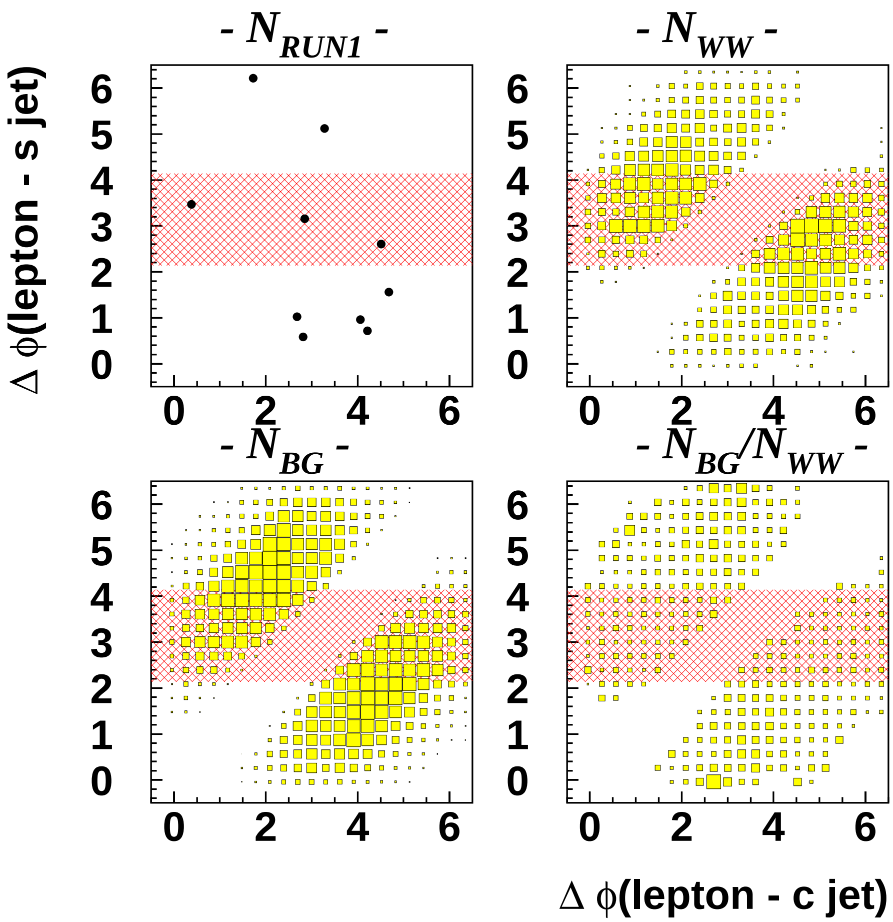

Figure 5.20: Azimuthal opening angle between lepton and null tag ("s jet"), versus azimuthal opening angle between lepton and charm tag ("c jet"). Upper left: Run 1 data; upper right: W^+W^- events; lower left: background events; lower right: ratio between W^+W^- and background distributions, after separately normalizing them to 1. W^+W^- events are concentrated in the hatched region.

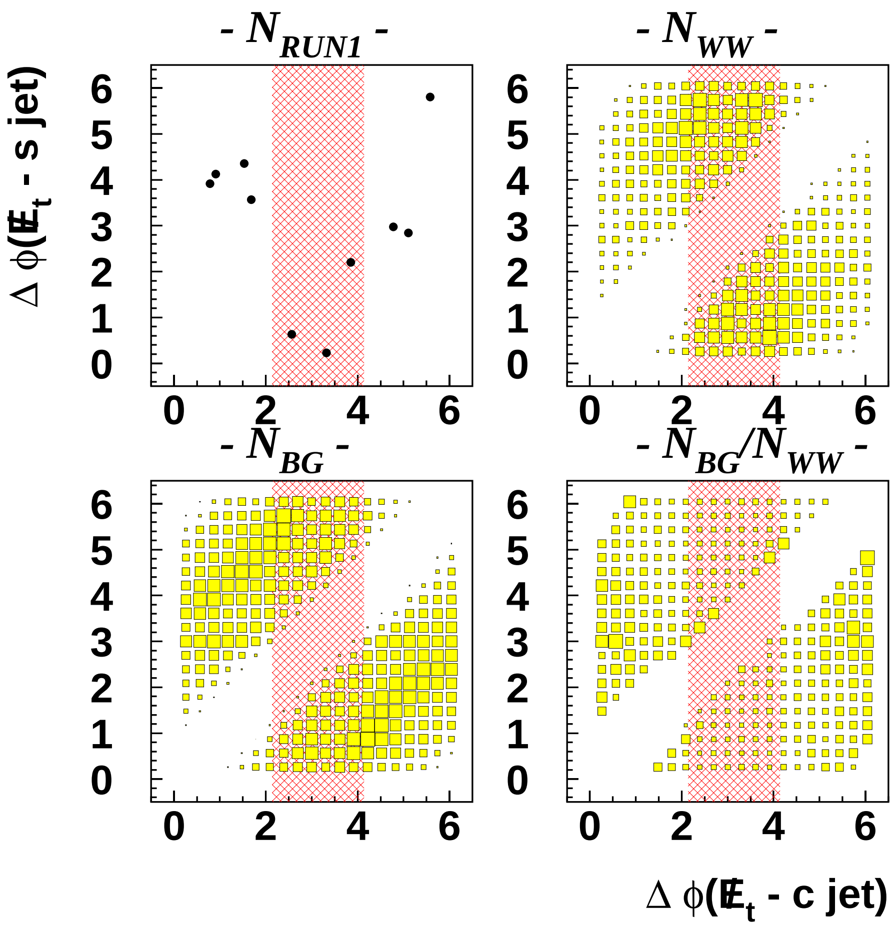

Figure 5.21: Azimuthal opening angle between missing E_T and null tag ("*s* jet"), versus azimuthal opening angle between missing E_T and charm tag ("*c* jet"). Upper left: Run 1 data; upper right: W^+W^- events; lower left: background events; lower right: ratio between W^+W^- and background distributions, after separately normalizing them to 1. W^+W^- events are concentrated in the hatched region.

A_1, ϕ correlations between $\ell(\nu)$ and dijet, and dijet mass, see Table 5.4) are combined into a global likelihood variable L for the $W + cs$ and $W + ud$ samples separately:

$$L = \sum_i \ln\left[\frac{P^i_{WW}(x_i)}{P^i_{BG}(x_i)}\right], \tag{5.5}$$

where i indexes the list of parameters, and $P^i_{WW}(x_i)$ and $P^i_{BG}(x_i)$ are the densities of parameter i for the W^+W^- signal and backgrounds, respectively, evaluated at the measured value x_i. We estimate these densities with highly populated histograms with narrow bins (no smoothing is performed).

Table 5.4: Components of the global likelihood function. We used seven components to analyze the cs sample, and five for the ud sample.

Likelihood Component	dimension	cs	ud
Charged track multiplicity vs. jet E_t for leading jet	2	✓	✓
Charged track multiplicity vs. jet E_t for 2^{nd}-leading jet	2	✓	✓
Q_{total}	1	✓	✓
η asymmetry of W boson	1	✓	✓
Dijet mass	1	✓	✓
$\Delta\phi(\ell, \text{charm tag})$ vs. $\Delta\phi(\ell, \text{null tag})$	2	✓	
$\Delta\phi(\not{E}_T, \text{charm tag})$ vs. $\Delta\phi(\not{E}_T, \text{null tag})$	2	✓	

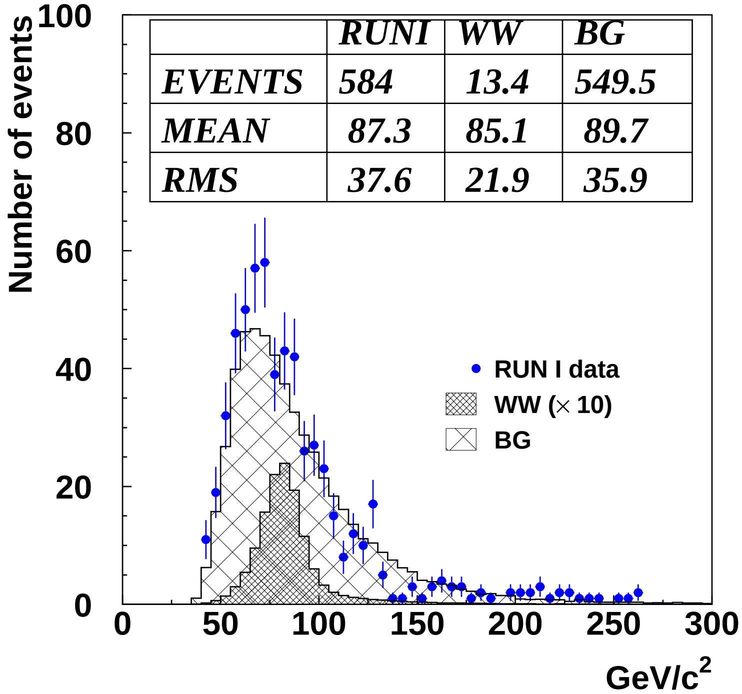

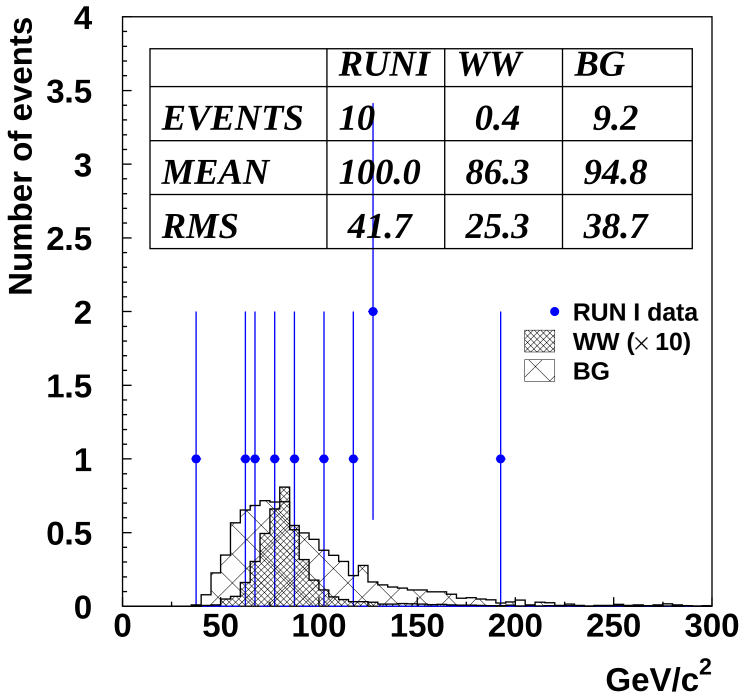

Figure 5.22: Dijet mass distributions for Run 1 data and simulations. Top: $W + ud$ sample. Bottom: $W + cs$ sample.

Chapter 6

Results and discussion

6.1 Expectations

The top portions of Figures 6.1 and 6.2 show distributions of the global likelihood for signal, background, and Run 1 data. The bottom portions show how the signal over background ratio S/B and the significance $S/\sqrt{B}$ vary with the global likelihood cut in the $W + ud$ and $W + cs$ samples.

In the previous section, we used all available parameters to define the global likelihood variable. It is however of some interest to study separately the background rejection power of three different combinations of these parameters: the quark-gluon jet discrimination parameters (charm tagging, charged track multiplicity, and jet charge), the W^+W^- kinematical parameters (η asymmetry of W pair, $\Delta\phi$ correlations between W^+W^- decay products, and dijet mass), and all parameters except the dijet mass. For each of these three combinations we form a global likelihood variable, choose the global likelihood cut that maximizes the signal significance in the sample under consideration ($W + cs$ or $W + ud$), and calculate the resulting signal over background ratio and signal significance. Table 6.1 summarizes this calculation.

It shows that both the quark-gluon discrimination and W^+W^- kinematical parameters improve the signal over background ratio and signal significance in the $W + ud$ and $W + cs$ samples. Unfortunately, the last two rows of the table clearly indicate that the signal significance is too low to permit observation of W pairs in the lepton+dijet mode in Run 1. We will therefore set upper limits on W^+W^- production instead. To calculate, with confidence level CL, an upper limit $N_S^{U.L.}$ on the number of signal events, we use a following equation:

$$1\text{−CL} \;=\; \frac{\displaystyle\sum_{n=0}^{n=n_\circ} \frac{1}{\sqrt{2\pi}\,N_S^{U.L.}\,\delta A_S} \int_0^\infty\!\!\int_0^\infty P(n;\mu'_B+\mu'_S)\; e^{-\frac{1}{2}\left(\frac{\mu'_B-\mu_B}{\sigma_B}\right)^2} e^{-\frac{1}{2}\left(\frac{\mu'_S-N_S^{U.L.}}{N_S^{U.L.}\,\delta A_S}\right)^2} d\mu'_B\, d\mu'_S}{\displaystyle\sum_{n=0}^{n=n_\circ} \int_0^\infty P(n;\mu'_B)\; e^{-\frac{1}{2}\left(\frac{\mu'_B-\mu_B}{\sigma_B}\right)^2} d\mu'_B} \tag{6.1}$$

where $n_\circ$ is the number of events observed, σ_B is the absolute uncertainty on the expected number of background events μ_B, and δA_S is the fractional uncertainty on the signal acceptance A_S. All our calculations will be based on a 95% confidence level CL. To transform an upper limit on the number of W^+W^- events into an upper limit on the W^+W^- production cross section we use the equation:

$$\sigma^{U.L.} = \left(N_S^{U.L.}/N_{WW}\right) \times \sigma_{WW}^{theory} \tag{6.2}$$

where N_{WW} is the number of W^+W^- events expected on the basis of the theoretical cross section σ_{WW}^{theory}, the Run 1 integrated luminosity, and the appropriate W^+W^- acceptance and efficiency.

We now determine the global likelihood cut value that will yield the lowest *expected* upper limit. The solution $\sigma^{U.L.}$ of the above equation depends, among other things, on the observed number of events $n_\circ$. Therefore, the expected upper limit will be obtained by averaging $\sigma^{U.L.}$ over all admissible values of $n_\circ$:

$$\langle\sigma^{U.L.}\rangle \;=\; \sum_{n_\circ=0}^{\infty} \frac{(\mu_B+\mu_S)^{n_\circ}}{n_\circ!}\; e^{-(\mu_B+\mu_S)}\; \sigma^{U.L.}(n_\circ), \tag{6.3}$$

where μ_S is the expected number of signal events and all other symbols are as defined previously. Table 6.2 lists expected upper limits as a function of the global likelihood cut in the $W+ud$ and $W+cs$ samples.

From this table we determine the optimal global likelihood cuts to be:

$$L(cs) \;>\; 0.0 \tag{6.4}$$
$$L(ud) \;>\; 1.5 \tag{6.5}$$

Finally, Table 6.3 gives the numbers of $W+cs$ and $W+ud$ events remaining after these global likelihood cuts.

Table 6.1: Expected signal over background ratio and signal significance for various combinations of variables, in the $W + cs$ and $W + ud$ samples.

	Sample	No cut	only q-g discrimination	only WW kin. variables	All variables except M_{jj}	All variables
S/BG	$W+cs$	0.04	0.07	0.12	0.10	0.14
	$W+ud$	0.02	0.04	0.05	0.04	0.07
$S/\sqrt{BG}$	$W+cs$	0.13	0.15	0.18	0.17	0.19
	$W+ud$	0.58	0.61	0.68	0.62	0.73

Table 6.2: Expected upper limits as a function of global likelihood cut. The background and signal uncertainties σ_B/μ_B and σ_S/μ_S are taken from section 6.2

$W + cs$ sample ($\sigma_B/\mu_B = 20\%$, $\sigma_S/\mu_S = 15\%$)				$W + ud$ sample ($\sigma_B/\mu_B = 15\%$, $\sigma_S/\mu_S = 10\%$)			
G.L. cut	μ_B	μ_S	$\langle\sigma^{U.L.}\rangle$ (pb)	G.L. cut	μ_B	μ_S	$\langle\sigma^{U.L.}\rangle$ (pb)
−1.0	4.66	0.360	195.10	0.0	182.9	9.51	70.53
−0.6	3.79	0.343	190.28	0.4	143.2	8.54	64.50
−0.4	3.43	0.333	189.20	0.8	93.7	6.89	57.60
−0.2	3.10	0.322	189.18	1.1	61.6	5.43	53.83
0.0	2.90	0.317	188.54	1.2	52.5	4.94	53.04
0.2	2.56	0.300	191.20	1.4	36.9	3.94	52.77
0.4	2.21	0.285	192.60	1.5	30.1	3.46	53.03
0.6	1.95	0.267	198.13	1.6	24.5	3.00	54.12
0.8	1.65	0.249	202.45	2.0	8.65	1.50	63.75
1.0	1.40	0.228	211.44	2.4	2.69	0.60	99.36

Table 6.3: Number of expected signal and background events in the $W + cs$ and $W + ud$ samples after the global likelihood cut. $\varepsilon =$ (Number of events after G.L. cut)/(Number of events before G.L. cut)

	$W + cs$ sample				$W + ud$ sample			
	e	μ	Total	$\varepsilon_{G.L}(\%)$	e	μ	Total	$\varepsilon_{G.L}(\%)$
$W + 2jets$	0.21	0.21	0.41	26.6	15.34	14.21	29.55	6.2
$Non - W$	0.00	0.00	0.00	0.00	2.33	1.00	3.33	15.6
$t\bar{t}$	0.17	0.14	0.31	16.0	0.09	0.06	0.14	2.8
$single\ top$	0.17	0.18	0.35	33.7	0.09	0.10	0.19	5.2
$Wb\bar{b}$	0.16	0.16	0.32	31.4	0.07	0.06	0.13	4.5
$Wc\bar{c}$	0.13	0.13	0.25	33.8	0.18	0.19	0.37	6.3
Wc	0.45	0.42	0.86	33.3	0.83	0.80	1.63	6.0
WW	0.16	0.15	0.32	78.0	1.86	1.70	3.56	26.6
MC total	1.44	1.39	2.83	29.6	20.79	18.11	38.90	7.0
Run I	1	1	2	20.0	33	10	43	7.3

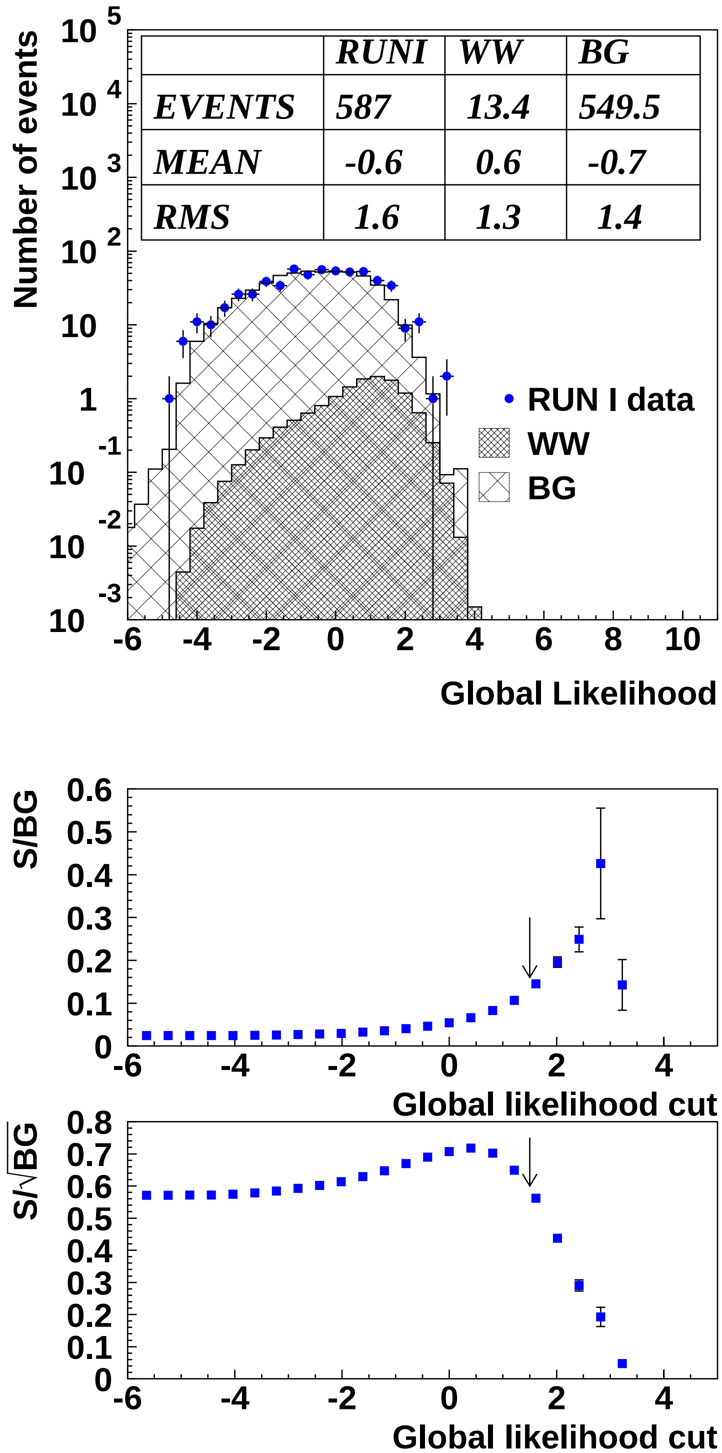

Figure 6.1: Top: global likelihood distribution for $W + ud$ sample; middle: signal over background fraction versus global-likelihood cut; bottom: signal significance versus global-likelihood cut.

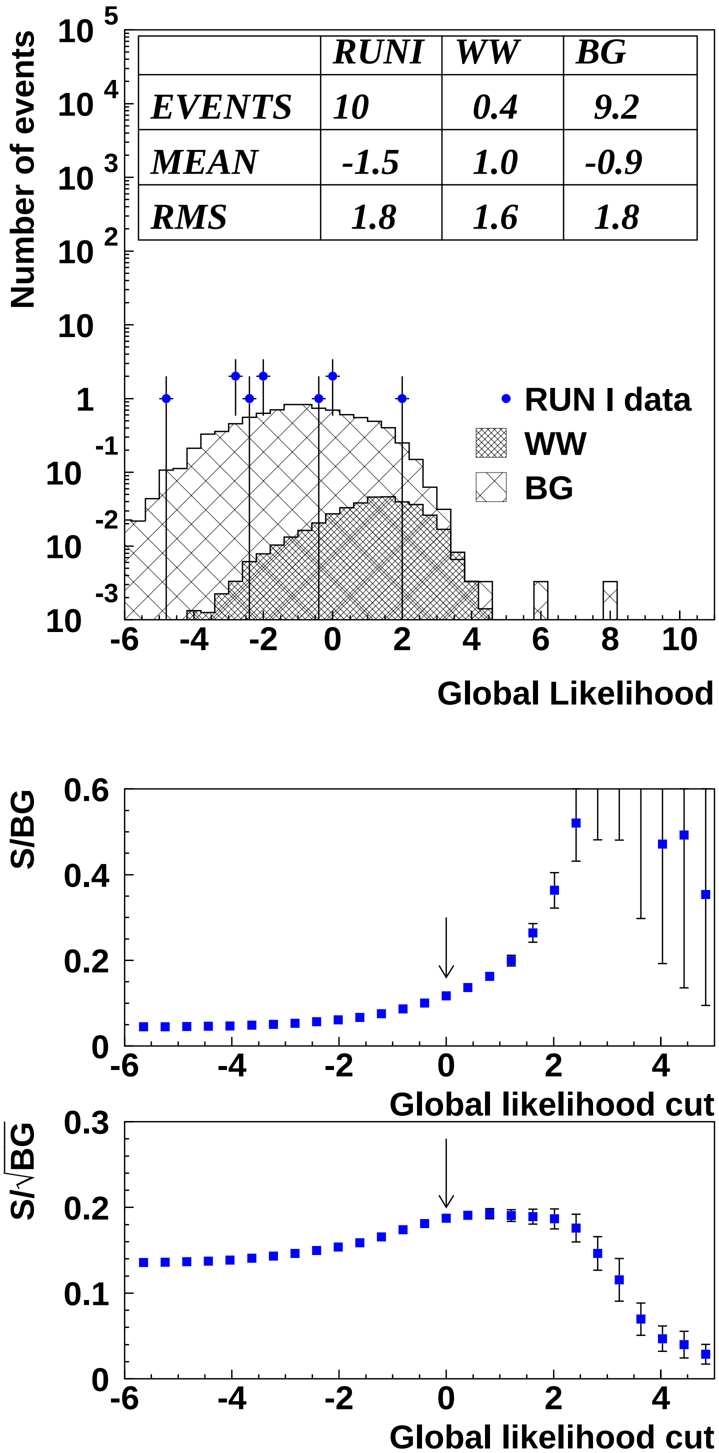

Figure 6.2: Top: global likelihood distribution for $W + cs$ sample; middle: signal over background fraction versus global-likelihood cut; bottom: signal significance versus global-likelihood cut.

6.2 Systematic uncertainty

We consider the following systematic uncertainties in the expected numbers of signal and/or background events:

- Jet transverse energy

  We estimate this systematic uncertainty with the same method as for the top mass measurement at CDF [35].

- Hard initial state radiation (ISR)

  We take half the difference between PYTHIA with and without initial state radiation. This systematic only applies to the expected signal.

- Hard final state radiation (FSR)

  We take half the difference between PYTHIA with no ISR and PYTHIA with no ISR where the two jets match the partons at GENP level (no hard final state radiation). This systematic only applies to the expected signal.

- Parton distribution function (PDF)

  For this uncertainty we follow the policy of the W cross section group, which currently reuses the results of a Run 1 study ([36]). This amounts to a $\pm 1.6\%$ uncertainty on the W acceptance.

- Q^2 scale

  We take the difference between the two scales $Q^2 = \langle p_T \rangle^2$ (default) and $Q^2 = M_W^2$, and symmetrize the resulting systematic shift. This systematic only applies to the W+QCD jets background simulation.

- Tracking efficiency ($\mathcal{CM}_|, Q_{jet}$)

  In Monte-Carlo simulations, tracking is done based on average CTC hit efficiencies that were measured from B0 data. In the data, the hit efficiencies were affected by instantaneous luminosity and tended to deteriorate as the run progressed. There may therefore be some effect due to the difference between average and actual hit efficiencies in the data. We first note that the charged track multiplicity and jet charge distributions in the data are reasonably well modeled by the simulation (see Figures 5.6, 5.15, and 5.16). An absolute uncertainty of about $\pm 3\%$ is estimated for the tracking efficiency inside jets in Run 1 dijet events with dijet mass around 80 GeV/c^2. For the present analysis we double this uncertainty and use $\pm 6\%$.

- Non-W background

  Section 4.6 describes the calculation of this background using the "isolation versus $\not\!\!E_T$" method. In the search sample, the fraction of non-W background is calculated to be 5.8% for electron events and 3.2% for muon events. Systematic uncertainties on these results can be estimated by varying the upper isolation threshold, i.e. the lower boundary of regions B and C. If we move the upper isolation threshold from 0.3 to 0.1 (0.5), the non-W fraction changes from 5.8% to 6.6% (respectively 8.5%) in electron events and from 3.2% to 3.4% (respectively 3.7%) in muon events.

- Top background

  Here we use the theoretical error on the $t\bar{t}$ production cross section: $\sigma_{t\bar{t}} = 5.0^{+0.1}_{-0.4}$ pb, on s-channel single-top: $\sigma_{W^\star} = 0.73 \pm 0.10$ pb, and on t-channel single-top: $\sigma_{Wg} = 1.70 \pm 0.29$ pb.

- $Wb\bar{b}, Wc\bar{c}$ background

  Here too we consider the theoretical error on the cross sections (± 0.9 pb).

- Charm tagging efficiency

  For this we consider the difference in JETPROBABILITY tagging efficiency between data and simulations. Given that track selection in the SECVTX module is tighter than in the JETPROBABILITY module, we estimate that a 10% uncertainty is adequate.

- The error on the luminosity

  The total uncertainty on the integrated luminosity (106 pb^{-1}) is 4%.

Tables 6.4 and 6.5 list all the systematic uncertainties on the expected numbers of background and signal events. Some of these uncertainties, such as those on jet E_T, tracking and tagging efficiencies, and integrated luminosity, are clearly correlated between signal and background.

6.3 Consistency check between simulation and real data

One way to check the modeling of W-pair events by PYTHIA is to compare features such as $\mathcal{CM}_j$, Q_{total} and M_{jj} with the CDF double b-tagged $W + 4$jets top sample. The two untagged jets in each event of that sample can be associated with the decay products of a hadronic W boson from top decay. The comparison is shown in Figure

Table 6.4: Systematic uncertainties in the expected number of events in the $W + ud$ sample after the global likelihood cut of eq. (6.5).

	WW	
	$-\Delta N/N$	$+\Delta N/N$
E_t scale	0.4	0.3
ISR	0	15
FSR	0	0
PDF	1.6	1.6
ϵ_{track}	5	5
$\epsilon_{charm\ tag}$	0	0
Luminosity	4	4
Total	6%	16%

	BG	
	$-\Delta N/N$	$+\Delta N/N$
E_t scale	1	2
QCD scale	10	10
PDF	1.6	1.6
ϵ_{track}	10	10
Non W	0	0
Top	0	0
$Wb\bar{b}$	0	0
$Wc\bar{c}$	0	0
$\epsilon_{charm\ tag}$	0	0
Luminosity	4	4
Total	15%	15%

6.3. Data and simulation appear to agree within the limited statistics of the Run 1 sample.

A statistically more meaningful test is provided by directly comparing data and simulation in the control and search samples, using kinematic properties such as uncorrected jet E_T (Figures 3.1 and 3.2), jet detector η (Figures 3.3 and 3.4), dijet opening angle (Figure 3.5), and dijet mass (Figures 6.4 and 5.22). The only discrepancy that really stands out occurs in the control sample, where the simulation fails to reproduce the leading jet E_T spectrum for $E_T < 30$ GeV, and the dijet invariant mass distribution for $M_{jj} < 70$ GeV/c^2. The modeling of the search sample however, is better.

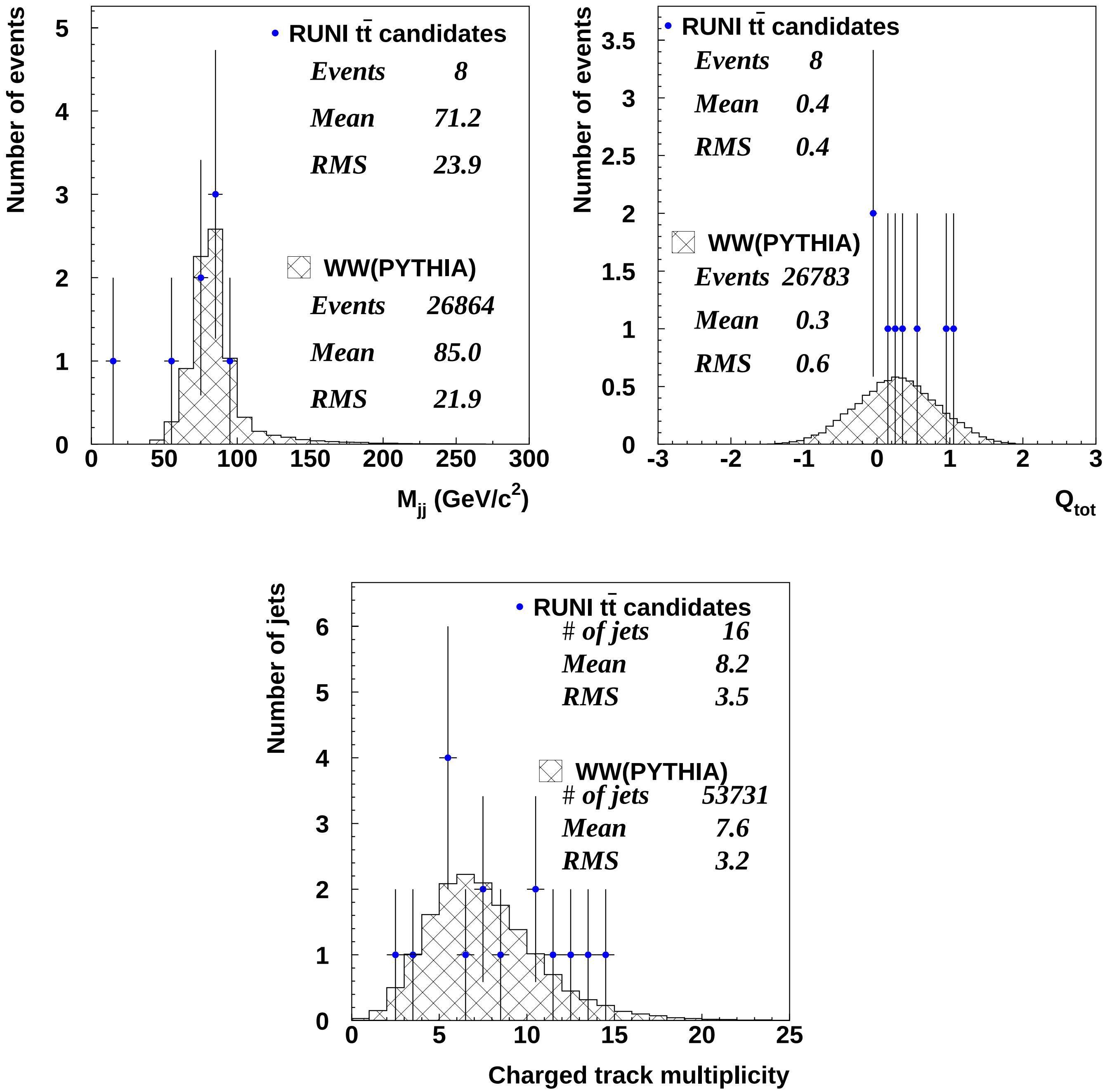

Figure 6.3: Comparison of PYTHIA W^+W^- events with CDF Run 1 double-tag $W+4$jets sample. Top left: dijet invariant mass; top right: Q_{total}; bottom: charged track multiplicity.

Table 6.5: Systematic uncertainties in the expected number of events in the $W+cs$ sample after the global likelihood cut of eq. (6.4).

	WW	
	$-\Delta N/N$	$+\Delta N/N$
E_t scale	4	4
ISR	0	8
FSR	0	0
PDF	1.6	1.6
ϵ_{track}	1	1
$\epsilon_{charm\ tag}$	10	10
Luminosity	4	4
Total	12%	14%

	BG	
	$-\Delta N/N$	$+\Delta N/N$
E_t scale	1	1
QCD scale	8	8
PDF	1.6	1.6
ϵ_{track}	12	12
Non W	0	0
Top	4	2
$Wb\bar{b}$	1	1
$Wc\bar{c}$	1	1
$\epsilon_{charm\ tag}$	10	10
Luminosity	4	4
Total	19%	18%

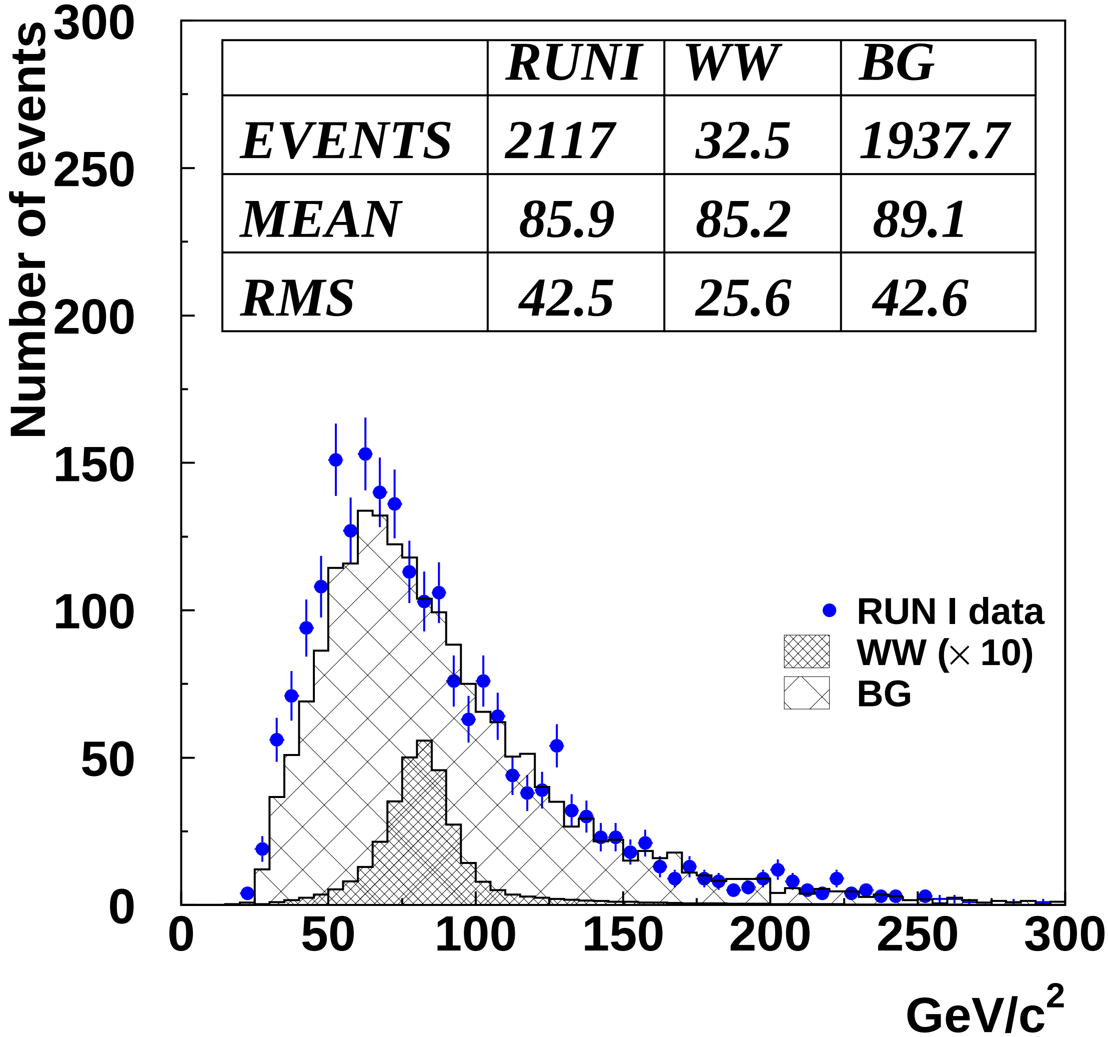

Figure 6.4: Dijet mass for the CDF control sample, superimposed on Monte Carlo simulations for signal (PYTHIA) and background (VECBOS).

6.4 Upper limit on W pair production cross section

In this section we use equations (6.1) and (6.2) to calculate upper limits on W^+W^- production in Run 1 data.

For the $W + cs$ sample, we observed 2 events, the background expectation is $\mu_B = 2.51 \pm 0.06(\text{stat})^{+0.45}_{-0.48}(\text{syst})$, and the signal expectation is $N_{W^+W^-} = 0.32 \pm 0.01(\text{stat}) \pm 0.04(\text{syst})$. The upper limit is found to be:

$$\sigma(p\bar{p} \to W^+W^-) \;\leq\; 145 \text{ pb at } 95\% \text{ C.L.} \tag{6.6}$$

For the $W + ud$ sample, we observed 43 events, the background expectation is $\mu_B = 35.3 \pm 1.4(\text{stat}) \pm 5.3(\text{syst})$, and the signal expectation is $N_{W^+W^-} = 3.6 \pm 0.1(\text{stat})^{+0.6}_{-0.2}(\text{syst})$. The upper limit is found to be:

$$\sigma(p\bar{p} \to W^+W^-) \;\leq\; 65 \text{ pb at } 95\% \text{ C.L.} \tag{6.7}$$

Combining the $W + cs$ and $W + ud$ samples, we obtain the following upper limit:

$$\sigma(p\bar{p} \to W^+W^-) \;\leq\; 61 \text{ pb at } 95\% \text{ C.L.} \tag{6.8}$$

6.5 Check of the upper limit calculation

We checked the above upper limit(U.L.) using a toy Monte Carlo which generates the numbers of signal and background events in a trial according to the following probability distribution.

$$\mathcal{P}_{\mu,\sigma}(n) = \int_0^\infty P_x(n) G_{\mu,\sigma}(x) dx \tag{6.9}$$

where $\mathcal{P}_{\mu,\sigma}(n)$ is defined with $P_\mu(n)$ (Poisson distribution) and $G_{\mu,\sigma}(x)$ (Gaussian distribution).

An upper limit ($N_s^{U.L.}$) is set at an given CL, including the total systematic uncertainty (σ_{syst}), by solving the following equation for $N_s^{U.L.}$:

$$1 - CL = \sum_{n=0}^{N_{obs}} \mathcal{P}_{N_s^{U.L.},\sigma_{syst}}(n) \tag{6.10}$$

where N_{obs} is the number of observed events.

Figure 6.5 shows the upper limit of W pair production cross-section as a function of confidence level(CL) for the combined sample.

$$\sigma(p\bar{p} \to W^+W^-) \leq 62 \text{ pb at } 95\% \text{ C.L.}$$

This U.L. is consistent with the U.L. calculation of the previous section.

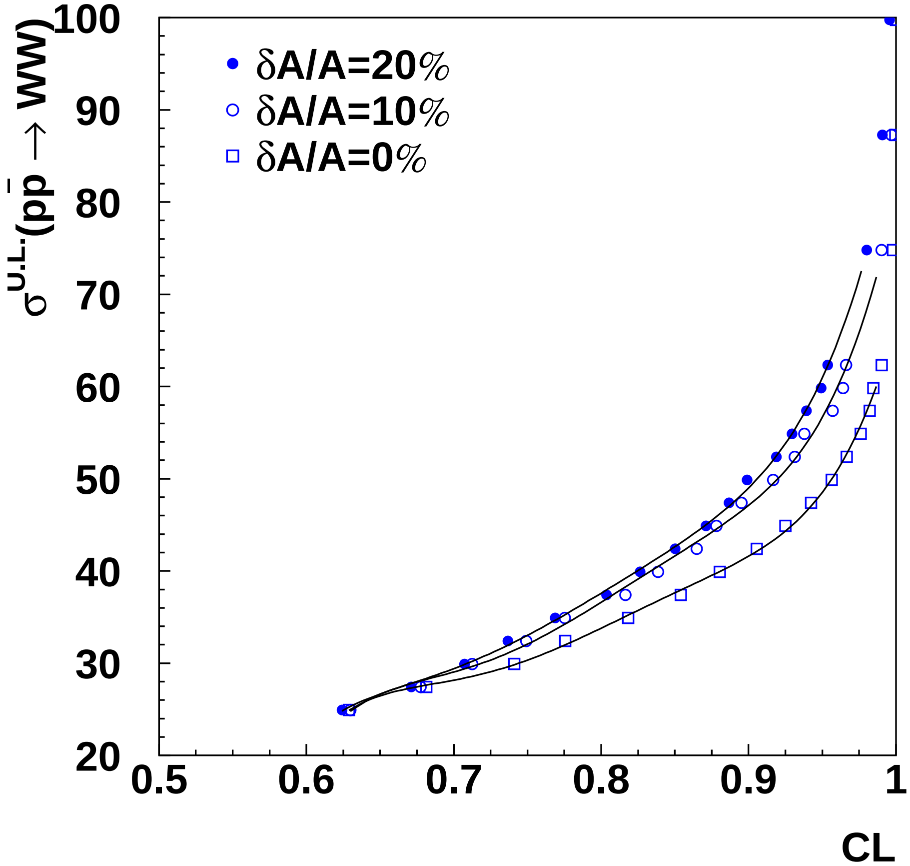

Figure 6.5: The upper limit of W pair production cross-section as a function of confidence level(CL) for the combined sample.

We generated 100,000 sets of four integers $(N_b^{ud}, N_b^{cs}, N_s^{ud}, N_s^{cs})$, each set representing a Poisson fluctuation of the expected numbers of background and signal events in the $W+ud$ and $W+cs$ samples after the global likelihood cut, smeared by their uncertainties (Table 6.3). For each set we calculated a $W+ud$ and $W+cs$ combined upper limit on the W^+W^- production cross section. The results are shown in Figure 6.6. About 60% of the pseudo-experiments yield an upper limit between 40 and 80 pb. The upper limit obtained from Run 1 falls well within the bulk of the upper limit distribution.

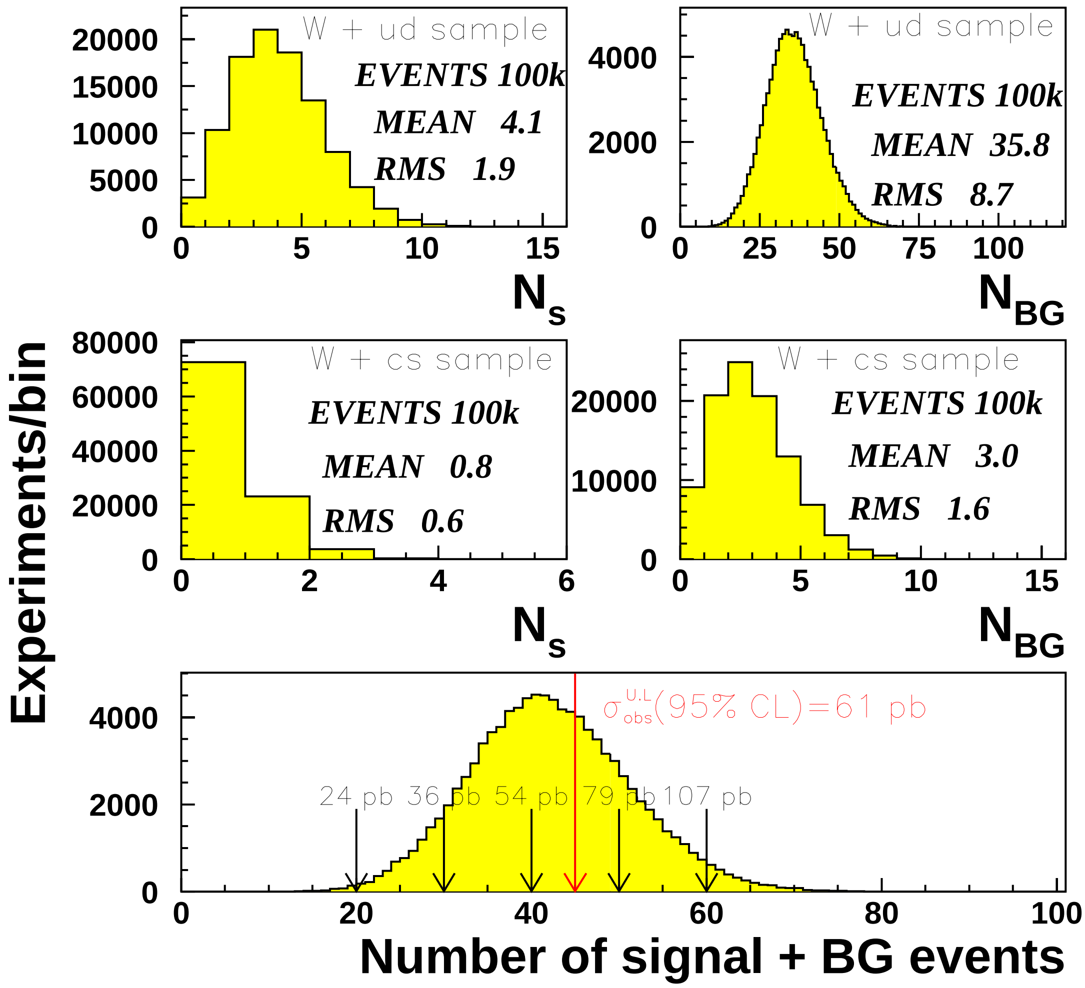

Figure 6.6: Pseudo-experiment check of the upper limit calculation. Top: distributions of the numbers of signal and background events in the $W + ud$ samples. Middle: distributions of the numbers of signal and background events in the $W + cs$ samples. Bottom: distribution of the total number of events in the $W + ud$ and $W + cs$ samples combined. For five values of this total number of events, each marked by a short arrow, the corresponding 95% C.L. upper limit on W^+W^- production is indicated. A longer arrow marks the Run 1 result.

Chapter 7

Conclusion

We searched for W-pair production in the lepton plus dijet channel, $W^+W^- \rightarrow \ell\nu jj$, using the full Run 1 data sample. In addition to kinematical variables that are characteristic of the W^+W^- final state, we used charm-jet tagging, jet charge and charged track multiplicity to improve the signal-to-background ratio.

After applying a global likelihood cut we observed 45 events while expecting $N_{W^+W^-} = 3.9 \pm 0.1(\text{stat}) \pm^{0.6}_{0.2}(\text{syst})$ signal events and $N_{BG} = 37.8 \pm 1.4(\text{stat}) \pm^{5.7}_{5.7}(\text{syst})$ background events in the combined $W + ud$ and $W + cs$ sample. The corresponding 95% C.L. upper limit on the W^+W^- production cross section is 61 pb. These results are summarized in Table 7.1.

Table 7.1: Summary of WW cross section upper limit.

	$W + cs$	$W + ud$	$W + cs$ & $W + ud$ combined
BG expectation(μ_B)	2.51	35.3	37.8
BG uncertainty(σ_B/μ_B (%))	19	15	15
# of observed events($n_\circ$)	2	43	45
Relative uncertainty on A_S (δA_S (%))	13	11	11
Signal acceptance(A_S (%))	0.1	1.16	1.26
95% C.L. $\sigma^{U.L.}$ (pb)	145	65	61

Appendix A

Effect of using H_T in the W^+W^- search

The variable H_T is defined as the sum of the transverse energies (or momenta) of all the "hard" objects in an event:

$$H_T \equiv E_T(lepton) + \not{E}_T + E_T^c(jet1) + E_T^c(jet2) \quad (A.1)$$

where $E_T^c(jet1)$ and $E_T^c(jet2)$ represent the corrected transverse energies of the leading and second-leading jets, respectively.

As shown in Figure A.1, H_T is strongly correlated with the dijet invariant mass. The effect on the signal over background ratio and on the signal significance of adding H_T to the global likelihood variable is shown in Figure A.2. This addition has very little effect on the signal significance.

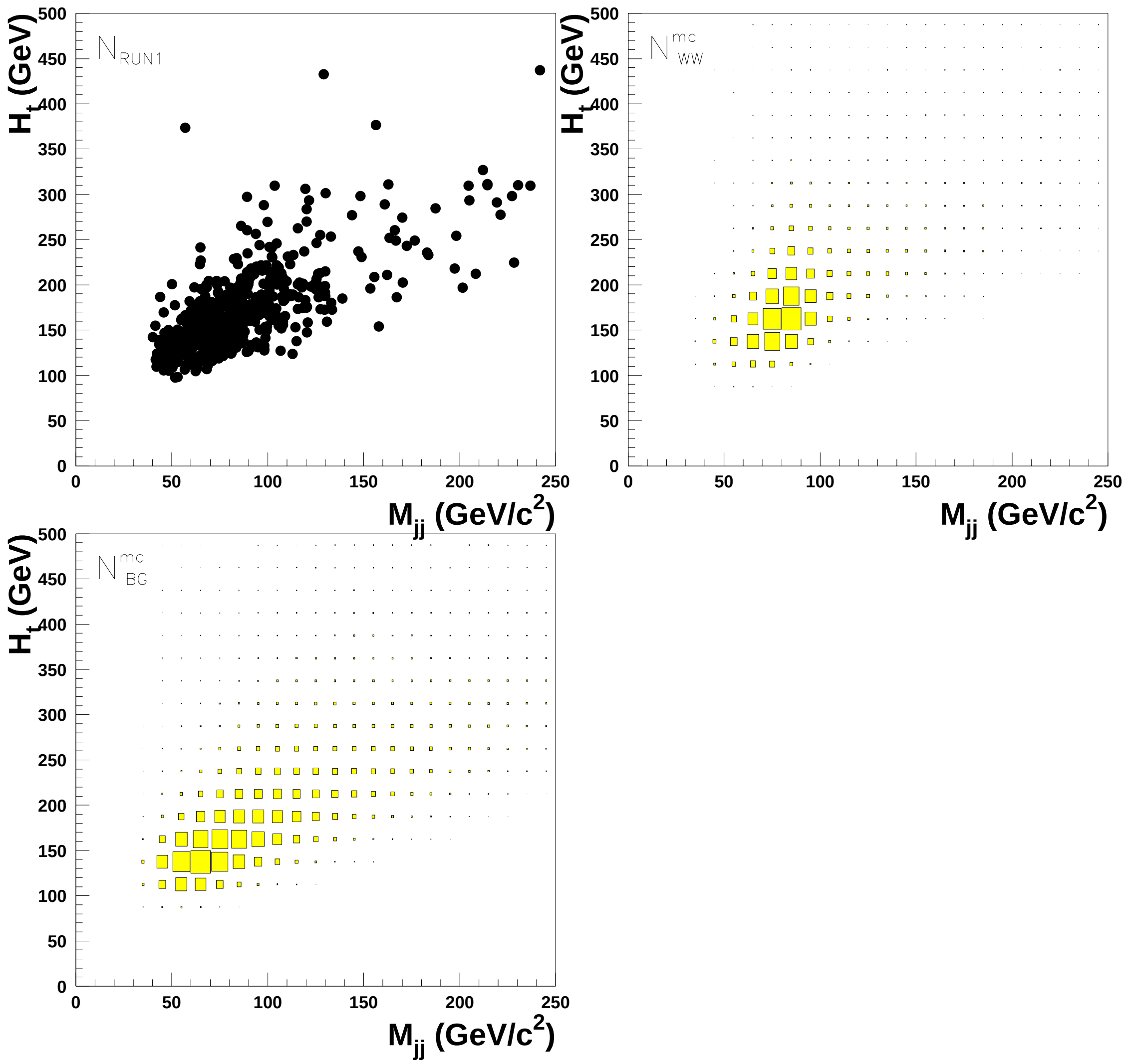

Figure A.1: Plot of H_T versus dijet mass. Top left: Run 1 data; top right: PYTHIA W^+W^-; bottom left: VECBOS background.

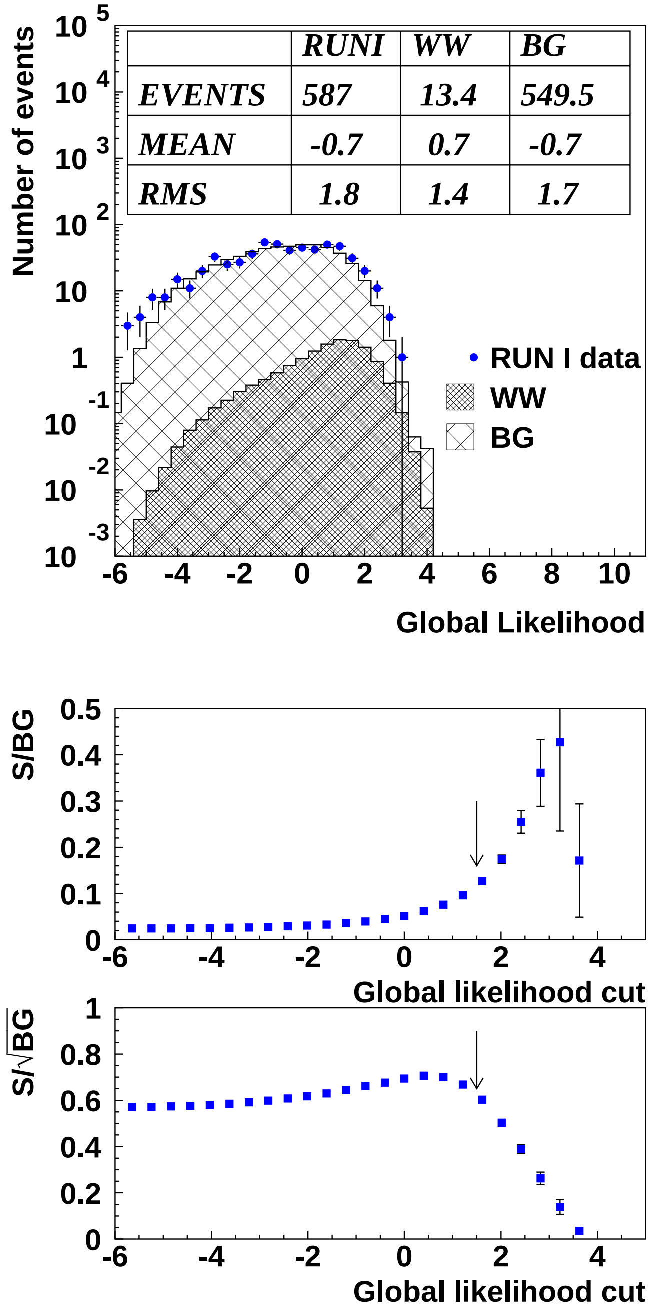

Figure A.2: Top: global likelihood distribution of $W+ud$ sample; middle: signal over background ratio as a function of global likelihood cut; bottom: signal significance as a function of global likelihood cut. For this plot the global likelihood variable includes H_T.

Appendix B

Identification of $W \to u\bar{d}$ and $W \to c\bar{s}$ using charm-tagging with JPBTAG

In this appendix we examine the possibility of basing the W-pair search analysis on the JETPROBABILITY tagging algorithm [31] only, instead of using the SECVTX algorithm as was done in section 5.1.1.

Figure B.1 shows the positive jet probability (JP^+) distributions of primary, bottom, and charm jets. The distributions for bottom and charm jets are enhanced near $JP^+ = 0$, as expected. For primary jets one expects the JP^+ distribution to be flat, but instead a dip is observed near zero. This can be understood as follows. The probability for the impact parameter significance of a given track in the data to be due to the detector resolution ("jet-probability of a single track") was derived from the *negative* side of the distribution of the signed impact parameter significance of tracks in the JET–50 data sample. For the jet-probability of a single track in the Monte Carlo, a HERWIG simulation of the JET–50 sample was used. Therefore, the jet-probability distribution will be perfectly flat only for JET–50 samples. On the other hand, the JET–50 samples (both data and Monte Carlo) contain a certain fraction of heavy-flavor jets, which enhance both the positive and negative jet-probability distributions near zero (see for example Figure 5 in reference [25]. Since a sample of primary jets contains no heavy-flavor, i.e. less heavy-flavor than a JET–50 sample, the jet-probability distribution of primary jets will exhibit a dip near zero.

We calculated the JETPROBABILITY tagging efficiency on bottom, charm, and primary jets for three different choices of JP^+ cut: $JP^+ < 0.01$, 0.05, and 0.10. Figures B.2 to B.4 show the result of this calculation. In order to achieve high charm purity by rejecting both b-jets and p-jets, we define a JP charm tag as being a jet passing the tight two-sided cut $0.001 < JP^+ < 0.01$. The efficiency of this cut on charm jets is about 9%, whereas it is only 0.2% on primary jets. Next, we define a *JP* null tag as being a jet with $JP^+ > 0.05$.

We are now ready to define two subsamples of the search sample, just as we did in section 5.1.1. The *JP* $W + cs$ subsample consists of events with one *JP* charm tag and one *JP* null tag, whereas the *JP* $W + ud$ subsample contains all events with two *JP* null tags. Figures B.5 to B.9 illustrate these subsample definitions in the plane of jet 1 JP^+ versus jet 2 JP^+ for Run 1 data, W^+W^- signal, and $W + 2$QCD jets, $Wb\bar{b}$, and $Wc\bar{c}$ backgrounds. Table B.1 shows the expected numbers of signal and background events in the *JP* $W + ud$ and $W + cs$ subsamples.

Table B.1: Expected numbers of signal and background events in the *JP* $W + cs$ and $W + ud$ subsamples. $\varepsilon =$ (Number of events in subsample)/(Number of events in search sample)

	$W + cs$ sample				$W + ud$ sample			
	e	μ	Total	ε_{JP+} (%)	e	μ	Total	ε_{JP+} (%)
$W + 2jets$	0.48	0.46	0.94	0.2	239.54	227.70	467.24	96.6
$Non - W$	0.67	0.29	0.96	3.3	15.48	10.16	25.64	88.5
$t\bar{t}$	0.53	0.45	0.98	10.4	2.67	2.33	5.01	53.2
single top	0.36	0.37	0.73	13.8	1.72	1.71	3.43	65.0
$Wb\bar{b}$	0.31	0.29	0.60	10.4	1.31	1.29	2.60	45.1
$Wc\bar{c}$	0.26	0.26	0.53	7.7	2.50	2.42	4.92	71.5
Wc	0.74	0.72	1.46	4.8	12.88	12.37	25.25	82.4
WW	0.17	0.14	0.31	2.2	6.61	6.05	12.67	90.5
MC total	3.51	2.99	6.50	1.1	282.74	264.04	546.77	93.5
Run I	3	2	5	0.8	290	279	569	90.2

Figures B.10 and B.11 show the distributions of the global likelihood. Table B.2 shows the number of *JP* $W + ud$ and $W + cs$ events after the global likelihood cut. The systematic uncertainties are listed in Tables B.3 and B.4.

Table B.2: Expected numbers of signal and background events in the *JP* $W + cs$ and $W + ud$ subsamples after the global likelihood cut. $\varepsilon =$ (Number of events in subsample after the G.L cut)/(Number of events in subsample before the G.L. cut)

	$W + cs$ sample				$W + ud$ sample			
	e	μ	Total	$\varepsilon_{G.L}(\%)$	e	μ	Total	$\varepsilon_{G.L}(\%)$
$W + 2jets$	0.08	0.11	0.19	20.2	13.98	13.44	27.43	5.9
$Non - W$	0.00	0.03	0.03	3.1	1.67	0.60	2.26	8.8
$t\bar{t}$	0.07	0.06	0.13	13.3	0.07	0.05	0.12	2.4
$single\,top$	0.08	0.08	0.16	21.9	0.08	0.09	0.16	4.7
$Wb\bar{b}$	0.07	0.07	0.14	23.3	0.05	0.05	0.10	3.8
$Wc\bar{c}$	0.07	0.07	0.14	26.4	0.14	0.15	0.29	5.9
Wc	0.15	0.18	0.33	22.6	0.73	0.67	1.40	5.5
WW	0.10	0.08	0.18	58.1	1.69	1.54	3.22	25.4
MC total	0.63	0.70	1.33	20.5	18.52	16.67	35.20	6.4
Run I	1	0	1	20.0	29	10	39	6.9

Table B.3: Systematic uncertainties in the expected numbers of signal and background events for the *JP* $W + ud$ subsample after the global likelihood cut of eq. (6.5).

	WW signal	
	$-\Delta N/N$	$+\Delta N/N$
E_T scale	0.5	0.4
ISR	0	15
FSR	0	0
PDF	1.6	1.6
ϵ_{track}	6	6
ϵ_{c-tag}	0	0
Luminosity	4	4
Total	7%	17%

	Backgrounds	
	$-\Delta N/N$	$+\Delta N/N$
E_T scale	1	2
QCD scale	10	10
PDF	1.6	1.6
ϵ_{track}	11	11
Non W	0	0
Top	0	0
$Wb\bar{b}$	0	0
$Wc\bar{c}$	0	0
ϵ_{c-tag}	0	0
Luminosity	4	4
Total	15%	15%

Table B.4: Systematic uncertainties in the expected numbers of signal and background events for the *JP* $W + cs$ subsample after the global likelihood cut of eq. (6.4).

	WW signal	
	$-\Delta N/N$	$+\Delta N/N$
E_T scale	3	3
ISR	0	9
FSR	0	0
PDF	1.6	1.6
ϵ_{track}	3	3
$\epsilon_{charm\ tag}$	10	10
Luminosity	4	4
Total	12%	15%

	Backgrounds	
	$-\Delta N/N$	$+\Delta N/N$
E_T scale	1	1
QCD scale	7	7
PDF	1.6	1.6
ϵ_{track}	11	11
Non W	0	0
Top	4	2
$Wb\bar{b}$	1	1
$Wc\bar{c}$	1	1
$\epsilon_{charm\ tag}$	10	10
Luminosity	4	4
Total	17%	17%

For the *JP* $W+cs$ subsample, we observed 1 event, the background expectation is $\mu_B = 1.15 \pm 0.02(\text{stat})\pm^{0.20}_{0.20}(\text{syst})$ and the signal expectation is $N_{W^+W^-} = 0.18 \pm 0.01(\text{stat})\pm^{0.03}_{0.02}(\text{syst})$. The upper limit is found to be:

$$\sigma(p\bar{p} \to W^+W^-) \ \leq \ 223 \text{ pb at } 95\% \text{ C.L.} \tag{B.1}$$

For the *JP* $W+ud$ subsample, we observed 39 events, the background expectation is $\mu_B = 32.0 \pm 1.4(\text{stat})\pm^{4.8}_{4.8}(\text{syst})$ and the signal expectation is $N_{W^+W^-} = 3.2 \pm 0.1(\text{stat})\pm^{0.5}_{0.2}(\text{syst})$. The upper limit is found to be:

$$\sigma(p\bar{p} \to W^+W^-) \ \leq \ 69 \text{ pb at } 95\% \text{ C.L.} \tag{B.2}$$

Finally, combining the *JP* $W+cs$ and $W+ud$ subsamples yields the following upper limit:

$$\sigma(p\bar{p} \to W^+W^-) \ \leq \ 65 \text{ pb at } 95\% \text{ C.L.} \tag{B.3}$$

We performed the same check on our *JP* upper limit calculation as in section 6.5. The result is shown in Figure B.12.

The expected Run 1 upper limit extracted from the JETPROBABILITY analysis is 56.7 pb, corresponding to observing a total number of 37.0 events in the *JP* $W+ud$ and $W+cs$ subsamples combined. For the SECVTX-based analysis described in the main part of this document, the expected upper limit is 56.0 pb, corresponding to a total of 41.5 events observed. The SECVTX analysis is therefore only slightly better than the JETPROBABILITY one. Since the two analyses are strongly correlated, we had to choose one, and the winner was SECVTX.

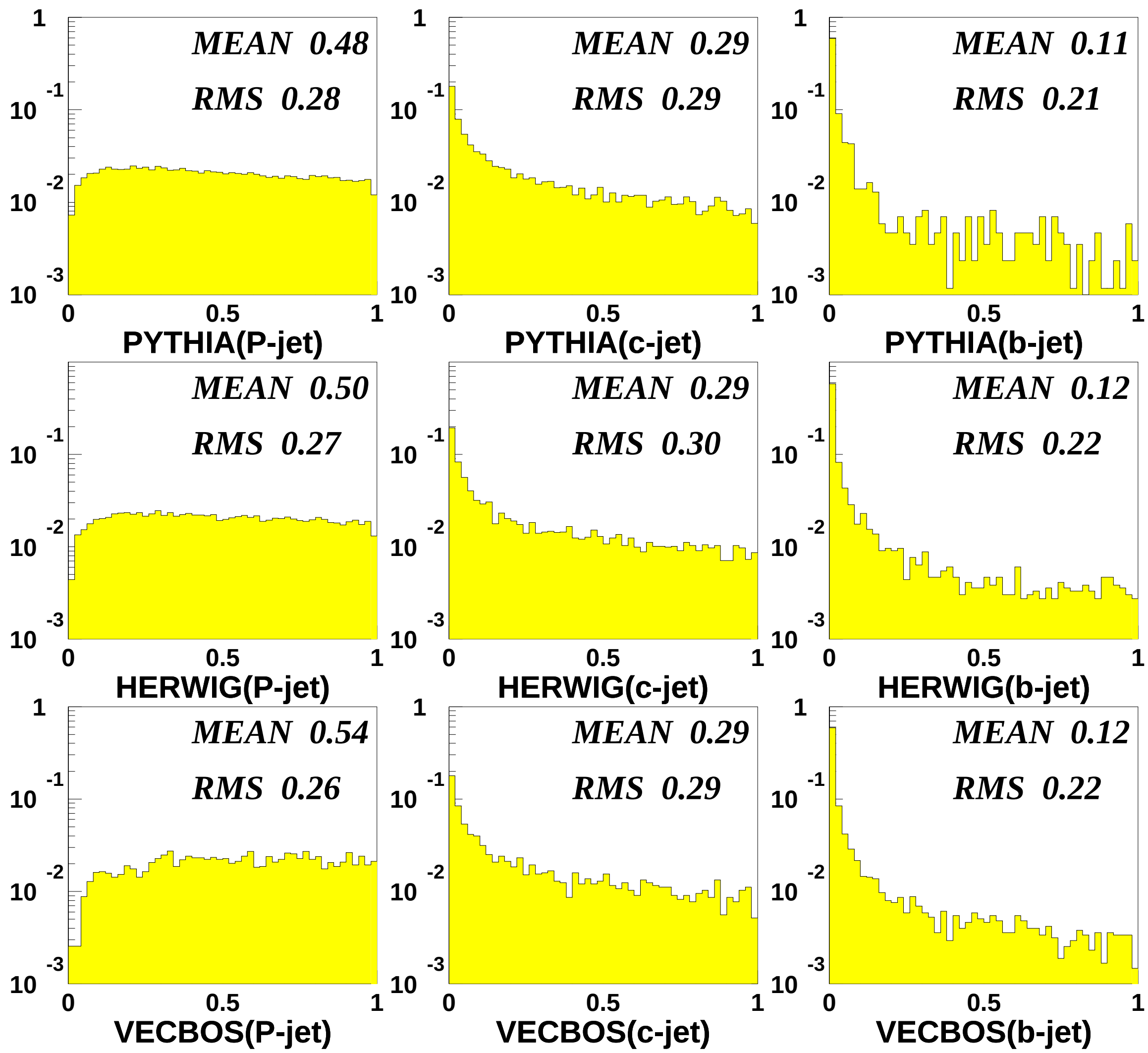

Figure B.1: Positive jet probability distributions of p-, c- and b-jets for PYTHIA, HERWIG, and VECBOS; p-jets are primary jets initiated by u, d, or s quarks, or by gluons.

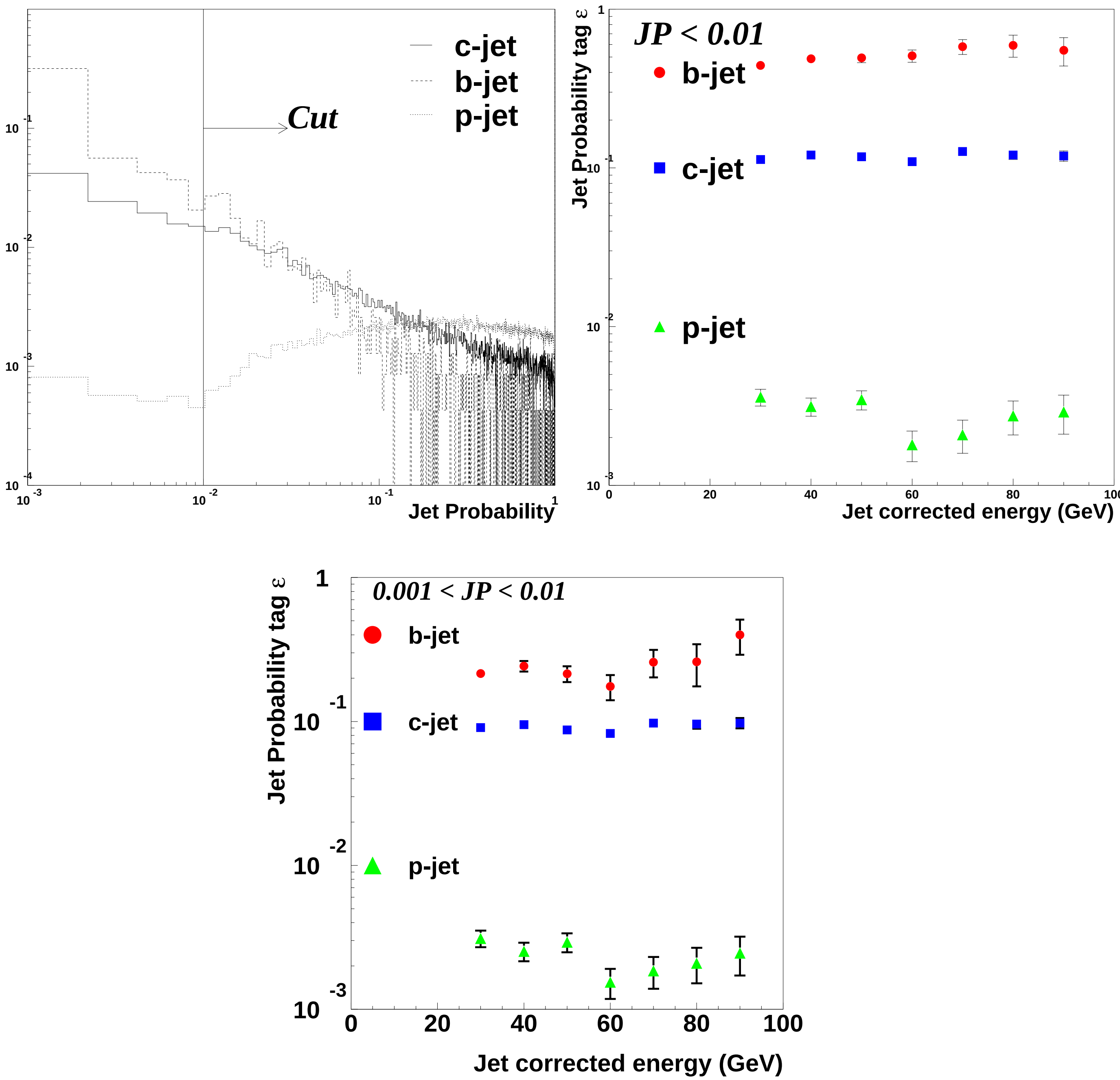

Figure B.2: Study of jet probability with PYTHIA W^+W^- events. Top left: jet probability distributions of c-, b-, and p-jets. Top right: efficiency of the cut $JP^+ < 0.01$ for c-, b-, and p-jets. Bottom: efficiency of the cut $0.001 < JP^+ < 0.01$ for c-, b-, and p-jets.

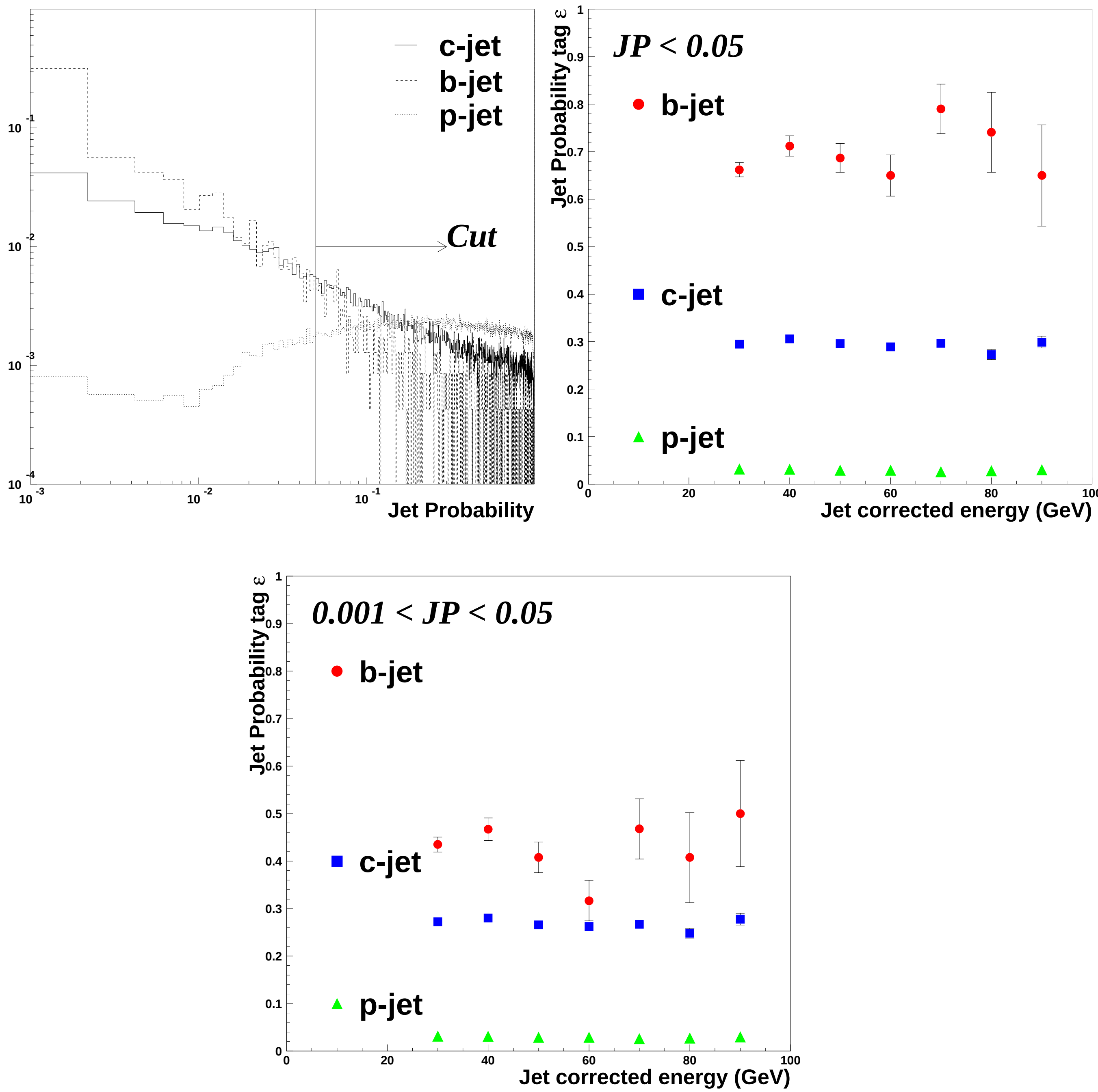

Figure B.3: Study of jet probability with PYTHIA W^+W^- events. Top left: jet probability distributions of c-, b-, and p-jets. Top right: efficiency of the cut $JP^+ < 0.05$ for c-, b-, and p-jets. Bottom: efficiency of the cut $0.001 < JP^+ < 0.05$ for c-, b-, and p-jets.

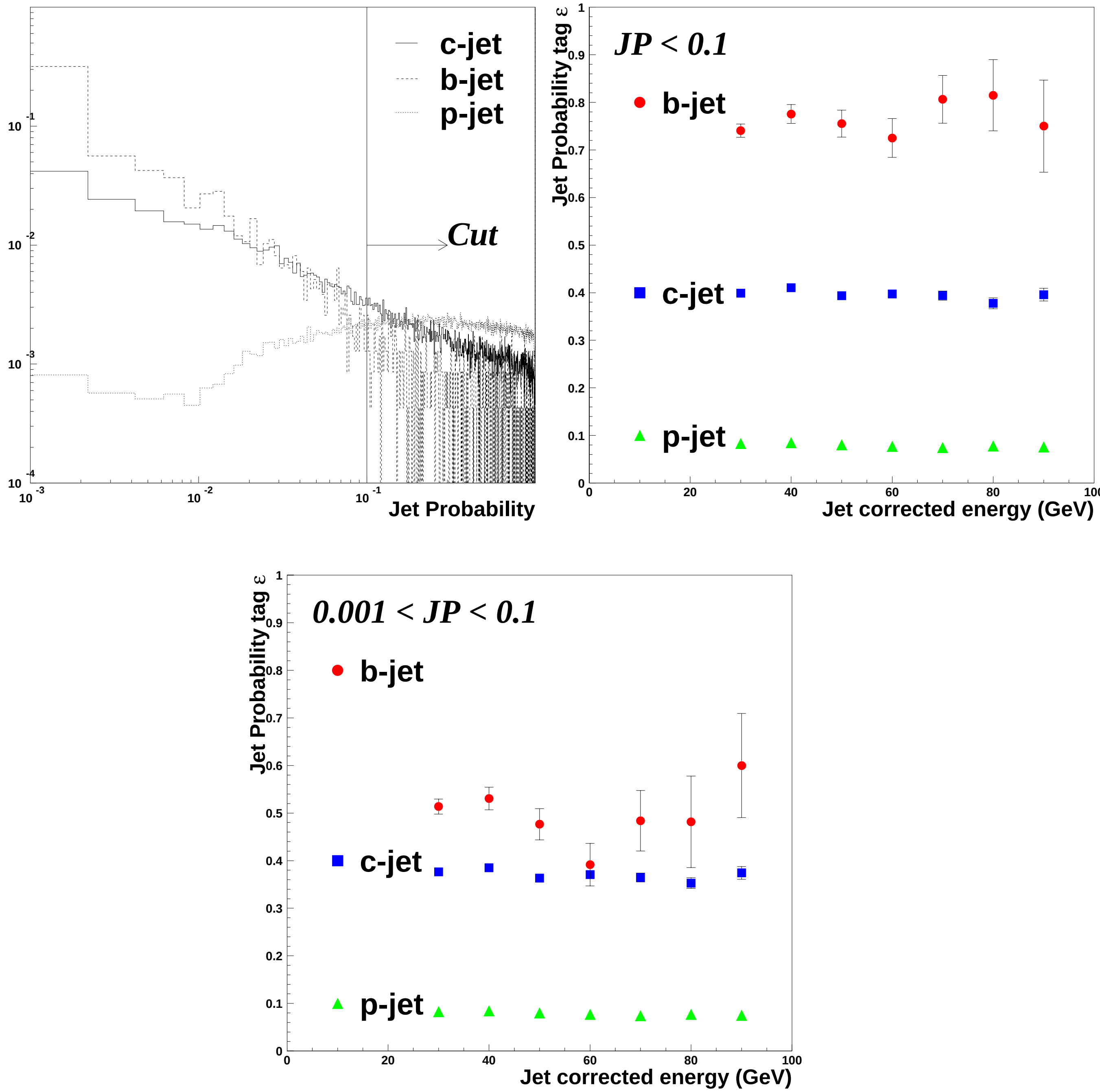

Figure B.4: Study of jet probability with PYTHIA W^+W^- events. Top left: jet probability distributions of c-, b-, and p-jets. Top right: efficiency of the cut $JP^+ < 0.1$ for c-, b-, and p-jets. Bottom: efficiency of the cut $0.001 < JP^+ < 0.1$ for c-, b-, and p-jets.

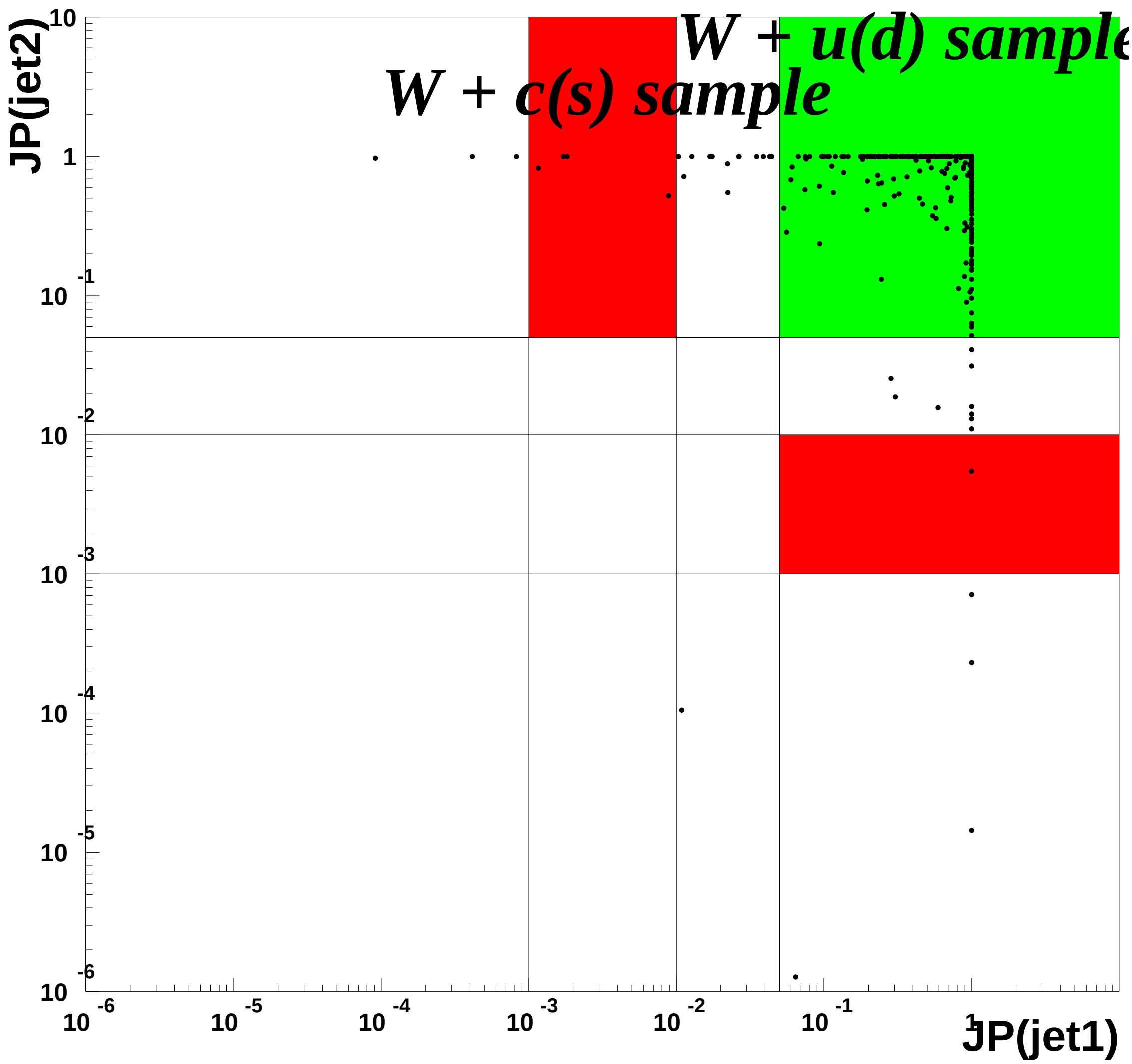

Figure B.5: Positive jet probability distribution for leading and second-leading jets in Run 1 data. The region $JP(jet1) > 0.05$ and $JP(jet2) > 0.05$ corresponds to the $W + ud$ sample, while the other two shaded regions contain the $W + cs$ sample. The wide unshaded region around the origin is dominated by b's.

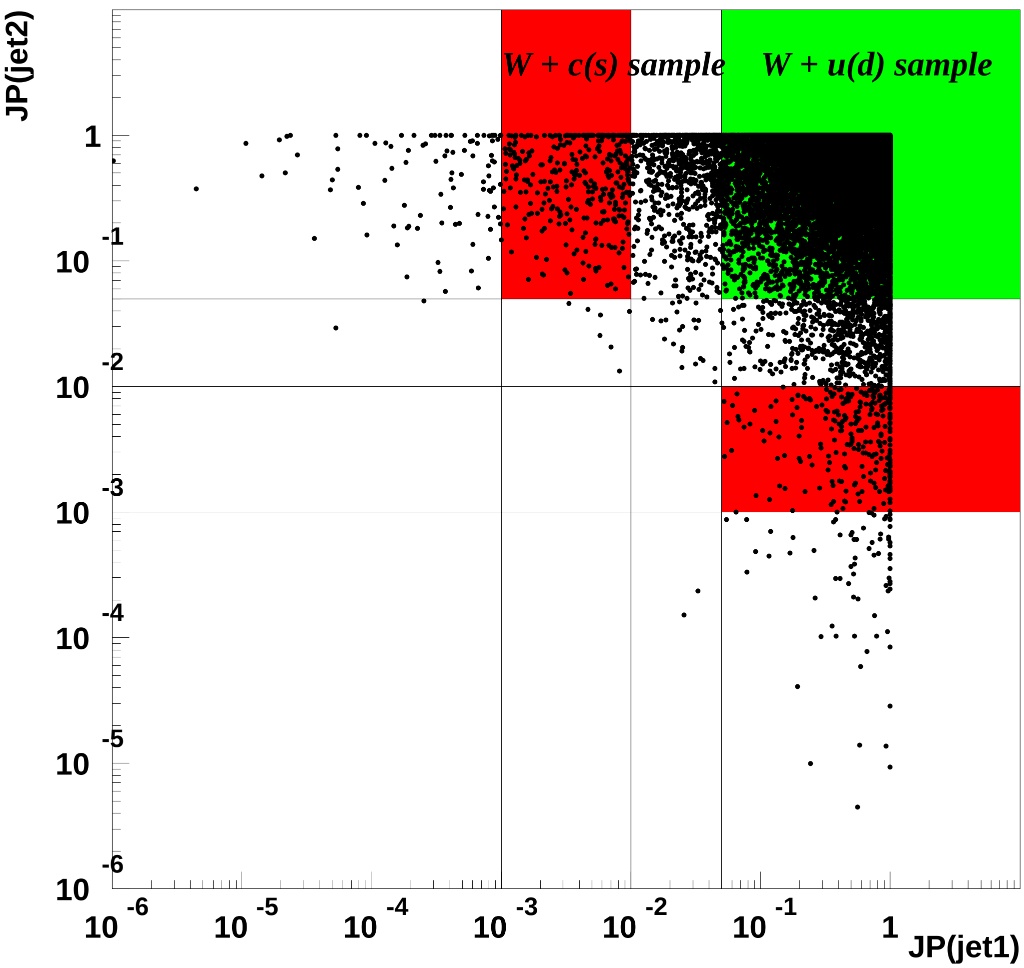

Figure B.6: Positive jet probability distribution for leading and second-leading jets in PYTHIA W^+W^- events. The region $JP(jet1) > 0.05$ and $JP(jet2) > 0.05$ corresponds to the $W + ud$ sample, while the other two shaded regions contain the $W + cs$ sample. The wide unshaded region around the origin is dominated by b's.

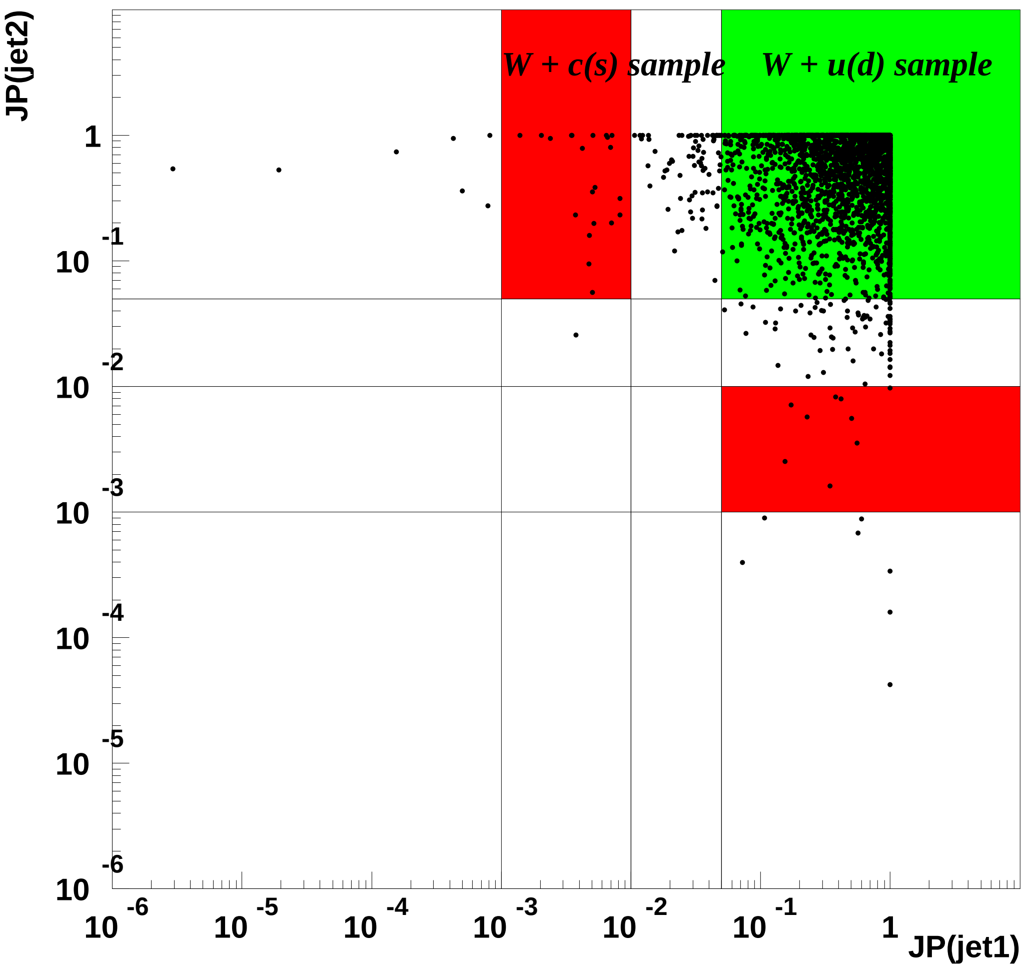

Figure B.7: Positive jet probability distribution for leading and second-leading jets in VECBOS $W + 2$jets events. The region $JP(jet1) > 0.05$ and $JP(jet2) > 0.05$ corresponds to the $W + ud$ sample, while the other two shaded regions contain the $W + cs$ sample. The wide unshaded region around the origin is dominated by b's.

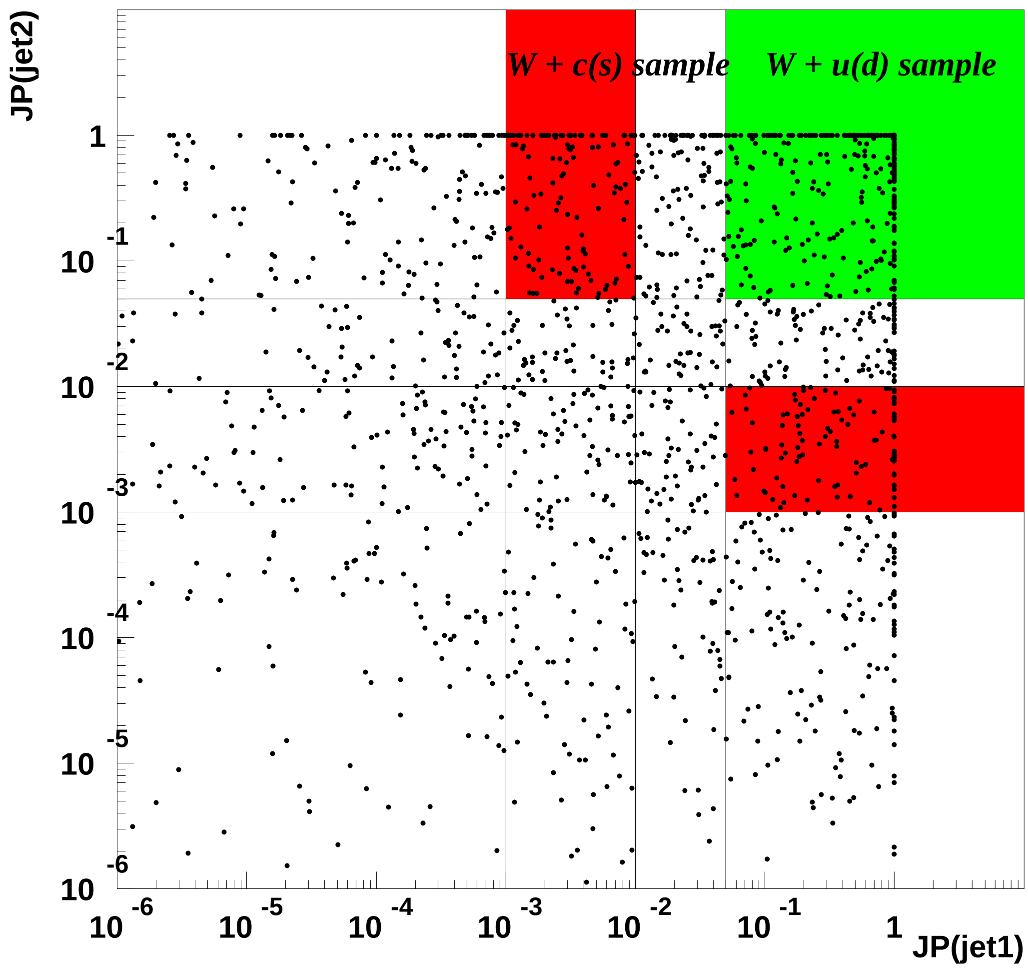

Figure B.8: Positive jet probability distribution for leading and second-leading jets in VECBOS $W b\bar{b}$ events. The region $JP(jet1) > 0.05$ and $JP(jet2) > 0.05$ corresponds to the $W + ud$ sample, while the other two shaded regions contain the $W + cs$ sample. The wide unshaded region around the origin is dominated by b's.

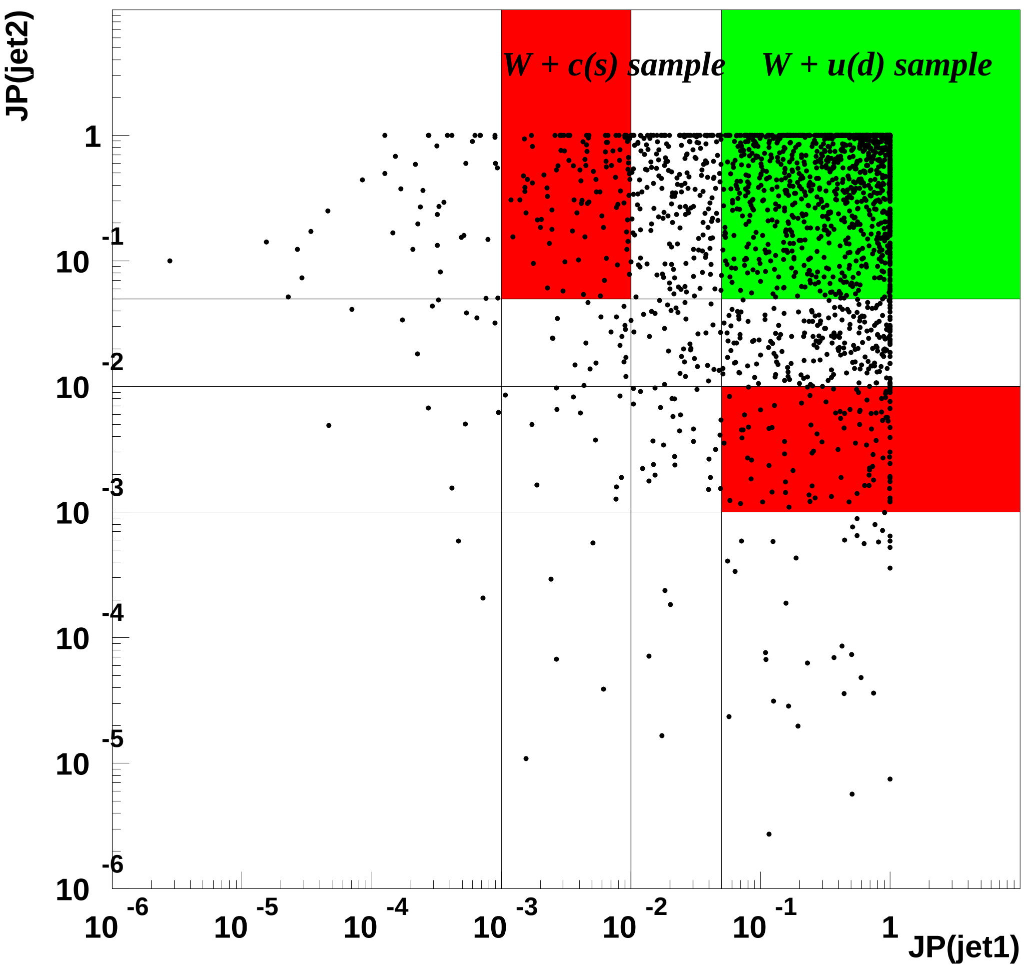

Figure B.9: Positive jet probability distribution for leading and second-leading jets in VECBOS $Wc\bar{c}$ events. The region $JP(jet1) > 0.05$ and $JP(jet2) > 0.05$ corresponds to the $W+ud$ sample, while the other two shaded regions contain the $W+cs$ sample. The wide unshaded region around the origin is dominated by b's.

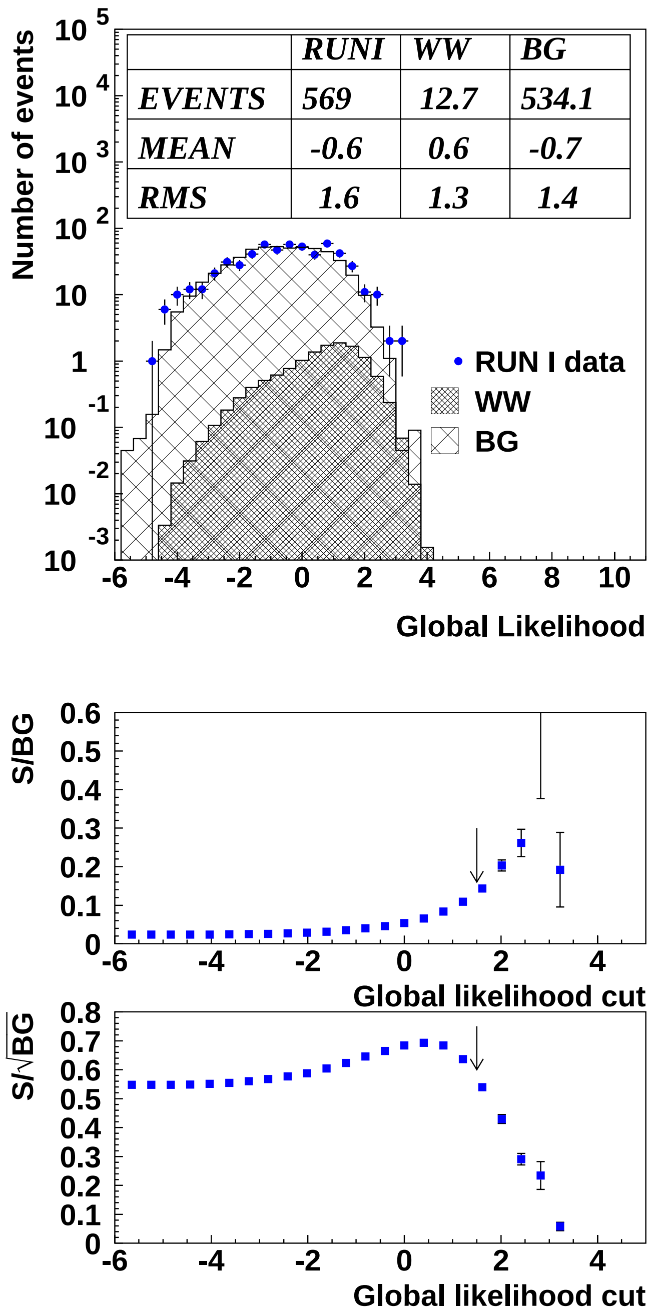

Figure B.10: Top: global likelihood distribution of the *JP* $W + ud$ sample; middle: signal over background ratio versus global likelihood cut; bottom: signal significance versus global likelihood cut.

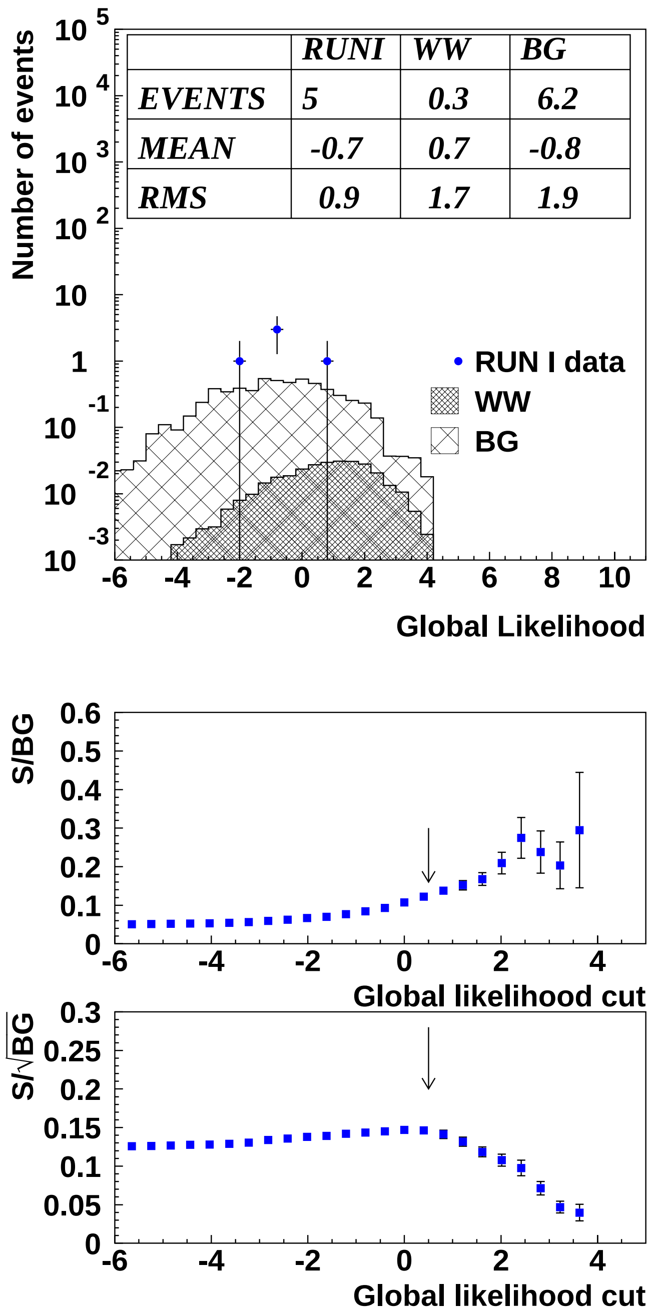

Figure B.11: Top: global likelihood distribution of the *JP* $W + cs$ sample; middle: signal over background ratio versus global likelihood cut; bottom: signal significance versus global likelihood cut.

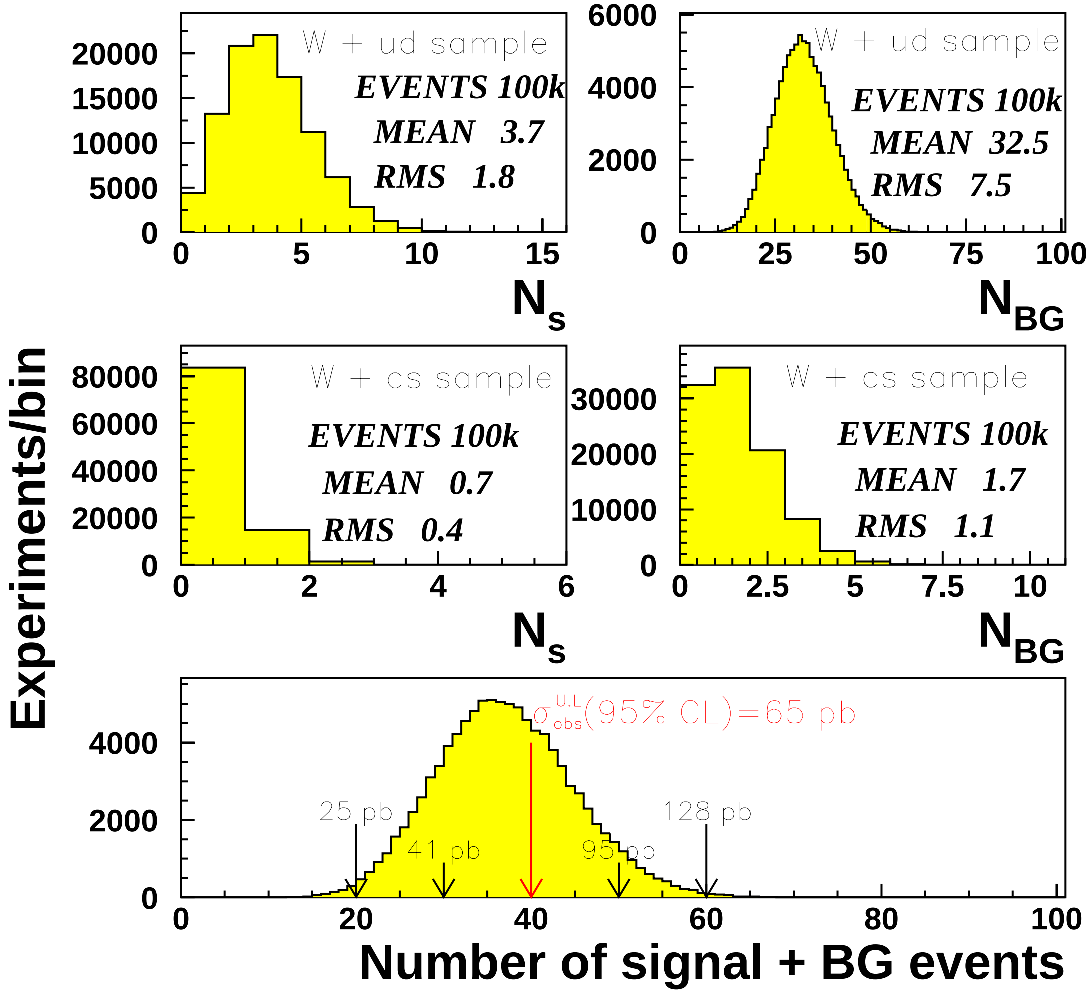

Figure B.12: Pseudo-experiment check of the *JP* upper limit calculation. Top: distributions of the numbers of signal and background events in the *JP* $W + ud$ subsamples. Middle: distributions of the numbers of signal and background events in the *JP* $W + cs$ subsamples. Bottom: distribution of the total number of events in the *JP* $W + ud$ and $W + cs$ subsamples combined. For five values of this total number of events, each marked by a short arrow, the corresponding 95% C.L. upper limit on W^+W^- production is indicated. A longer arrow marks the Run 1 result.

Appendix C

Run 2 prospects for observing W^+W^- in the lepton+dijet channel

We evaluated the feasibility of a W-pair search in the dijet channel in Run 2,based on the above Run 1 analysis and the following assumptions. In Run 2, the planned integrated luminosity is 2 fb^{-1}, resulting in 20 times more data than in Run 1. The increased tracking efficiency and η acceptance of the silicon vertex detector yields SECVTX tagging efficiencies of $\sim 20\%$ and $\sim 50\%$ for charm and bottom jets respectively. The jet energy resolution will be improved by using information from the tracker, the shower-max detectors and the HAD/EM segmentation of the calorimeters. This alone will improve the dijet mass resolution by about 10%, increasing the expected number of signal events by about 5%. An additional 4% increase in that number comes from the rise in W^+W^- production cross section with $\sqrt{s}$ (1.8 to 2.0 TeV).

Given these assumptions, the Run 2 analysis can be further optimized by requiring at least two jets with uncorrected E_T greater than 15 GeV and detector $|\eta| < 2$, thereby extending the jet acceptance to the plug region.

Taking all of these changes into account, the expected numbers of W^+W^- and background events in the $W + cs$ sample are 38 and 140 respectively, while in the $W + ud$ sample these numbers are 210 and 2743 respectively. The resulting signal significance ($S/\sqrt{B}$) is about 4.6.

Bibliography

[1] CDF Collaboration, F. Abe *et al.*, "*Limits on W W Z and W W gamma couplings from W W and W Z production in p anti-p collisions at s**(1/2) = 1.8-TeV.*", Phys. Rev. Lett. **75**: 1017-1022, 1995.

[2] CDF Collaboration, F. Abe *et al.*, "*Evidence of* W^+W^- *Production in* $p\bar{p}$ *collision at* $\sqrt{s} = 1.8$ *TeV*", Phys. Rev. Lett. **78**, 4537 (1997).

[3] R. D. Field and R. P. Feynman, "*A parametrization of the properties of quark jets*", Nucl. Phys. **B 136**, 1 (1978).

[4] CDF Collaboration, F. Abe *et al.*, "*Measurement of* $B^0\bar{B}^0$ *flavor oscillations using jet charge and lepton flavor tagging in* $p\bar{p}$ *collision at* $\sqrt{s} = 1.8$ *TeV*", Phys. Rev. **D60**, 072003 (1999).

[5] D0 Collaboration, B. Abbott *et al.*, "*Limits on Anomalous* $WW\gamma$ *and* WWZ *Couplings.*", Phys. Rev. D Rapid Communications **D58**, 31102 (1998).

[6] D0 Collaboration, B. Abbott *et al.*, "*Studies of* WW *and* WZ *Production and Limits on Anomalous* $WW\gamma$ *and* WWZ *Couplings.*", Phys. Rev. **D60**, 072002 (1999).

[7] D0 Collaboration, B. Abbott *et al.*, "*Limits on Anomalous* $WW\gamma$ *and* WWZ *Couplings from* $WW/WZ \rightarrow e\nu jj$ *Production.*", Phys. Rev. **D62**, 052005 (2000).

[8] The OPAL Collaboration, G. Abbiendi *et al.*, "W^+W^- *production and triple gauge boson couplings at LEP energies up to 183 GeV.*", CERN-EP/98-167 (1998), submitted to the European Physical Journal C.

[9] The LEP Working Group for Higgs Boson Searches, "*Search for the Standard Model Higgs Boson at LEP.*", CERN-EP/2003-011 (2003), Submitted to Phys. Lett. B

[10] J. Conway, "*Higgs searches at the Tevatron.*", FERMILAB-CONF-01-119-E (Jun 2001).

[11] CDF Collaboration, F. Abe et al. "*The CDF Detector: An Overview*", Nucl. Instrum. Methods Phys. Res., Sect. **A 271**, 387 (1988).

[12] S. Tkaczyk et al., "*The CDF Silicon Vertex Detector*", Nucl. Instr. Meth. **A342**, 240-250 (1994); D. Amidei et al., "*The Silicon Vertex Detector of the Collider Detector at Fermilab*", Nucl. Instr. Meth. **A350**, 73-130 (1994); P. Azzi et al., "*SVX' , the New CDF Silicon Vertex Ditector*, Nucl. Instrum. Methods Phys. Res., Sect. **A360**, 137 (1995).

[13] F. Snider et al., "*The CDF Vertex Time Projection Chamber System*", Nucl. Instrum. Meth. **A268**, 75 (1988). This is a reference for the previous generation of the device. The replacement for the Run I (1992-1996) data-taking period has more modules, each with a shorter drift length, but otherwise similar.

[14] F. Bedeschi et al., "*Design and Construction of the CDF Central Tracking Chamber*", Nucl. Instrum. Methods Phys. Res., Sect. **A268**, 50 (1988).

[15] F. Abe et al., "*Evidence for top quark production in p-barp collisions at sqrt s =1.8 TeV*", Phys Rev **D50**, 2966 (1994)

[16] F. Abe et al., "*Measurement of the $t\bar{t}$ Production Cross Section in $p\bar{p}$ Collisions at $\sqrt{s}$ = 1.8 TeV*", Phys Rev Lett.**80**, 2773 (1997).

[17] T.Sjostarad, Comput. Phys. Comm. **39** 347 (1986).

[18] T.Sjostarad and M.Bengtsson Comput. Phys. Comm. **46** 43 (1987).

[19] F.A.Berends, W.T.Giele, H.Kuijf and B.Tansk, Nucl. Phys. **B357**, 32 (1991).

[20] G.Marchesini and B.R Webber Nucl. Phys. **B301**, 461 (1988).

[21] G.Marchesini et. al Comut. Phys. Comm. **67** 405 (1992).

[22] P.Avery, K.Read, G.Trahern, Cornell Internal Note CSN-212, March25, 1985 (unpublished).

[23] T. Chikamatsu *et al.*, "*Top quark search in the dilepton channel in 1.8-TeV proton - anti-proton collisions.*", FERMILAB-THESIS-1994-34 (Apr 1994).

[24] D. Cronin-Hennessy, "*Tests of Perturbative QCD in W + jets events produced in s**(1/2) 1.8-TeV proton - anti-proton collisions.*", FERMILAB-THESIS-1997-42 (1997).

[25] T. Affolder *et al.* (CDF Collaboration), "*Measurement of the $t\bar{t}$ production cross section in $p\bar{p}$ collisions at $\sqrt{s} = 1.8$ TeV*", Phys. Rev. **D64**, 032002 (2001).

[26] CDF Collaboration, F. Abe et al., "*Evidence for top quark production in* $p\bar{p}$ *Collisions at* $\sqrt{s}$*=1.8 TeV*", Phys. Rev. **D50**: 2966-3026, 1994.

[27] R. Bonciani *et al.*, Nucl. Phys. **B 529**, 424 (1998).

[28] M. Smith and S. Willenbrock, Phys. Rev. **D 54**, 6696 (1996).

[29] T. Stelzer, Z. Sullivan, and S. Willenbrock, Phys. Rev. **D 56**, 5919 (1997).

[30] J. Ohnemus, Phys. Rev. **D 44**, 1403 (1991).
S. Frixione, Nucl. Phys. **B 410**, 280 (1993).

[31] D. Buskulic et al., Phys. Lett. **B313**, 535 (1993).

[32] F. Abe et al., Phys. Rev. Lett. **74**, 2626 (1995).

[33] J.R. Andersen, N.H. Brook, Yu.L. Dokshitzer, V.A. Khoze, W. Kittel, W. Ochs, W.J. Stirling, G. Zanderighi, "*Multiparticle Production in QCD Jets.*", May 2002, J. Phys. **G28**: 2509-2522; CDF Collaboration, F. Abe *et al.*, "*Momentum Distribution of Charged Particles in Jets in Dijet Events in* $p\bar{p}$ *Collisions at S**(1/2) = 1.8-TeV and Comparison to Perturbative QCD Predictions.*", FERMILAB-PUB-02-096-E, Jun 2002.; M. Ninomiya, "*Study of jet fragmentation properties in 1.8-TeV proton - anti-proton collisions*", FERMILAB-THESIS-1992-16 (Jan 1992); S. Kanda, "*Measurement of jet fragmentation properties in p - anti-p collisions at s**(1/2) = 1.8-TeV*", FERMILAB-THESIS-1990-02 (Jun 1990)

[34] Vernon D. Barger, Roger J.N. Phillips, "Collider Physics", P270-272

[35] T. Affolder *et al.* (CDF Collaboration), "*Measurement of the top quark mass with the collider detector at Fermilab*", Phys. Rev. **D63**, 032003 (2001).

[36] J. Wahl, "*A Measurement of* $R = (\sigma \times B(p\bar{p} \rightarrow W^{\pm} \rightarrow e^{\pm}\nu))/(\sigma \times B(p\bar{p} \rightarrow Z0 \rightarrow e^{+}e^{-}))$ *using the CDF detector in proton anti-proton collisions at S**(1/2) = 1800-GeV.*", FERMILAB-THESIS-1999-49 (1999)